the use of single sensors in seismic acquisition, processing and interpretation

The use of single sensors in seismic acquisition, processing and interpretation

Proefschrift

ter verkrijging van de graad van doctor
aan de Technische Universiteit Delft,
op gezag van de Rector Magnificus Prof. dr. ir. J.T. Fokkema,
voorzitter van het College voor Promoties,
in het openbaar te verdedigen
op vrijdag 19 oktober 2007 om 15.00 uur

door

Ionelia PANEA

Magister in Geology

University of Bucharest
geboren te Caracal-Olt, Romania

Dit proefschrift is goedgekeurd door de promotor:

Prof. dr. ir. J. T. Fokkema

Toegevoegd promotor: Dr. ir. G.G. Drijkoningen

Samenstelling promotiecommissie:

Rector Magnificus	voorzitter
Prof. dr.ir. J.T.Fokkema	Technische Universiteit Delft, promotor
Dr. ir. G. G. Drijkoningen	Technische Universiteit Delft, toegevoegd promotor
Prof. dr.ir. C.P. Wapenaar	Technische Universiteit Delft
Prof. dr.ir. S. Cloetingh	Vrije Universiteit Amsterdam
Prof. dr.ir. A-J. van der Veen	Technische Universiteit Delft
Prof. dr.ir. C. Dinu	Boekarest Universiteit
Dr. R. Stephenson	Vrije Universiteit Amsterdam

Dr. Randell Stephenson heeft als begeleider in belangrijke mate aan de totstandkoming van dit proefschrift bijgedragen.

Support

The research reported in this thesis has been financially supported by the Netherlands Research Center of Integrated

Printed by Curtea Veche in Romania

to my family,

Contents

Summary

The quality of the results of a seismic reflection project is strongly dependent on the data acquisition parameters. Once the data are recorded, we cannot undo some of the artifacts of the acquisition, such as spatial aliasing and hard-wired array forming. However, in the digital domain, we can undo some of the acquisition artifacts in processing by adding extra processing steps and/or using different parameters and algorithms. So, in general, it is desirable to move the digital world to the sensing element as much as possible.

The use of single sensors in data acquisition, processing and (tectonic) interpretation is studied in this thesis. In data acquisition, the quality difference between single sensors and hard-wired arrays depends on the characteristics of the studied area (e.g. surface topography). Via modeling we show the effect of the topography on the reflection responses of single sensors and (hard-wired) standard arrays. We also analyze the effect of amplitude and phase variations on the array responses, knowing that these types of variations can occur in field situations. Using fine spatially sampled single-sensor recordings, we obtain an improved array response after some corrections have been applied. In this way, we demonstrate the efficacy of the use of single sensors for data acquisition instead of hard-wired arrays.

Analyzing the noise attenuation performed by standard arrays, we propose a more efficient algorithm used to enhance the signal-to-noise ratio of array response, called the Minimum Variance Distortionless Response (MVDR)

beamformer. This is a type of beamformer that adapts itself to the data and therefore allows flexibility in its use. The beamformer creates weights of the different elements of the array, while for a standard array the weights are just 1. The beamformer is steered by the global characteristics of a record and uses this information to do local spatially adaptive beamforming. We show that in all cases studied, on synthetic as well as field data, the MVDR beamformer is superior to the standard array, in the sense that the MVDR showed better noise attenuation. The algorithm has been used for 2D and 3D datasets where the highest gain is achieved in 3D.

Two field single-sensor datasets are studied in this thesis. First one was a part of a shallow seismic reflection project and the second one a part of a deep seismic reflection and refraction project. Their recording was done using fine spatially sampled single sensors in the first case, and coarse single sensors in the second case. Since the presence of the surface waves is important on the shallow seismic dataset, the MVDR algorithm was used to enhance the signal-to-noise ratio of array responses. Next, the accuracy of the 2D velocity model, used for stacking and migration of the data, was increased using the post-stack stereotomography.

The single-sensor deep seismic reflection dataset was recorded with the purpose to study the crustal structure in the bending zone of Carpathians. Data processing is done following two directions, namely the processing for the upper and lower crust reflectivity. Both time sections were used for tectonic interpretation that provided new interesting structural features in the subsurface in the curvature zone of Carpathians which has not been detected before and seems consistent with other deep-refraction studies.

Samenvatting

De kwaliteit van de resultaten van een seismisch reflectie-experiment hangt sterk af van de data-acquisitie parameters. Als de data eenmaal zijn vastgelegd, is het niet meer mogelijk om bepaalde artefacten van de acquisitie, zoals een onvoldoende fijne ruimtelijke bemonstering en fysieke groepvorming, ongedaan te maken. Echter, in het digitale domein is het wel mogelijk om sommige artefacten van de acquisitie ongedaan te maken, door het toevoegen van extra bewerkingsstappen en/of het gebruiken van andere parameters en algoritmen. In het algemeen is het dus wenselijk om de digitalisering zo ver als mogelijk door te zetten naar de opname apparatuur in het veld.

Het gebruik van enkele sensoren in data-acquisitie, bewerking en (tektonische) interpretatie is het onderwerp van studie in dit proefschrift. Bij data-acquisitie hangt het kwaliteitsverschil tussen opnames gemaakt met enkele sensoren en fysieke groepen van sensoren af van de karakteristieken van het onderzochte gebied (bijv. de topografie aan de oppervlakte). Middels modeleren laten we het effect zien dat de topografie heeft op de reflectierespons van enkele sensoren en standaard (fysieke) groepen. Tevens analyseren we het effect van variaties in amplitude en fase op de groeprespons, dit soort variaties treedt in het veld namelijk vaak op. Wanneer we gebruik maken van opnamen gedaan met enkele sensoren in een fijne ruimtelijke bemonstering, verkrijgen we na het toepassen van enige correcties een verbeterde groeprespons. Op deze

wijze tonen we de doeltreffendheid aan van het gebruik van enkele sensoren ten opzichte van fysieke groepen van sensoren.

Aan de hand van het bestuderen van de ruisverzwakking verkregen met standaard groepen, stellen we een efficiënter algoritme voor om de signaal/ruis verhouding van de groeprespons te verbeteren, genaamd de Minimum Variantie Vervormingloze Respons (MVDR) beamformer. Dit type beamformer past zichzelf aan de data aan, en is derhalve flexibel in gebruik. De beamformer creëert gewichten voor ieder element van een groep, terwijl bij een standaard groep de gewichten gewoon één zijn. De beamformer wordt gestuurd door de globale karakteristieken van een opname en gebruikt deze informatie om lokaal een ruimtelijk afhankelijke beamforming toe te passen. We tonen aan dat in alle bestudeerde gevallen, op zowel synthetische data als data opgenomen in het veld, de MVDR beamformer beter werkt dan de standaard groep op het gebied van ruisverzwakking. Het algoritme is gebruikt op 2D en 3D datasets, de grootste verbetering treedt op in 3D.

Twee enkele-sensor datasets uit het veld zijn in dit proefschrift bestudeerd. De eerste is afkomstig uit een onderzoek naar ondiepe seismische reflecties, en de tweede uit een onderzoek naar diepe seismische reflecties en refracties. In het eerste geval werden de opnamen gemaakt met behulp van enkele sensoren, met een fijne ruimtelijke bemonstering, in het andere geval was de ruimtelijke bemonstering grof. Aangezien oppervlaktegolven dominant aanwezig zijn op de data voor ondiepe seismiek, werd het MVDR algoritme gebruikt om de signaal/ruis verhouding van de groepresponsies te verbeteren. Vervolgens werd de nauwkeurigheid van het 2D ‘stacking’ en migratie snelheidsmodel vergroot middels ‘post-stack’ stereotomografie.

De dataset met diepe reflecties werd opgenomen met enkele ontvangers met als doel het bestuderen van de structuur in de aardkorst bij de plooiingszone van de Karpaten. De data werden twee keer verwerkt, om een

optimaal beeld te verkrijgen van de contrasten in het bovenste en onderste gedeelte van de aardkorst. De twee tijdsecties die dit opleverde, werden beide gebruikt voor tektonische interpretatie, waarbij nieuwe structuren in de ondergrond van de plooiingszone van de Karpaten werden opgemerkt die consistent lijken met bevindingen uit andere onderzoeken voor diepe refracties.

List of symbols

a – steering vector
α – emergence angle in stereotomography
β_S – takeoff angle to the source S
β_R – takeoff angle to the receiver R
d – vector of single-element observations
$\mathbf{d}_o$ – vector of analytic complex signal
d_i^r – real stereotomographic dataset
d_i^c – computed stereotomographic dataset
e_{tx} – error in the (t, x)-domain
e_{fk} – error in the (f, k_x)-domain
ε – positive constant
f – frequency
h – half offset
k_n – horizontal wavenumber of the noise
k_N – Nyquist wavenumber
k_M – rejection notch wavenumber
k_x – wavenumber in the spatial direction x
λ_s – horizontal wavelength of the signal
λ_n – horizontal wavelength of the noise
λ_1 – Lagrange multiplier
λ_2 – Lagrange multiplier

m – model part in stereotomography

$\boldsymbol{n}$ – noise vector

p_{sx} – slope on the common-shot gather

p_{rx} – slope on the common-receiver gather

ρ - density

$\boldsymbol{s}$ – desired signal vector

s_o – analytic complex signal

t – time

t_o – zero-offset travel-time

t_{SR} – two-way travel-time

t_{CRS} – CRS-stacking operator

τ – delay in time

v – velocity

v_o – near-surface velocity

$\mathbf{w}$ – weight vector

$\mathbf{w}_{opt}$ – optimal weight vector

x – space

x_o – output position in stereotomography

x_{CMP} – midpoint position

y – MVDR beamformer response

y^o – desired array response

y^s – standard-array or MVDR beamformer response

$\tilde{y}^o$ – (f, k_x)-domain amplitude spectrum of the desired array response

$\tilde{y}^s$ – (f, k_x)-domain amplitude spectrum of the standard-array or MVDR beamformer response

z - depth

A – transfer function of receiver array

A_{norm} – normalized transfer function of receiver array

C – velocity field

$\mathbf{D_s}$ – matrix that contain the desired signal

$\mathbf{D_n}$ – matrix that contain noise

$\mathbf{\Delta}$ – error matrix

Δt – travel-time interval

Δx – single-sensor spacing

Δx_p – distance interval

E – output power

E_n – noise power

E_s – signal power

I – identity matrix

J – number of B-spline functions

L – array length

$L_1(\boldsymbol{w}, \lambda_1)$ – Lagrangian function

$L_2(\boldsymbol{w}, \lambda_2)$ – Lagrangian function

M – number of array elements in in-line direction

N – normal wave in stereotomography

NIP – Normal-incidence-point wave in stereotomography

N_t – number of time samples

N_e – number of picked travel-times

N_f – number of frequency samples

N_k – number of wavenumber samples

N_{k_old} – number of wavenumber samples computed for single-sensor spacing

N_{k_new} – number of wavenumber samples computed for desired group interval

P – number of array elements in cross-line direction

P_o – acquisition point

R_N – radius of the N wavefront

R_{NIP} – radius of the NIP wavefront

$\mathbf{R_{ps}}$ – presumed signal covariance matrix
$\mathbf{R_s}$ – signal covariance matrix
$\mathbf{R_n}$ – noise covariance matrix
$\mathbf{R_d}$ – data covariance matrix
$\mathbf{R}$ – sample covariance matrix
R – receiver position
S – source position
SNR – signal-to-noise ratio
T – transpose
T_S – two-way travel-time to source S
T_R – two-way travel-time to receiver R
V_a – apparent horizontal velocity
V_p – P-wave velocity
V_s – S-wave velocity
X – reflecting / diffracting point

Chapter 1

Introduction

1.1 Background

The seismic reflection method is the most successful method to explore and monitor hydrocarbon reservoirs from the surface. It has been used for decades in this industry, starting in the beginning of the 1900's. In the early days, one single sensor was a big investment, and no exploration industry existed. Only during that century, seismic was used more and more to explore the subsurface, and many big oil and gas fields were discovered using single-sensor recordings. In the 1960's two advances came: the common-midpoint (CMP) method and the advent of the computer (Mayne, 1962). Also, during that time, the sensors had become much smaller and allowed arrays to be used. Arrays had the task to reduce noise, on land being mainly surface waves; they act as discrete spatial filters in the field. Regarding the aliased frequencies, the recording station contains an anti-alias filter that removes the frequencies greater than the Nyquist frequency. In addition, the arrays were supposed to reduce the amount of data since a multi-channel system of 16 channels in the 1960's was seen as

high-tech. Since those days, arrays existed while the number of channels increased and increased over time. Nowadays, systems of 10,000 channels are not uncommon. A further advance in understanding the tasks of arrays was put forward in the 1980's. It was recognized that the seismic receivers were supposed to sample the wavefield properly [*Ongkiehong and Askin* (1988)]. At that time it was recognized that the number of channels was not sufficient to have proper sampling so arrays were identified as spatial anti-alias filters and resampling operators. Nowadays, with 10,000-channel systems, this spatial sampling can be fully done in 3D, and array operations can be done digitally rather than in an analog way (the old-fashioned hard-wired array).

In the more academically oriented field of crustal seismology, the developments were not supported by a rich industry but have been stimulated by more fundamental geological questions. During the last century, many active seismic surveys have taken place to unravel the structure of the earth as a whole. After the international ban on nuclear tests, the sources were less extreme, but large sources such as large air guns and large amounts of dynamite are still being used for exploring the crust of the earth. Also, in this field arrays were introduced to reduce the source-induced noise, i.e., surface waves. Many of the DEKORP lines going through Germany were recorded with arrays. In Romania, arrays are also used to monitor the regional seismic activity [*Ghica et al.* (2005)]. But also here the number of channels increased and so allowed a fuller recording of the whole wavefield, although mostly being 2D recordings. In this field, arrays are not always used, the reason being that if the topography or shallow subsurface is heavily structured, the array may work as a damper rather than a reflector-enhancer. This is typically happening in hilly or mountainous areas, where elevation statics are significant. It is known that reflections (wave propagating vertically into the earth) are more sensitive to statics compared to surface waves (wave propagating horizontally).

In this thesis, we will model, analyze and process single-sensor recordings for these two settings: for exploration (Chapters 2, 3 and 4) and for crustal seismology (Chapter 5). In the last decades, various modeling codes were designed in order to get synthetic seismograms for complex subsurface geometries and for arbitrary source-receiver separations. The complexity of the modeling codes varies from the convolution between an input wavelet and a reflection time series to, for example, the fourth-order-finite difference modeling of the P- and S-waves. The results of the synthetic dataset pre-processing modeled with single sensors or array of sensors for a studied area can influence the choice of the data acquisition parameters (Chapter 2). Single-sensor spacing is considered an important parameter since it is a source of spatial aliasing in case of slow seismic arrivals (e.g. surface waves). Data without spatial aliasing are data sampled to more than two points per wavelength, otherwise the wave arrival direction becomes ambiguous. Aliasing can occur on the axes of time, depth, geophone, shot, midpoint, offset or crossline, but in practice is the worst on the horizontal space axes. The efficiency of some of the processing algorithms is influenced by spatial aliasing, such as *f-k* filtering and migration (spatial deconvolution). There are algorithms that work good in the presence of aliased data belonging to the class of beamformers; they are applied to increase the signal-to-noise ratio of seismic records (Chapter 3).

In time, the algorithms designed for migration increased in complexity. Migration could only be done digitally in the 1970's, which has now developed in full pre-stack depth-migration in 3D. Also here the data reduction as achieved by arrays in the field helps in the migration process. In our era, single-sensor recordings is still too expensive to do in a pre-stack depth-migration since the amount of data would become, e.g., twelve-fold, determined by the number of receivers in one array. It is expected that in the future, this will

become a feasible option. A gain here would be is that higher-resolution images can be obtained using single-sensor recordings. The possibility will be shown in Chapter 5.

1.2 Literature review

Single sensors are often used in the data acquisition, especially in deep seismic surveys. Nowadays, the fine spatially sampled single sensors tend to replace the arrays of receivers used in the acquisition of shallow data. It is known that arrays of sensors and sources are considered very efficient in coherent noise attenuation [*Newman and Mahoney* (1973), *Morse and Hildebrandt* (1989), *Cooper* (2004)]. An array sums the signals from a pattern of sources or receivers to attenuate various noises while attempting to preserve as much of the reflection signal as possible [*Stone* (1994)]. The design of an array is done taking into account that the single-sensor spacing must allow a proper recording of the noise (e.g. surface waves) and the group interval spacing must allow a proper recording of the reflected waves [*Vermeer* (1990)]; a proper recording meaning arrivals with no spatial aliasing. Also, it is known that shorter array emphasizes signal preservation while the longer array places priority on noise rejection [*Hoffe et al.* (2002)]. Modeling results showed that the hard-wired array response can be synthesized using fine spatially sampled single sensors recordings. The phase and amplitude variations occur due to the field conditions (rough topography, significant lateral velocity variations, irregular sensors spacing, imperfection in ground-coupling). These variations affect the real dataset [*Hoover and O'Brien* (1980), *Krohn* (1984), *Drijkoningen* (2000), *Muyzert and Vermeer* (2004), *Drijkoningen et al.* (2006), *Capman et al.* (2006)]. The use of single-sensor recordings to synthesize the standard array response allows a data pre-processing (e.g. static corrections)

that can attenuate the effect of such variations [*Hoffe et al.* (2002), *Capman et al.* (2006)]. In this way, the signal-to-noise ratio of array response is enhanced; also, the reflected waves are protected. This is considered one advantage of the use of single-sensors in data acquisition with important effect on the data processing and interpretation results.

The arrays of sensors are used in many fields, such as sonar, radar, microphone array speech processing [*Capon et al.* (1967), *Cox* (1973), *Gershman et al.* (1995), *Gershman et al.* (2000)], seismology [*Ozbek* (2000)], wireless communications [*Godara* (1997), *Rapapport* (1998)]. Their elementary recordings are input data to different algorithms (e.g. beamforming) proposed to attenuate various noise contributions. Different types of beamformers were designed depending on the type of noise that has to be attenuated. The simplest one is known as delay-and-sum beamformer [*Johnson et al.* (1993)]. The complexity of the beamformers increased in order to be able to adapt to any type of mismatches between the designing approaches and real data [*Cox* (1973), *Godara* (1986), *Cox et al.* (1987), *Feldman and Griffiths* (1994), *Wax and Anu* (1996), *Bell et al.* (2000), *Shahbazpanahi et al.* (2003)]. In the exploration seismology, *Ozbek* (2000) proposed a type of beamformer that can be used to attenuate various types of coherent noise encountered in seismic data acquisition and processing. This type of beamformer can be thought as an adaptive *f-k* filter that is fixed in those parts of the (f, k)-amplitude spectrum that contain the signal to be protected and adaptive in the rest of it.

Sometimes, the signal-to-noise ratio of the seismic recordings can be low, even if single sensors or arrays are used in data acquisition. The lack of clear reflections on the pre-stack data can decrease the accuracy of the standard velocity analysis. Based on this, many algorithms were proposed in order to obtain a reliable velocity model used for stacking and migration.

Stereotomography is an example of such algorithm. It belongs to the class of the slope methods and it can be applied on pre-stack [*Billette and Lambaré* (1998), *Chauris et al.* (2002), *Chalard et al.* (2002), *Billette et al.* (2003), *Lambaré et al.* (2003), *Lambaré et al.* (2004)] and post-stack domains [*Lavaud et al.* (2004)]. Both algorithms have been applied on synthetic and marine dataset. The application of the pre-stack stereotomography is restricted to the datasets recorded using the same spacing between single sensors and sources. The advantage of the post-stack stereotomography is that its application does not require the same spacing between single sensors and sources and the automatic traveltime picking is done on a Common-Reflection-Surface (CRS) stack that is characterized by a higher signal-to-noise ratio due to stacking of traces from super common-midpoint gathers. The computation of the CRS stack also allows the computation of a control triplet parameter (α, R_{NIP}, R_N), where α is the emergence angle of the zero-offset ray, R_{NIP} and R_N are the radii of the wavefront curvatures [*Müller* (1999), *Mann et al.* (1999), *Jaeger et al.* (2001), *Trappe et al.* (2001)]. They all are associated with two hypothetical waves, namely the so-called normal wave (N) and the normal-incident-point wave (NIP). The CRS stack is a model independent seismic imaging method that can be performed without any ray tracing and macro-velocity model estimation. The knowledge of the near surface velocity is required [*Jaeger et al.* (2001)]. It has been demonstrated that the CRS stack produces high-resolution time-domain sections and post-stack depth migration of CRS stacks may be considered as an alternative to pre-stack depth migration in areas of high difficulties (e.g. complicate tectonic structure) [*Hubral* (1999), *Trappe et al.* (2001)].

1.3 Thesis aim and outline

The aim of this thesis is to study the effectiveness of the use of single sensors and arrays of sensors in areas with different topographies. Also, starting from the modeling results regarding to the surface waves attenuation performed by standard arrays, we present an algorithm that will perform a better attenuation of the un-desired energy contained by single-sensor records. Throughout the thesis, the standard array response is equivalent with the hard-wired array response. Using fine spatially sampled single-sensor records as input data, this response can be synthesized in two steps. First, we sum a number of traces equal with the desired number of array elements and, then, the output is spatially resampled to the desired group interval.

The results of the analysis of synthetic and field single-sensor records will be presented in this thesis. In Chapter 2 we compare the processing and tectonic interpretation results of two modeled datasets. The first one is represented by single-sensor recordings and the second one is represented by recordings with standard array responses. Both datasets are modeled in the presence of phase variations introduced by significant elevation statics and irregular spacing of single sensors. The elevation profile used in modeling is based on the field situation described in Chapter 5. The standard array responses are computed following the procedure described above.

In the next chapter we will describe a new algorithm, the Minimum Variance Distortionless Response (MVDR) beamformer, which can be applied on 2D and 3D single-sensor records in order to attenuate the undesired energy. We define as undesired energy all energy present at wavenumbers greater than the Nyquist wavenumber computed for the desired group interval. We start with the analysis of single-sensor records modeled for simple depth models and, then, we increase the model complexity in order to get various types of waves.

Since the field records are affected by the amplitude and phase variations due to the field conditions, we model single-sensor records in the presence of these variations; then, we apply the MVDR beamforming in order to see how efficient is its noise attenuation in such conditions. At the end of Chapter 3, the standard array-forming and MVDR beamforming are applied on a single-sensor shallow dataset. Since the field data quality is low, a new tomographic method is used to determine the velocity model required by stacking and depth migration. This is the subject of Chapter 4. The results of two different approaches are presented here, namely the Common-Midpoint approach and the Common-Reflection-Surface-stereomography approach.

The effectiveness of the use of single sensors in tectonic interpretation will be shown in Chapter 5. We use a single-sensor deep dataset recorded along a profile that started and crossed the mountainous and hilly areas and ended in the plain area. Different processing directions are followed in order to get the best structural image possible.

Finally, conclusions are drawn in Chapter 6.

Chapter 2

Problem statement for single-sensor data in acquisition, processing and interpretation

2.1 Introduction

The quality of land seismic data depends on many factors. In first instance it is important to set the acquisition parameters, such as the distances, right. But even if these parameters are correctly set, how the geophones are deployed can influence the signal-to-noise ratio of the seismic recordings. Land seismic data contain many un-desired arrivals that can be cumbersome to attenuate during the data processing. The most important type of noise is the so-called ground roll being surface or Rayleigh waves; they occur because of the presence of the (stress-free) surface and near-surface layers. Surface waves are characterized by low apparent velocities and small frequencies, compared to the reflected waves. These arrivals are sometimes recorded using improper acquisition parameters, since only proper recording of the *reflected* waves is performed. An example of such a parameter is the geophone spacing that, in general, is chosen too large for the proper recording of the surface waves. As a result, these slow arrivals are affected by spatial aliasing, which creates

problems during the data processing (e.g. filtering, migration) and interpretation. Other non-standard acquisition is a variation in field conditions, creating phase and amplitude variations across an array.

A common way, used for decades, to attenuate the surface waves is the use of hard-wired receiver arrays [*Newman and Mahoney* (1973), *Hoffe et al.* (2002), *Cooper et al.* (2004)]. Two parameters are crucial in the array design, namely the spacing between array elements and the size of group interval. The first one is chosen so that a proper sampling of the surface waves is allowed and, the second one, it is chosen so that a proper sampling of the reflected waves is allowed. In both cases, it is desired to have recordings without any spatial aliasing.

In the last two decades, the use of hard-wired arrays is more and more questioned and acquisition using finely spatially sampled single sensors is more being used [*Burger et al.* (1998), *Baeten et al.* (2000)]. Then, the conventional array response can be easily synthesized in two steps. Using this type of input dataset, the array response is synthesized in two steps. First, we sum a number of single-sensor recordings equal to the desired number of array elements. Then, we resample the result to the desired group interval; the size of the desired group interval has to be chosen so that the desired signal will not be spatial aliased.

In this chapter, we show that in case of significant field variations within arrays, using arrays in the standard way is not good enough for example, attenuation of the surface waves. There are situations when the remaining noise seen on the first step of array-forming will be heavily spatially aliased after resampling. Looking at the array response in the time domain we will see some remaining wavelets, sometimes, of significant amplitude and frequency; they can be seen as “edge-effects” of the array and should be attenuated because they degrade the quality of array response. In addition, the standard arrays do

not work properly in the presence of variations being caused by local variations in the field (coupling statics).

2.2 Seismic acquisition

In this section we will show that the use of conventional hard-wired arrays in hilly and mountainous areas will have a negative effect on the reflections. Their response can be analyzed by modeling different field situations. In addition, we will analyze the effect of phase and amplitude variation on the array response. Both types of variation affect the real dataset due to the field conditions [*Hoover and O'Brien* (1980), *Krohn* (1984), *Drijkoningen* (2000), *Hoffe et al.* (2002), *Panea et al.* (2003), *Panea et al.* (2004), *Panea and Drijkoningen* (2006), *Capman et al.*(2006)].

Phase variations are mainly caused by traveltime variations. These are introduced by rapid near-surface variations and could, via processing, be corrected with static corrections if the data allow (if arrays are used, it will not be possible to process them this way). In statics, the effect of the near subsurface is assumed to be a pure time delay and these delays are surface consistent, implying that each trace at a given location gets the same time delay [*Cox* (1999)]. The near surface affects the seismic data in several ways. For example, the lateral velocity variations in the near surface and variations in layer thickness or topography can cause variations in the arrival times and amplitudes of the upcoming events [*Capman et al.* (2006)]. The presence of the sub-surface and near-surface layers allows for the generation of the most important type of noise recorded on land data, namely the ground-roll. It was said that the use of suitable array patterns can suppress partially ground-roll [*Morse and Hildebrandt* (1989)]. Recent studies have shown that the array response can be less or even strongly distorted by increasing of the complexity

of the overburden, rapid lateral velocities variations on the scale of an array [*Muyzert and Vermeer* (2004)].

Amplitude variations are caused mainly by imperfect ground-coupling of geophones. The problem of coupling has been extensively studied in the last decades using modeling tests and field experiments [*Lamar* (1970), *Hoover and O'Brien* (1980), *Krohn* (1984), *Tan* (1987), *Drijkoningen* (2000), *Drijkoningen et al.* (2006)]. The term *coupling* defines a phenomenon that affects energy transfer. The coupling of a geophone to the ground involves the quality of the plant, how firmly these two are in contact, and also considerations of the geophone's weight and base area, because the geophone-ground coupling system as natural resonances and introduces a filtering action [*Sheriff* (1991)]. According to theory, the geophone-ground coupling is the difference between the velocity measured by the geophone and the velocity of the ground without the geophone. This, so-called, definition of the ground-coupling was used for theoretical models; it is also used for the design of geophones so that optimal characteristics can be found [*Drijkoningen* (2000)]. The practicing geophysicist takes into account the imperfections of the coupling of the geophones with its surroundings. As a consequence, the definition written above becomes: Bad geophone coupling is the difference between the velocity as measured by the badly planted geophone and the velocity as measured by the well-planted geophone [*Drijkoningen* (2000)]. Measurements of the geophone-ground coupling for vertical and horizontal geophones have been done in the laboratory and in the field [*Krohn* (1984), *Drijkoningen* (2000)]. Their results showed that the geophone accurately follows the ground motion for lower frequencies than the coupling resonant frequency. In case of higher frequencies, the coupling can alter both the amplitude and phase of the seismic signal. The coupling resonant frequency for vertical geophones is determined by the firmness of the soil [*Krohn* (1984)]. Based on the experiment results, it was accepted that for

conventional seismic recordings the use frequencies less than 100 Hz and vibrational amplitudes less than 10^{-2} cm/s, the normal planting of vertical geophones in firm soil is acceptable. For higher frequency recordings or for surveys that take place in areas with loose soil, the geophone should be buried, in order to achieve better coupling. In addition, the laboratory experiments showed that the length of the geophone spike affects the coupling [*Krohn* (1984)]. The effect of ground-coupling was studied in both domains, time and frequency, using different field datasets [*Drijkoningen* (2000)].

2.2.1 Standard array-forming

It is well-known that an array sums the signals coming from a pattern of receivers or sources to attenuate various types of noises while attempting to preserve as much of the reflection signal is possible [*Stone* (1994), *Hoffe et al.* (2002)]. An effect related to receiver arrays occurs in the conventional seismic processing when the common midpoint (CMP) stack forms [*Anstey* (1986), *Hoffe et al.* (2002)].

The underlying principle of receiver arrays is that the desired signal (primary reflected waves) propagates across an array with higher apparent horizontal velocity than that of the ground-roll, as an example of noisy arrival. For any given frequency value, f, the horizontal wavelength of the signal, $\lambda_s = V_a / f$, will be larger than the horizontal wavelength, λ_n, of the noise. Because the wavenumber is equal to the inverse of the wavelength, we will have a larger horizontal wavenumber of the noise, k_n [*Hoffe et al.* (2002)]. Based on this, we can design a spatial filter that can separate signal and noise; we can do it because, in some cases, we deal with seismic arrivals characterized by overlapping frequency content but different wavenumber contents [*Ongkiehong and Askin* (1988)]. But, the effect of a spatial filter can be obtained using

receiver arrays whose designing parameters are chosen such to obtain optimal spatial filter parameters (e.g. element spacing and group spacing). In seismic exploration, the use of spatial (wavenumber) filters is always considered a compromise; for example, a part of the desired signal can be removed when filtering the un-desired signal.

In the spatial-frequency, i.e., the wavenumber domain, the transfer function for an odd number of receivers (M) of an array is given as:

$$A(k_x) = e^{-((M-1)/2)\Delta x 2\pi i k_x} + \ldots + e^{-\Delta x 2\pi i k_x} + e^{0} + e^{\Delta x 2\pi i k_x} + \ldots + e^{((M-1)/2)\Delta x 2\pi i}. \quad (2.1)$$

Here, we have assumed that each term has the same weight which in practice will not be the case, e.g. due to coupling variations, topographic changes, etc. It is well-known that the above function can be condensed into the formula:

$$A(k_x) = \frac{\sin(M\Delta x \pi k_x)}{\sin(\Delta x \pi k_x)}. \quad (2.2)$$

In our modeling we will use the normalized transfer function:

$$A_{norm}(k_x) = \frac{1}{M}\frac{\sin(M\Delta x \pi k_x)}{\sin(\Delta x \pi k_x)}. \quad (2.3)$$

2.2.1.1 One array response without and with variations

Let us compute the array response using Equation 2.2. First, we model an array with 12 identical equally spaced elements ($\Delta x = 5$ meters). The normalized amplitude spectrum and the phase spectrum of the array response are displayed in Figure 2.1. The amplitude spectrum is symmetrical with the Nyquist wavenumber ($k_N = 1 / 2\Delta x$). The phase spectrum in the absence of any type of variation varies between 0 and π (see Figure 2.1).

On the amplitude spectrum of array response, we can separate three zones. The first one, called the pass-band zone, extends from $k = 0$ to the first rejection notch ($k_1 = 1 / L$, where $L = M\Delta x$ and M is the number of array elements). The rejection notches are found using $k_i = i / L$, where $i = 1, 2, \ldots M - 1$; the rejection notches define the wavenumbers where the amplitude spectrum of array response is zero. The second zone, called the aliased pass-band, extends from the last rejection notch, $k_{M-1} = (M - 1) / L$ to the end $k_M = 1 / \Delta x$. The third one, known as the rejection-band, extends between the pass-band and the aliased pass-band; the energy present on this band should be attenuated.

The shape of amplitude and phase spectra, displayed in Figure 2.1, can be distorted by the presence of different types of variations grouped into two types of variations, namely the phase and amplitude variations.

We can model the same array response in the presence of the phase variations, by mis-placing one array element using a maximum random variation of 10% from 5 metres; the spacing between the others array elements is 5 meters. Again, we model an array with 12 elements. In Figure 2.2, the amplitude and phase spectra are displayed in both the absence and presence of variations. We notice that both spectra are affected by phase variations. They look different than those obtained in the absence of variations (see Figure 2.2).

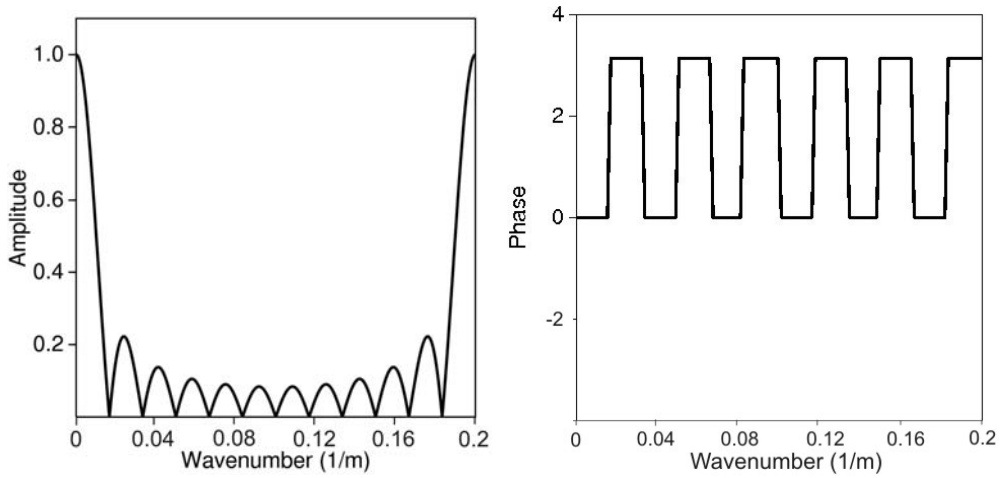

Figure 2.1. Amplitude (left) and phase (right) spectrum of array response

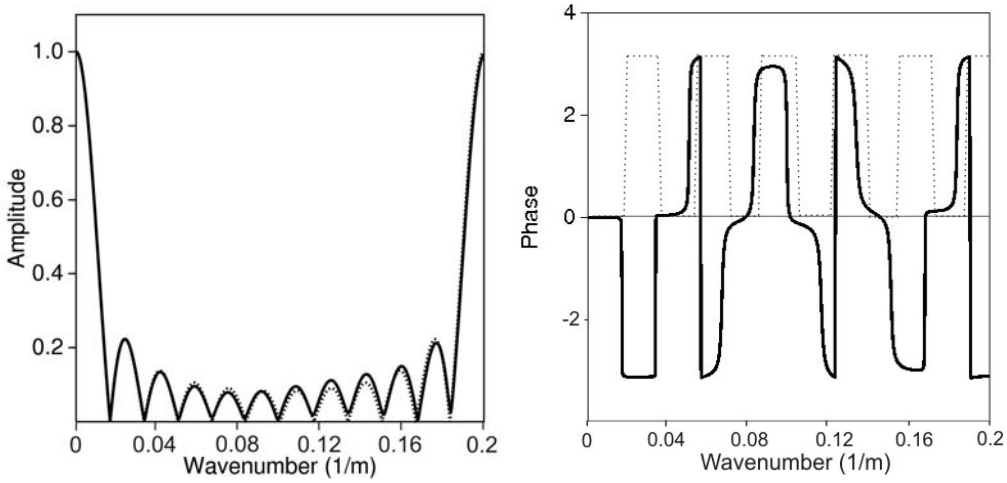

Figure 2.2. Amplitude (left) and phase (right) spectra of array response with (solid line) and without (dashed line) phase variation for one array element

Next, we model the response of an array with 12 elements in the presence of the phase variations by assuming irregular spacing between all elements instead of only one. The spacing is computed using a maximum random variation of 10% from the regular spacing of 5 meters. The amplitude and phase spectra of array response displayed in Figure 2.3 look more different than those displayed in Figure 2.2. The amplitude of the aliased pass-band is smaller and the amplitude spectrum has non-zero values at the rejection notches.

In order to analyze the effect of *amplitude* variations an array response, we model an array with 12 elements equally spaced at 5 meters but with different weights given to each element. First, we assume that one array element has a random weight, computed for a maximum random variation of 10%. Both amplitude and phase spectra of the array response are affected by this single error (see Figure 2.4). The distortions observed on both spectra become stronger when all array elements instead of only one have random weights, obtained for a maximum random variation of 10% (see Figure 2.5).

These modeling results show us that the presence of variations affects the array response, depending on the magnitude of variations.

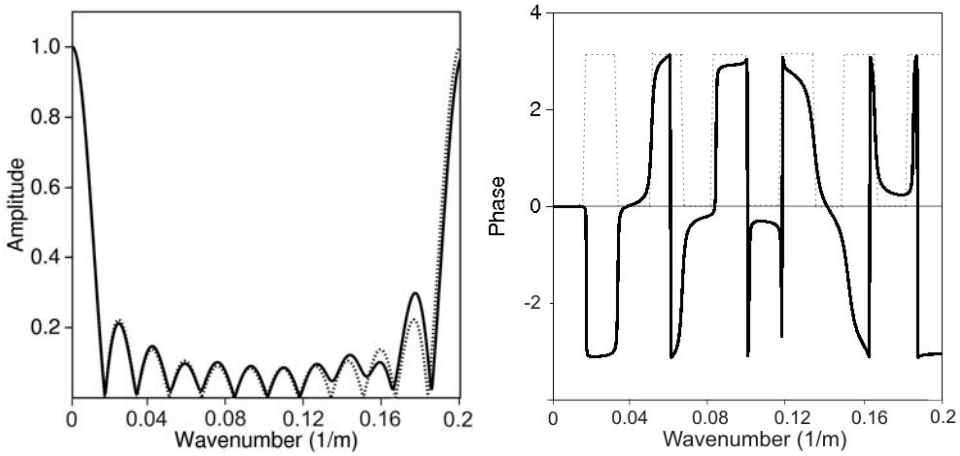

Figure 2.3. Amplitude (left) and phase (right) spectra of array response with (solid line) and without (dashed line) phase variation for all array elements

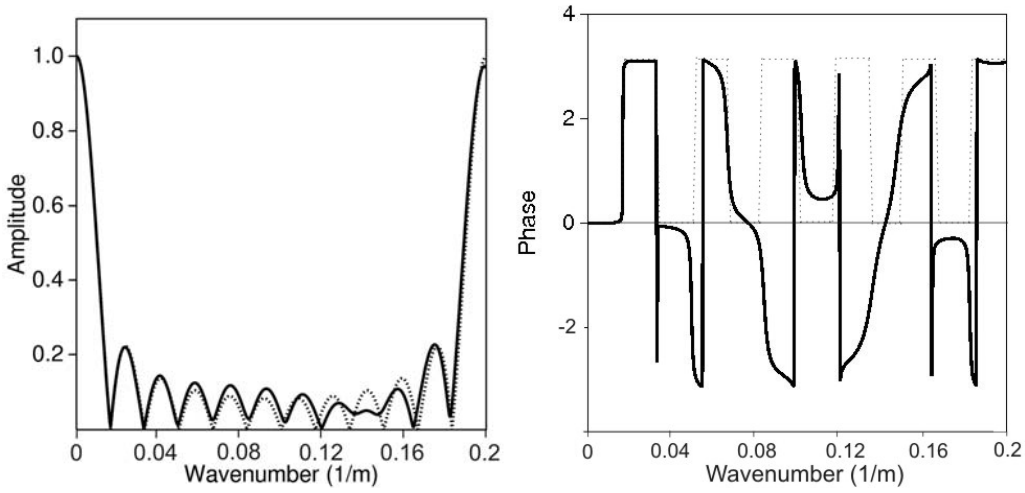

Figure 2.4. Amplitude (left) and phase (right) spectra of array response with (solid line) and without (dashed line) amplitude variation for one array element

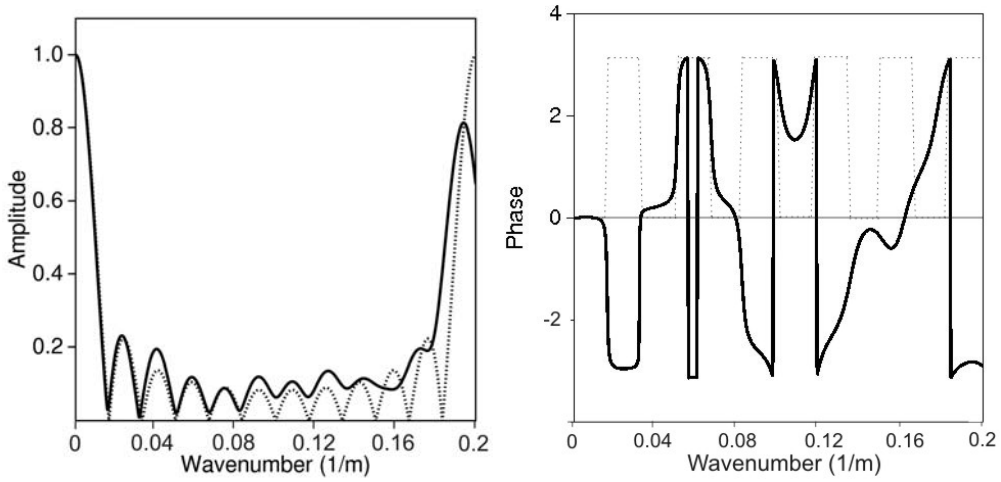

Figure 2.5. Amplitude (left) and phase (right) spectra of array response with (solid line) and without (dashed line) amplitude variation for all array elements

2.2.1.2 Multiple arrays without and with variations

In the previous section, we analyzed the response of one array in the absence and the presence of variations. Here, in order to look at the spatial characteristics, we model multiple arrays using single-sensor recordings as input data. The synthetic single-sensor record contains one linear event, characterized by small apparent frequencies (maximum amplitude at 12 Hz) and low apparent velocity (550 m/s), and one hyperbolic event, characterized by high apparent frequencies (maximum amplitude at 36 Hz) and high apparent velocity (layer velocity 2000 m/s). The thickness of the first layer, from the geological model, is 400 meters. The input wavelet is the Ricker wavelet, i.e., the second derivative of a Gaussian. The spatial sampling interval is again 5 meters; 80 single sensors have been used. The responses of arrays with 12

elements are synthesized and displayed in the time and frequency domain (Figure 2.6); no variations were used in this modeling.

The effect of the array is to improve the signal-to-noise ratio and conduct little distortion of the reflection wavelet. Summing the elementary recordings from array elements has an effect on the reflected waveform. For example, the reflections coming from deep horizons are characterized by small move-out; therefore, the summing will result in a little distortion of the seismic wavelet (see Figure 2.6, right). Regarding the surface waves, the effect is opposite. The output of the first step from array-forming shows an effect which is due to the finiteness of an array, an "edge-effect": two remaining wavelets with significant amplitude are seen on the time interval where the surface waves occurred on initial recordings (Figure 2.6, right). Looking at the amplitude (f, k_x)-spectrum of the single-sensor record, we notice that the energy of the linear event is still significant after summing (Figure 2.7, right). Therefore, the attenuation provided by array-forming is not at all perfect.

Next, we introduce phase variations in the modeling, via irregular positioning of all single sensors; the maximum random variation is 20% of regular spacing of 5 meters. The effect of the phase variations is clear on the records displayed in both domain (Figures 2.8 and 2.9). It is known that, physically, the linear event is more sensitive to the irregular spacing compared with the hyperbolic event; this is sustained by Figures 2.8 and 2.9. Looking at the amplitude (f, k_x)-spectrum, we notice aliased energy that occur as dipping stripes parallel with the energy of the linear event (Figure 2.9). This undesired aliased energy was well attenuated after summing but the noisy energy is still significant.

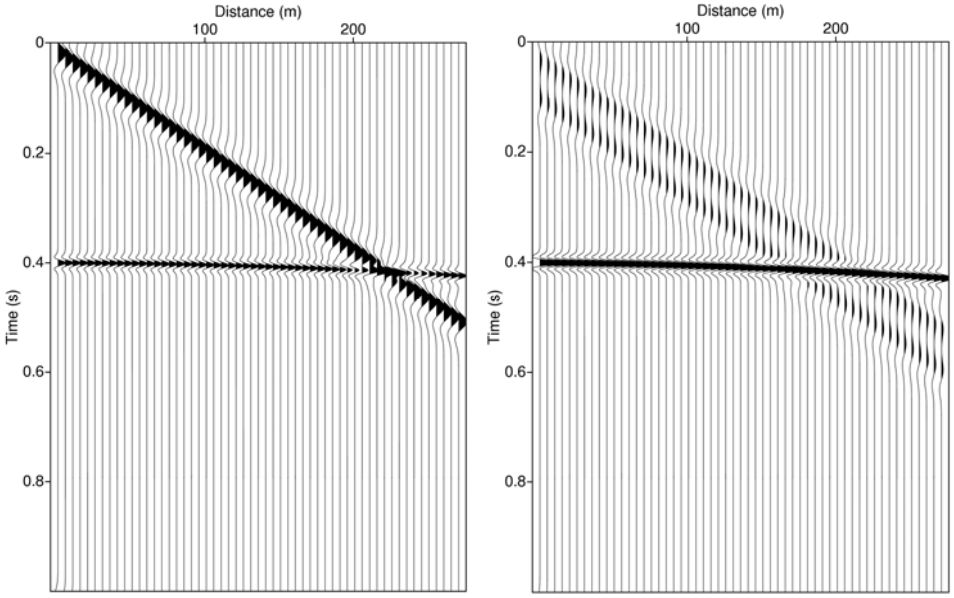

Figure 2.6. Synthetic single-sensor record (left) after standard array-forming (right)

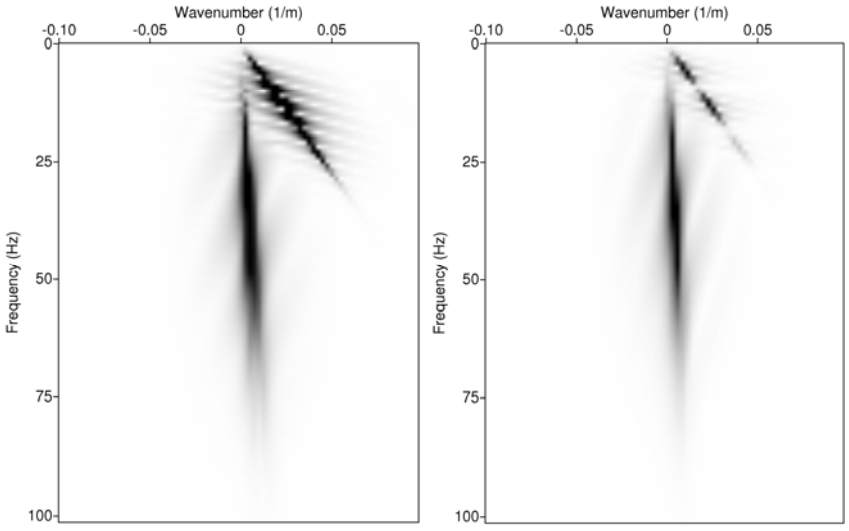

Figure 2.7. Amplitude (f, k_x)-spectrum of synthetic single-sensor record (left) after standard array-forming (right)

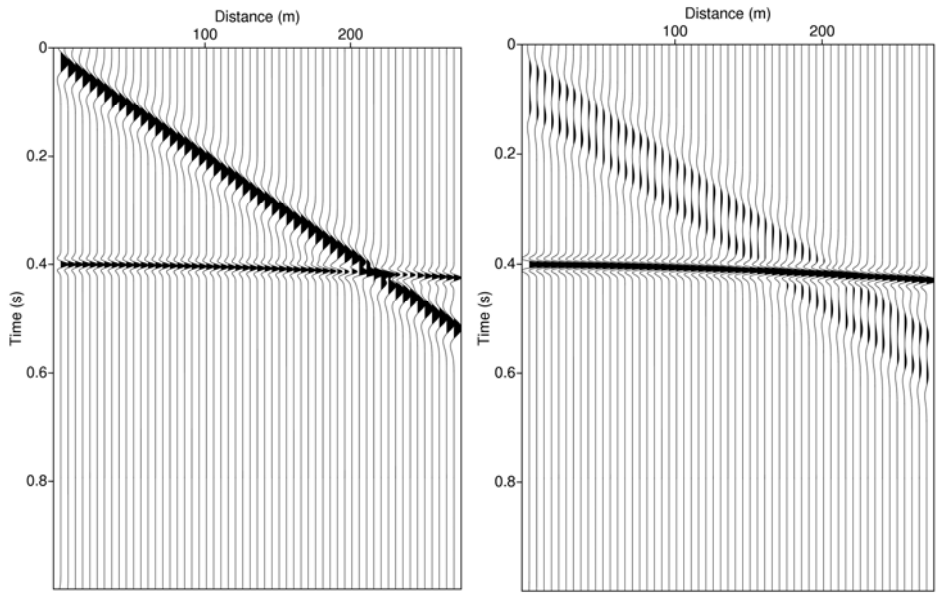

Figure 2.8. Synthetic single-sensor record with irregular positioning, max random variation of 20% from 5 m, (left) after standard array-forming (right)

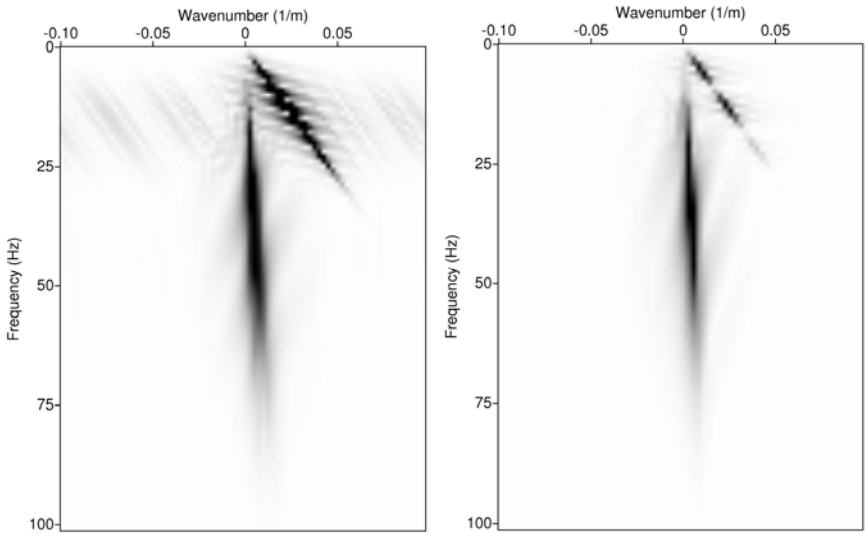

Figure 2.9. Amplitude (f, k_x)-spectrum of synthetic single-sensor record with irregular positioning, max random variation of 20% from 5 m, (left) after standard array-forming (right)

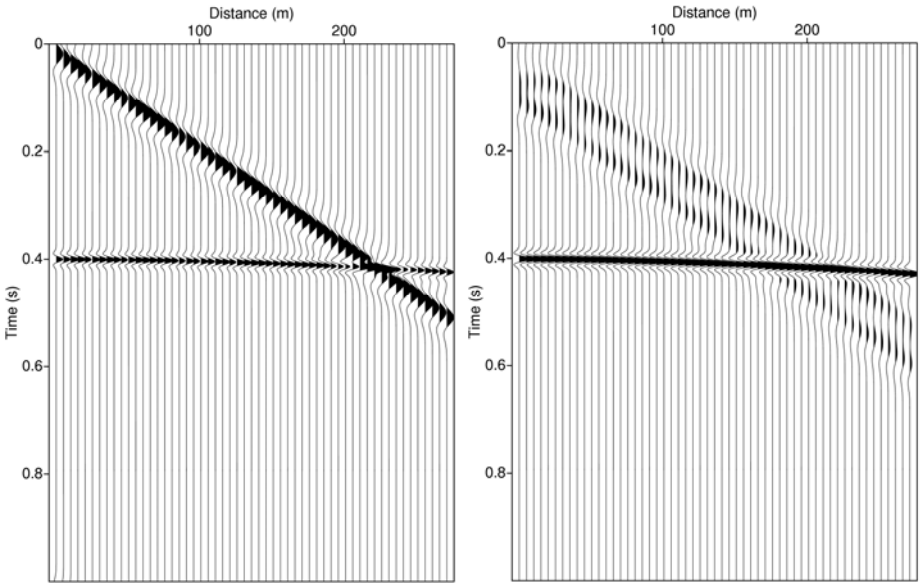

Figure 2.10. Synthetic single-sensor record with amplitude variations, max random variation of 20% , (left) after standard array-forming (right)

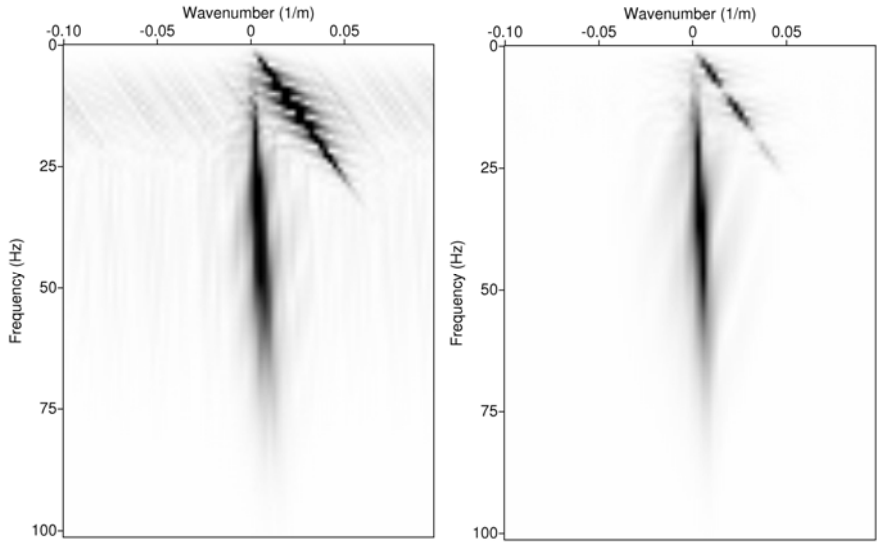

Figure 2.11. Amplitude (f, k_x)-spectrum of synthetic single-sensor record with amplitude variations, max random variation of 20%, (left) after standard array-forming (right)

If we introduce amplitude variations in our modeling, we notice that both arrivals are affected by their presence (Figures 2.10 and 2.11). The variations were computed using a maximum random error of 20% and were introduced as weights applied to all single sensors, before summing them. The aliased energy, an effect of these variations, occurs as dipping stripes parallel with both arrivals (Figure 2.11). Again, the array-forming could attenuate the aliased energy but the linear event, still, shows significant energy (Figure 2.11).

In all examples displayed above, we noticed that the standard array does not perform a good attenuation of the noisy energy and this means that we have to find a better way to do it. We will give a new method which tackles this better in Chapter 3.

2.2.2 Multiple arrays for a field situation

In this section, we want to compare, via modeling, the responses of data acquisition using single sensors and standard arrays in areas with rough topography (hilly and mountainous area). We will analyze the effect of elevation statics and irregular spacing of single sensors on the seismic arrivals. The presence of rough topography causes bad planting of the receivers; the chance to plant them at various distances one to the each other is higher in such areas. In our modeling, we will use a set of elevations measured on the field (Figure 2.12) during the DACIA-PLAN campaign as will be described and used in Chapter 5.

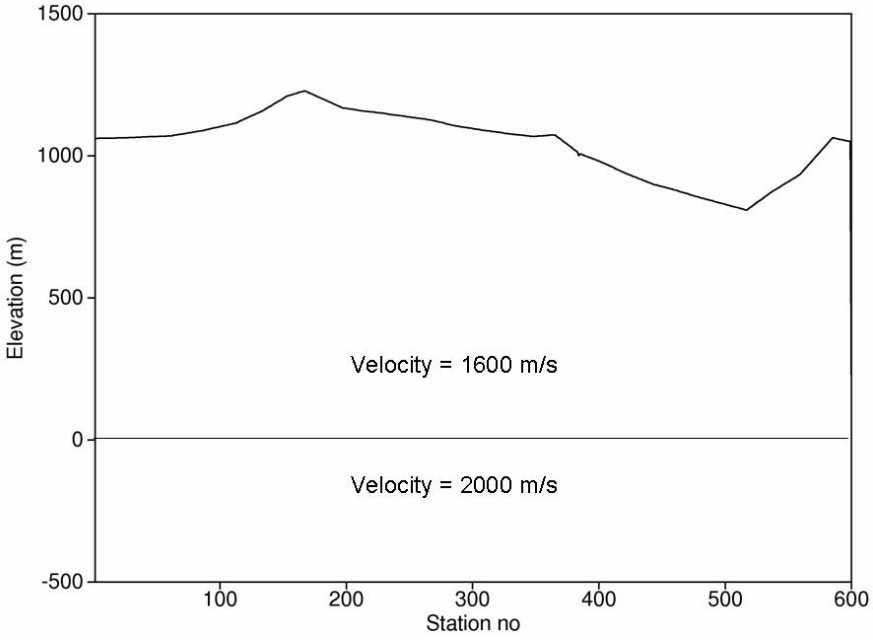

Figure 2.12. Synthetic depth model and elevation profile used in modeling

First, we model 10 records with 49 single sensors spaced at 50 meters; the source spacing is 50 meters and the depth shot is 20 meters. The input wavelet is a Ricker type. The synthetic records contain one linear event, characterized by small apparent frequencies (maximum amplitude at 12 Hz) and slow apparent velocity (600 m/s), and one hyperbolic event, characterized by high apparent frequencies (maximum amplitude at 42 Hz) and high apparent velocity (layer velocity 2000 m/s). The thickness of the first layer is 500 meters. Time sampling interval is 4 ms.

It was shown before that irregular spacing between single sensors has more effect on the linear event, e.g. surface waves, (waves propagating horizontally) and statics have more effect on the reflected waves (waves

propagating vertically). Therefore, we will model the linear event using irregular single-sensor spacing and the hyperbolic event in the presence of elevation statics (Figure 2.13). The source and receiver statics were computed assuming the final datum at 0 meter and a replacement velocity of 1600 m/s.

Now, let us redo the modeling using the same parameters as used above but for standard arrays. We use single sensors spaced at about 5 meters; the maximum random variation is 1 meter (20%). The array response is computed assuming an array of 12 elements and a group interval of 50 meters. The hyperbolic event is affected by elevation statics while the linear event is modeled for irregular single sensor spacing (Figure 2.14).

Array-forming will attenuate the linear event but, unfortunately will destroy the reflection in places where the variation in elevation along the array of single sensors is strong (see Figure 2.15, the reflections from the last 7 traces have very small amplitude and a stretched wavelet).

Based on our modeling responses, we can say that the use of hard-wired arrays in areas with rough topography is not a good choice in order to perform a proper acquisition of the reflected waves. High quality seismic data means not only very low noise level but clear reflections characterized by the highest amplitude possible. We also know that good input data to processing means good processing results.

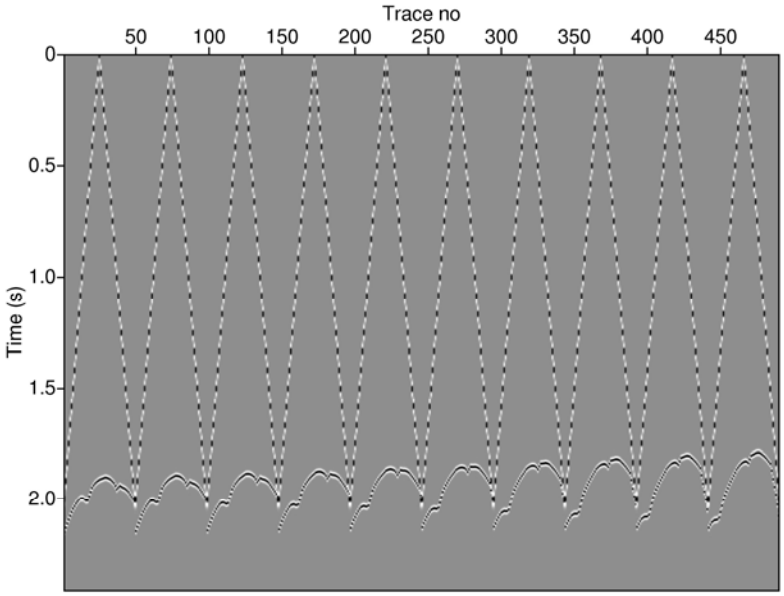

Figure 2.13. 10 synthetic records with single sensors spaced at about 50 m, maximum random variation 1 m, before static corrections

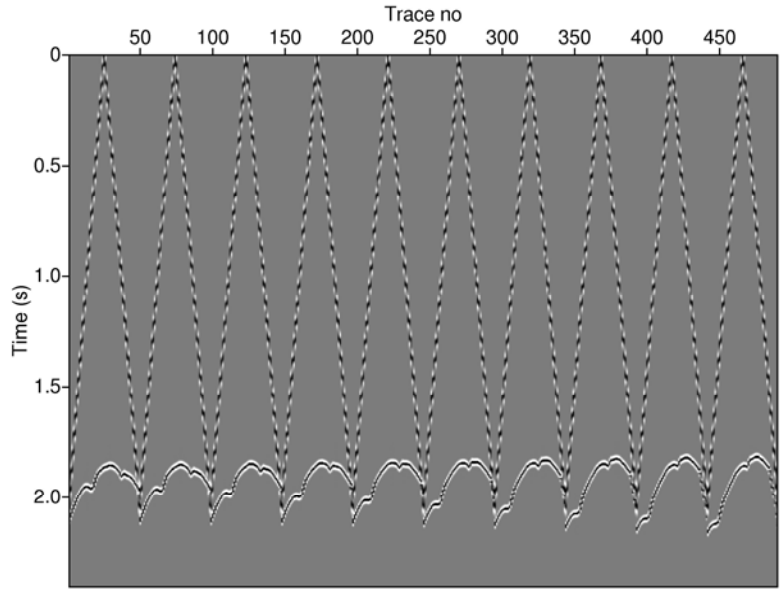

Figure 2.14. 10 synthetic records based on standard array responses, before static corrections

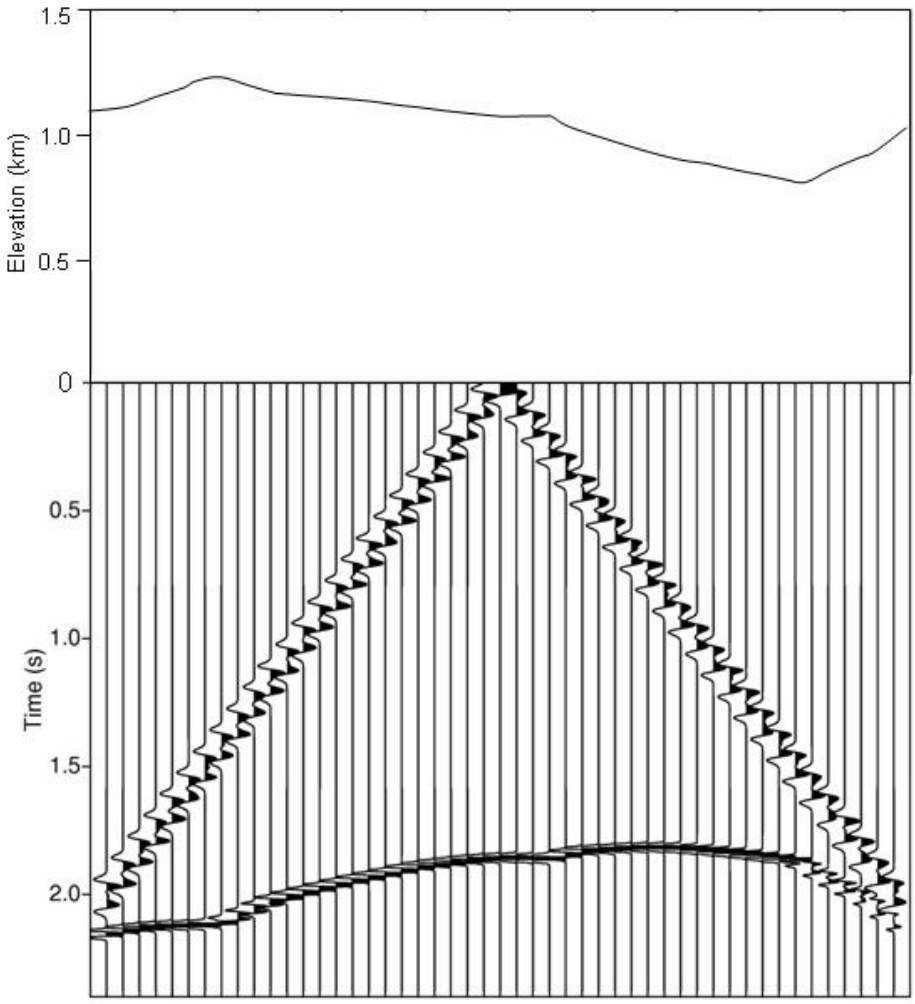

Figure 2.15. One single-sensor record after adding of 12 traces and spatial resampling at 50 m, before static corrections (down) and elevation profile used in modeling (up)

2.3 The use of single sensors in data processing

Let us investigate the effect of single sensors and array forming in processing. To this aim, we process the seismic dataset modeled in the previous section in a very basic way. In this way, we can analyze the effectiveness of the use of single sensors or arrays for data acquisition in hilly or mountainous areas. We can compare the amplitude (f, k_x)-spectrum of these records, the CMP-gathers obtained for both datasets and, at the end, the time sections obtained in both situations. Static corrections are applied at the beginning of the data processing (see Table 2.1). In this way, the effect of elevation statics is nicely removed from the single-sensor data (see Figures 2.16 and 2.18, left). Things are different in case of recordings based on standard arrays. Here, elevation statics affect the array responses since the individual single-sensor recordings were summed before the static corrections were applied (see Figures 2.17 and 2.18, right).

Processing steps	
Input data	10 seismograms in SU format 2.4 s length
Geometry	yes
Elevation static corrections	Final datum = 0 m Replacement velocity = 1600 m/s
Velocity analysis	2000 m/s
NMO correction	yes
Stacking	yes

Table 2.1. Synthetic data processing flow

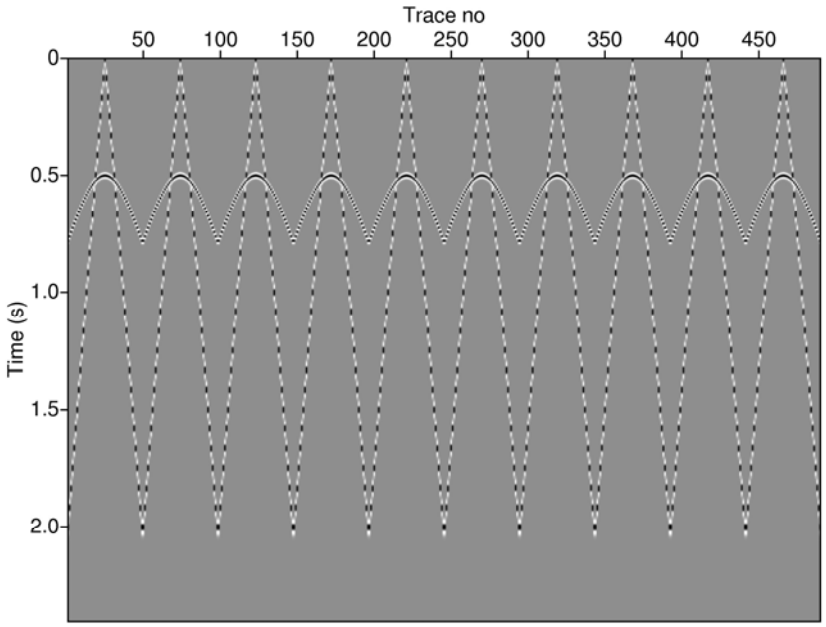

Figure 2.16. 10 single-sensor records, after static corrections

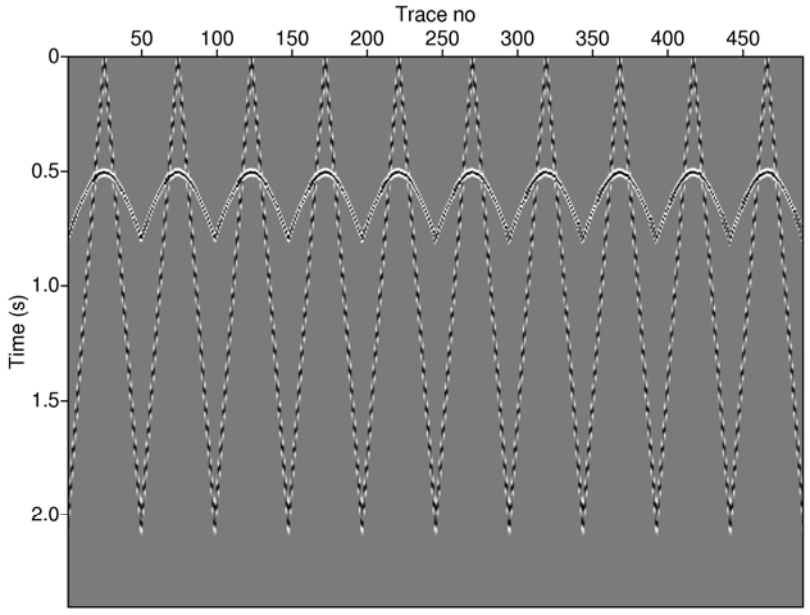

Figure 2.17. 10 synthetic records based on standard array responses, after static corrections

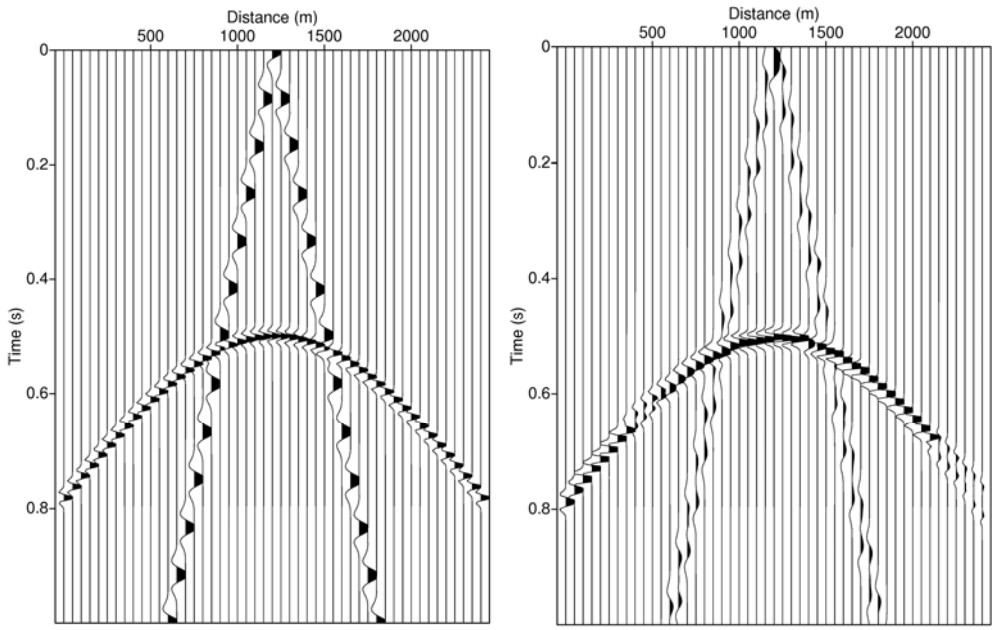

Figure 2.18. Time windowed single-sensor record (left) and one record based on array responses (right) after static corrections

Looking in detail at this effect, we chose two traces from the records displayed in Figure 2.18; we compare the shape and amplitude of both reflections which occur at about 650 ms (Figure 2.19). The reflection seen on the trace selected from the single-sensor record has the maximum amplitude used in modeling and a nice shape of the Ricker wavelet. The other one, being on the response of an array that covered an area with important variations in elevation, is characterized by very small amplitude; in addition, it does not show the shape of the Ricker wavelet any more.

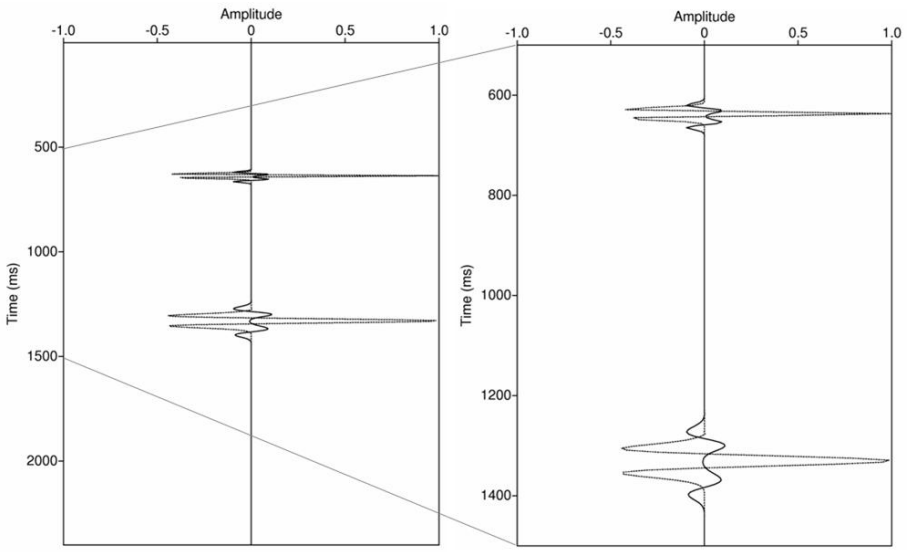

Figure 2.19. Traces from a single-sensor record (dashed line) and from a record modeled using standard-arrays (solid line), after static correction have been applied

We know from modeling that array-forming affects the wavelet of the reflections at large offset where moveout is significant, especially in cases of the shallower arrivals [*Panea et al.* (2003), *Panea et al.* (2004)]. In the presence of other types of variations, e.g. elevation statics, the array-forming will have a higher negative effect on the reflections (Figure 2.19).

Both datasets were sorted to the common-midpoint domain in order to obtain the required input for the velocity analysis, the Normal-Moveout correction and stacking. The hyperbolic events seen on the common-midpoint-gathers (CMP-gathers) differ in terms of the shape of the wavelet and amplitude (Figure 2.20); the CMP-gathers obtained from the single-sensor records contain wavelets with higher amplitude compared with those seen on the CMP-gathers obtained from the records based on standard array responses. The NMO correction is applied in order to flatten the hyperbolic events (Figure 2.21).

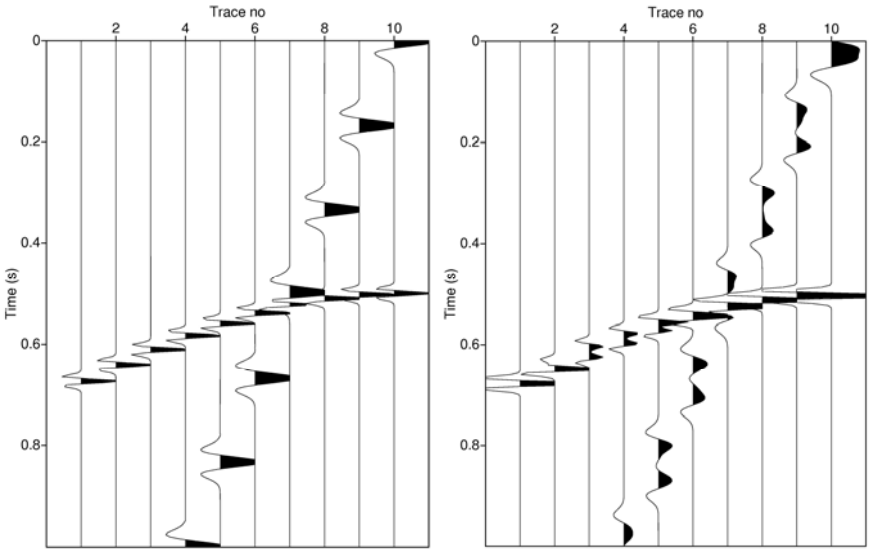

Figure 2.20. CMP-gather from a single-sensor record (left) and from a record based on standard array response (right), before the NMO correction

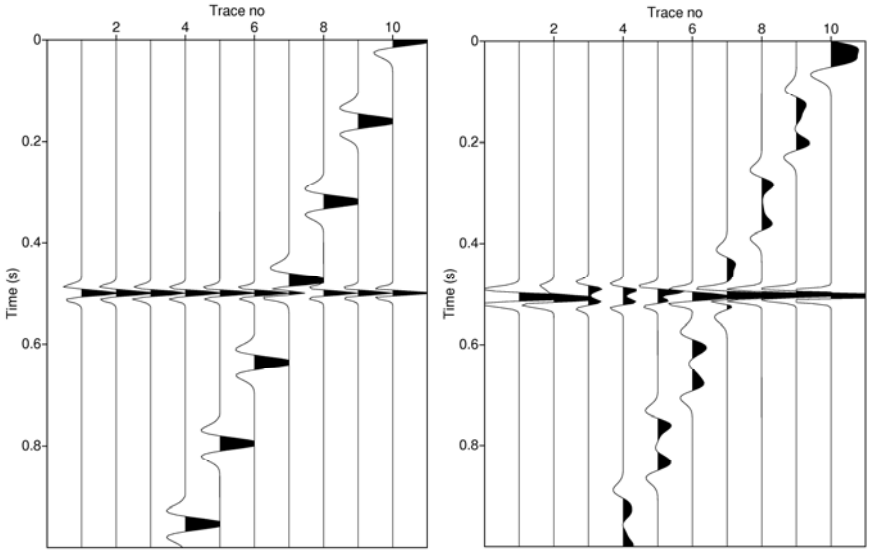

Figure 2.21. CMP-gather from a single-sensor record (left) and from a record based on standard array response (right), after the NMO correction

Stacking of the NMO corrected gathers will give us two different images of the time sections. The time section displayed in Figure 2.22 is based on the single-sensor records. It shows a clear reflection, with high amplitude. The time section displayed in Figure 2.23 is obtained on records based on array responses. The reflection seen here looks different than the other one displayed in Figure 2.22, namely it is not a straight event.

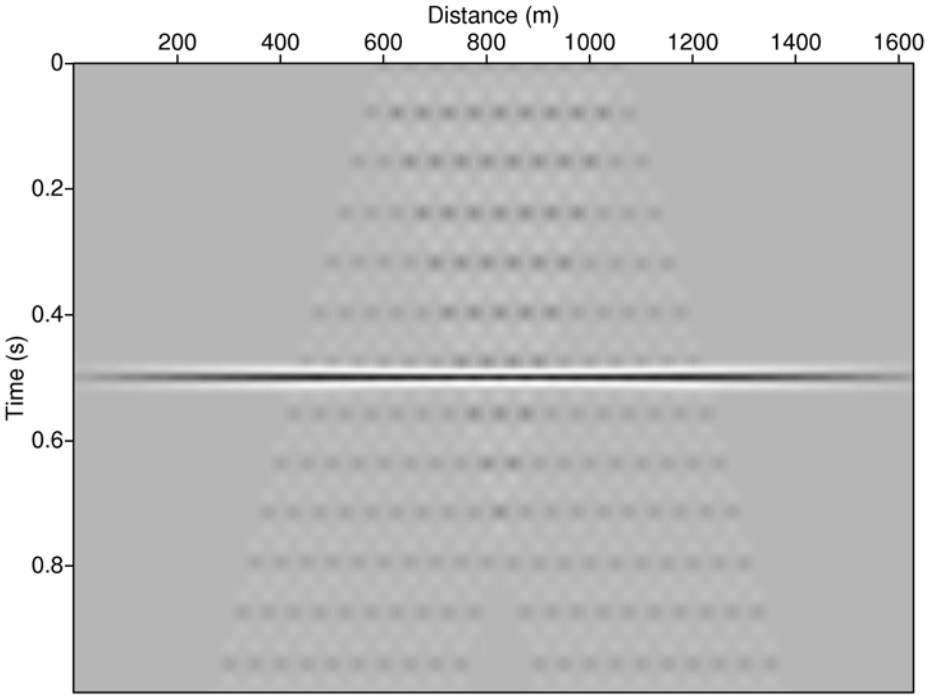

Figure 2.22. Time section obtained for single-sensor records; same display parameters have been used

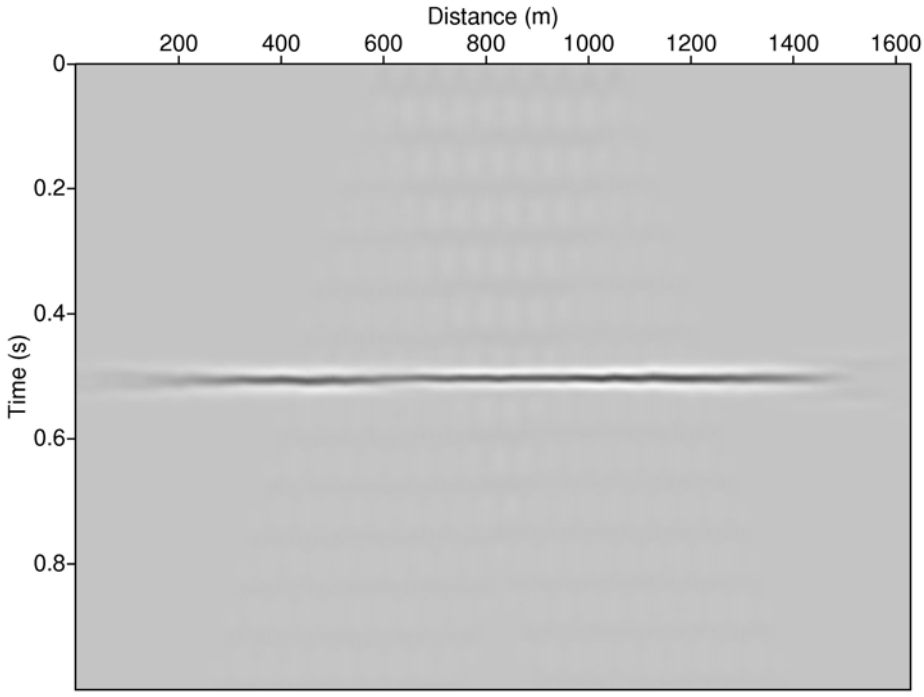

Figure 2.23. Time sections obtained for records based on standard array responses; same display parameters have been used

2.4 The use of single sensors in geological interpretation

In the previous sections, we studied the effectiveness of the use of single sensors or conventional hard-wired arrays in the presence of surface with rough topography. The quality of the processed data influences the accuracy of the image available for the geological interpretation. A reliable subsurface image depends on the information contained by the stacked data and we showed that this information depends, mainly, on the type of acquisition. Usually, the geological interpretation is based on the presence of clear reflections,

characterized by the highest amplitude possible to be obtained from data processing.

Our modeling results showed that the use of single sensors or conventional hard-wired arrays influences the shape and amplitude of the reflections. For a clear image, we chose and displayed one trace from a stack obtained using single-sensor recordings and the same corresponding trace from the stack computed for records based on array responses (Figure 2.24). Looking at these two reflections, we notice that the amplitude of the reflection from the time section based on single-sensor records is almost double that of the section based on conventional hard-wired arrays responses. The noisy wavelets seen on the trace chosen from the section based on single-sensor records are still significant in amplitude because we did not apply a filter during data processing. We assumed that stacking would partially attenuate them. On the other trace, these noisy wavelets have very small amplitude as an effect of array-forming and stacking. This is the advantage of using arrays in data acquisition but with the cost of reflections, as we could see in our modeled field situation.

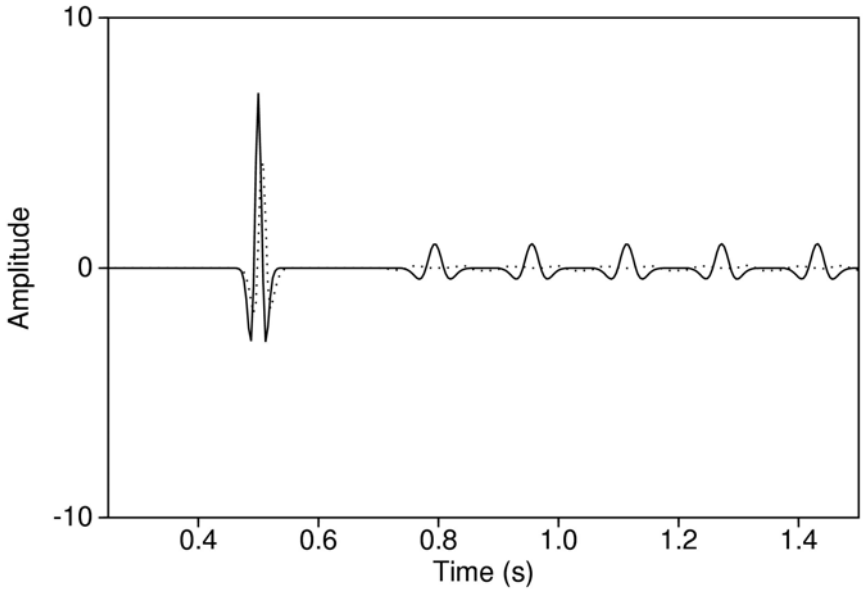

Figure 2.24. Traces chose from a time section based on single-sensor records (dashed line) and records based on array responses (solid line)

The reflection amplitude is very important in interpretation. Typically, any change in the amplitude reflects a variation in the physical properties of the subsurface. We avoided introducing modeling parameters that can affect the amplitude. In this way, we assume that we control the amplitude variations seen on the time sections. In our modeling, only array-forming and stacking have an effect on the reflection amplitude.

Looking at the reflection displayed in Figure 2.26, we notice a lateral variation in amplitude. Usually, in the field situation, this type of variation occurs due to the presence of different fluids (oil, gas, water) combined with lateral variation of the densities, velocities (e.g. lateral variation of lithology). All of them have an effect on the contrast in acoustic impedance and, therefore, on the reflection amplitude. In our case, these amplitude variations are caused

by the use of conventional hard-wired arrays on a surface with rough topography. In the previous sections, we showed the effect of array-forming on the reflection contained by the common source- or CMP-gathers and, as a consequence, this effect has to occur on the stacked data.

Also, by comparing the images of both time sections, we notice that some of the reflections seen on the section obtained using records based on conventional arrays occur at *false* times (see Figures 2.25 and 2.26). The geological model used in modeling contains one horizontal interface, therefore the time sections should show it. It does not matter if we analyze an un-migrated or migrated time section because the reflections occur at the same position in time on both. The reflection seen on the time section displayed in Figure 2.25 shows a perfect *planar* horizontal limit. In the other example, the conventional hard-wired array case, the reflection shows us a false *rough* horizontal limit. Locally, the time differences between the reflections seen on both stacks at the same position are large, about tens of milliseconds.

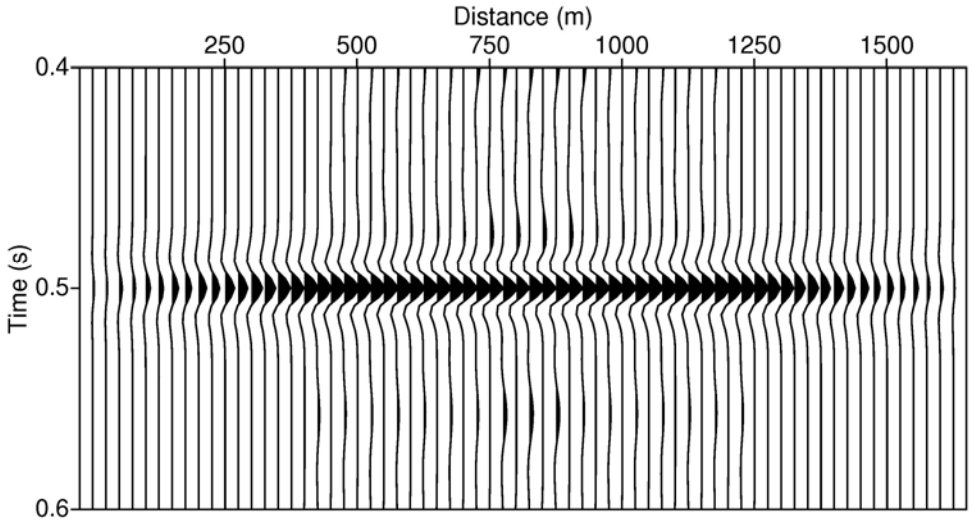

Figure 2.25. Time windowed section obtained for single-sensor records

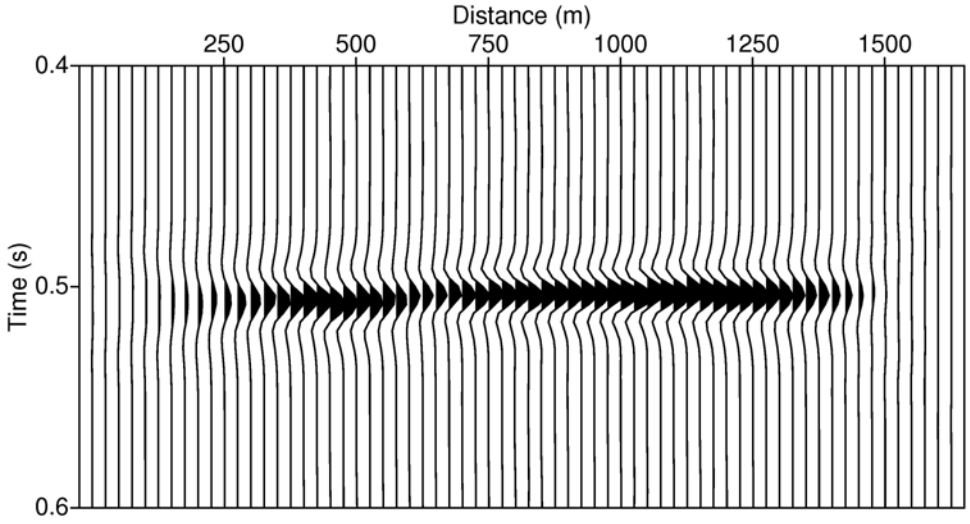

Figure 2.26. Time windowed section obtained for records based on standard array responses

Finally, it is clear from these simple examples that when single-sensor data are being used it becomes possible to see events which would otherwise be missed or destroyed by data from conventional hard-wired arrays. This issue is exploited in Chapter 5 where acquisition has taken place in an area with rough topography. Single-sensor recordings allowed reflections to be revealed which had an impact on the geological interpretation.

2.5 Conclusions

The purpose of this chapter was to describe and analyze the main problem from data acquisition, namely the attenuation of the noisy seismic arrivals. The surface waves are the least desirable arrivals identified on land seismic data and, therefore, have to be attenuated. We provided a brief description of the receiver arrays at the beginning of this chapter. Also, we made an introduction to the variations that can affect the array-forming responses.

We modeled the response of single and multiple arrays in the absence and presence of phase and amplitude variations and we noticed that the phase variations have more significant effect on array response compared to the amplitude variations. Both of them affect the amplitude and phase spectrum of the array response. By modeling arrays using single-sensor records, we showed that the attenuation of the surface waves is not satisfactory. The remaining waves are still significant in amplitude and energy. This means that we have to find another algorithm to do it (Chapter 3).

We also studied the effectiveness of using single sensors or standard arrays in areas with rough topography. We showed that single sensors work better in such areas. We also showed that there are field situations when the standard array responses are strongly affected by the phase variations. Statics

can distort irreparably the shape of the reflections when using conventional arrays since they are destroyed in the array-forming. Single-sensor recordings allow static corrections (or other processing, as will be shown in Chapter 3), to be applied at an earlier stage in data processing.

The effects of intra-array variations in the data processing were also shown. It affects the CMP gathers with its associated velocity-model building. Single-sensor data will be used for velocity-model estimation in Chapter 4.

The effects of variation are also shown on stack level, representing un-migrated time sections, and show very clear the effects of intra-array variations on the reflections. This will further be exploited for geological purposes in Chapter 5.

Chapter 3

The use of single sensors in data acquisition: Robust Minimum Variance Distortionless Response (MVDR) beamformer[1]

3.1 Introduction

In the last years, the channel count has increased dramatically. This has allowed seismic explorers to question the use of hard-wired arrays in the field. Conventionally, seismic arrays were needed to reduce the amount of data. This reduction then put some requirements on the data, the most important one being that reflections, seen as the desired signal here, should not be spatially aliased. The nastiest arrival on land is the ground-roll that requires a much finer spatial sampling than the reflections. Therefore, as *Vermeer* (1990) has stated, the array should work as a spatial antialias and resampling operator. However, nowadays with high channel counts, fast data transfer and storage, the array

[1] This chapter is completely based on: Panea, I., and Drijkoningen, G., 2007. The data-adaptive MVDR beamformer on seismic single sensor data, paper submitted to Geophysics.

should not be considered as a hard-wire-connected array any more but as a digital array that can be treated by more sophisticated digital array processing.

Digital array-processing is being used in many fields. A common denominator in array processing is the so-called beamformer. A beamformer is a processor applied to data from an array of sensors in order to increase the signal-to-noise ratio. It belongs to the class of spatial filters used in case of data where signals and noise are overlapping in frequency content but coming from different spatial directions [*Van Veen and Buckley* (1988), *Van Veen* (1991)]. In a beamformer, weights are applied to single array-elements to create a "beam".

In general, beamformers can be data-independent, statistically optimum, data-adaptive and partially data-adaptive, depending on the procedure to determine the weights [*Van Veen and Buckley* (1988)]. In case of data-independent beamformers the weights are fixed so independent of the received data. For statistically optimum beamformers, the weights are based on the statistics of the array. The statistics of the array data are usually not known and may change over time so adaptive algorithms can be employed. The data-adaptive beamformer is designed such that the response is optimal based on the data themselves. Partially data-adaptive beamformers are designed in order to reduce the computational load and cost of the data-adaptive algorithms.

It was demonstrated that, under ideal conditions, the data-adaptive beamformers achieve a better signal-to-noise ratio in comparison with the conventional beamformers [*Feldman and Griffiths* (1994)]. Also, it was shown that the responses of data-adaptive beamformers are sensitive to mismatches between the presumed and actual array responses. An example of possible mismatches and a solution to deal with them are given in *Shahbazpanahi et al.* (2003). In addition, the quality of data-adaptive beamformers depends on the number of analyzed data samples used in the data covariance matrix.

Different types of data-adaptive beamformers have been proposed in the last two decades. For the specific case of the mismatches between the presumed and actual signal-look directions, algorithms have been developed like the Linearly Constrained Minimum Variance (LCMV) beamformer [see *Johnson and Dudgeon* (1993)], signal blocking-based algorithms [*Godara* (1986)] and Bayesian beamformer [*Bell et al.* (2000)]. An analysis of the performance of the MVDR beamformers in the presence of errors in signal-look directions was done by *Wax and Anu* (1996). Another approach in the presence of unknown arbitrary-type mismatches of the desired signal array response is proposed in the Minimum Variance Distortionless Response (MVDR) beamformer [*Monzingo and Miller* (1980), *Vorobyov et al.* (2003), *Jian et al.* (2003)].

Due to its properties, the Robust MVDR beamformer, presented in this chapter, is suitable for dealing with seismic data since it uses matrices computed based on raw single-sensor seismic data containing both desired signal and noise. Its purpose is to compute weights that will be applied to each group of recordings of single elements, before their summation. These weights will be different from one group to another because of the different data covariance matrices in the weight definition formula; in this way we can define a proper data-adaptive beamformer.

3.2 Design of a Robust MVDR Beamformer

In this section we will describe the Robust MVDR beamformer as derived in *Shahbazpanahi et al.* (2003). We start with the classic MVDR beamformer definition which is based on the knowledge of two types of record, one with noise (interference) and the other with a desired signal. In seismic exploration the desired signal is defined as the primary reflected energy

whereas the noise is defined as anything but primary reflected energy, such as multiply reflected and refracted waves, diffractions, and surface waves. The surface waves, also known as ground roll, are very dominant in land seismic data. Their attenuation is difficult to define because their frequency content overlaps with that of the reflected waves. Furthermore, the surface wave is frequently affected by spatial aliasing arising from the receiver spacing chosen for acquisition. A traditional effective way to attenuate the surface wave signal is to use an appropriate receiver array. The spacing between array elements is arranged such that good reception of the surface waves is permitted. This means no spatial aliasing, and the size of a group interval is chosen so that the reflected waves are not spatially aliased.

A beamformer can be designed in combination with an array of receivers with its purpose being to compute weights based on single element recordings and to apply the weights to individual recordings before summing them into the beam. It can be used to filter out the arrivals coming from other directions than that of the desired signal. Our aim is to derive a beamformer such that a desired signal (reflected wave) is enhanced, or at least not cancelled, and interfering signals (surface wave) are attenuated, or cancelled if possible.

In general, in seismology signals are wideband, whereas in standard array processing literature many adaptive beamforming algorithms are derived under narrowband conditions, so that these beamformers can be frequency independent. But, the design and application of a narrowband beamformer can be meaningful taking into account that the standard hard-wired arrays, also frequency independent, are used in reflection seismology for noise attenuation [*Anstey* (1986)].

The formula of the output signal of a spatial filter (beamformer or standard array) is well-known, it is defined by the sum of weighted individual recordings coming from the array elements. These weights can be all equal to 1

and this is the case of standard hard-wired arrays (as showed in Chapter 2); this is appropriate for the enhancement of a desired signal characterized by a small moveout, including at large offsets. Signals coming from other directions, e.g. surface waves, will be attenuated (as shown in Chapter 2) but sometimes not very well, depending on their characteristics (e.g. velocity, frequency).

Therefore, our aim in this chapter is to take this a step further. We still consider frequency-independent beamformers, but design them data-adaptive, such that an interfering signal (e.g. a surface wave) is attenuated as much as possible. We first need to show under what conditions this is reasonable.

In principle, the data model for which this filter is applied is that of a narrowband signal. For such a signal, the small delay that occurs in going from one sensor to the next one can be replaced by a phase shift. If $s_o(t)$ is an analytic complex signal, representing a narrowband signal, with center frequency ω, then for a sufficiently small delay τ, we have:

$$s_o(t-\tau) \cong e^{-j\omega\tau} s_o(t). \tag{3.1}$$

For the i-th sensor in the array, we can write:

$$s_o(t-\tau_i) \cong e^{-j\omega\tau_i} s_o(t), \tag{3.2}$$

and for a received signal vector:

$$\mathbf{d}_o(t) = \mathbf{a}\, s_o(t), \tag{3.3}$$

where the vector **a** has as component for the i-th sensor $a_i = e^{-j\omega\tau_i}$.

A beamformer to cancel this signal is a beamformer whose weight vector **w** is orthogonal to **a**, in that case $\mathbf{w}^T \mathbf{d}_o(t) = 0$.

If $s_o(t)$ is a real narrowband signal, and not complex analytic, the received signal vector will be of the form:

$$\mathbf{d}_o(t) = \mathbf{a}_{o1} s_{o1}(t) + \mathbf{a}_{o2} s_{o2}(t), \tag{3.4}$$

where $\mathbf{a}_{o1}$ and $\mathbf{a}_{o2}$ are two vectors that depend on the delays and center frequency, but are not time-dependent. In order to cancel $\mathbf{d}_o(t)$, the weight vector **w**, provided by the beamformer, has to be orthogonal to both vectors $\mathbf{a}_{o1}$ and $\mathbf{a}_{o2}$.

Here, the unknown vector is the weight vector **w**. In order to estimate it, we denote with $\mathbf{D}_o = [d_o(t_1), d_o(t_2), \ldots, d_o(t_N)]$ the data matrix that contains the recorded data sampled at the time sampling interval. Next, this matrix is used to compute the covariance matrix:

$$\mathbf{R}_{do} = \frac{1}{N_t} \mathbf{D}_o \mathbf{D}_o^T, \tag{3.5}$$

where N_t is the total number of time samples.

The eigenvalue decomposition of $\mathbf{R}_{do}$ will reveal that it is of rank 2, meaning that there are two nonzero eigenvalues and the others are zero, with column span formed by the span of $[\mathbf{a}_{o1}\ \mathbf{a}_{o2}]$. The beamformer weight vector **w** can be any eigenvector corresponding to the "zero" eigenvalues or to a linear combination thereof.

The required narrowband condition is:

$$\tau_{\max} BW \ll 1, \tag{3.6}$$

where τ_{max} is the maximum delay and BW is the bandwidth of the signal.
In case of wideband signals with delays that are not too large, the product between the maximum delay and bandwidth could in the limit be almost equal to 1. In that case the covariance matrix will not be exactly of rank 2; therefore the "zero" eigenvalues are small but non-zero. Thus, the undesired signals can be attenuated but not completely canceled. This fact can be used in seismology, when sensors are closely spaced.

In reflection seismology noise need to be separated from the reflections. Noise in active seismology is mainly coherent noise. On land seismic data, the most important coherent noises are the surface waves since they dampen much more slowly than body waves; there are considered the highest energy wave types. In seismic records, where seismic sensors are laid out along lines at the surface, surface waves show up as linear events; they also show a dispersive character and there are characterized by low frequencies (up to max 16 Hz). Since surface waves travel along the surface, they have a low apparent velocity. This is in complete contrast to the reflections, which not only have a higher velocity but also come from below so nearly arrive vertically.

The simplest data model, that can approximate signal and noise in reflection seismology, can be written as follows:

$$\mathbf{d}\,(t) = \mathbf{s}\,(t) + \mathbf{n}\,(t), \tag{3.7}$$

where **d** (t) is the vector of recorded data from one array (M entries for an array with M sensors), **s** (t) is the part of the data that contains mostly the desired signal (reflected wave) and **n** (t) is the noise part of the data that contain the

undesired signals (surface wave). We will assume that both desired and undesired signals can be considered narrowband.

Let $\mathbf{w} = [w_1, w_2, \ldots w_M]^T$ be a M × 1 weight vector to be determined, based on an array with M elements. The output of the beamformer is a signal $y(t) = \mathbf{w}^T \mathbf{d}(t)$. With N_t is the number of available time samples, the output power of y(t) is estimated as:

$$E = \sum_{t=1}^{N_t} |y(t)|^2. \tag{3.8}$$

Define a matrix **D** that collects all sample data vectors, $\mathbf{D} = [\mathbf{d}(1), \mathbf{d}(2), \ldots, \mathbf{d}(N_t)]$ and define the sample covariance matrix as:

$$\mathbf{R} = \frac{1}{N_t} \mathbf{D}\mathbf{D}^T, \tag{3.9}$$

where **R** is a positive semidefinite matrix of size M × M. Then, $E = \mathbf{w}^T \mathbf{R}\, \mathbf{w}$. Since **d**(t) is the sum of a signal and a noise term, we can define the signal power at the output of the beamformer as $E_s = \mathbf{w}^T \mathbf{R_s}\, \mathbf{w}$, and the noise power as $E_n = \mathbf{w}^T \mathbf{R_n}\, \mathbf{w}$, where the sample covariance matrices $\mathbf{R_s}$ and $\mathbf{R_n}$ are defined as:

$$\mathbf{R}_s = \frac{1}{N_t} \mathbf{D_s} \mathbf{D_s}^T, \ \mathbf{R}_n = \frac{1}{N_t} \mathbf{D_n} \mathbf{D_n}^T, \tag{3.10}$$

where $\mathbf{D_s}$, $\mathbf{D_n}$ are M × N_t matrices that contain the desired signal and noise samples, respectively.

The signal-to-noise ratio, denoted by *SNR*, can be defined as:

$$SNR = \frac{\mathbf{w}^T \mathbf{R}_s \mathbf{w}}{\mathbf{w}^T \mathbf{R}_n \mathbf{w}}. \tag{3.11}$$

The aim is to select a weight vector **w** such that the *SNR* is maximized. Above all, we need to protect the desired signal. This is guaranteed by requiring that $\mathbf{w}^T\mathbf{R}_s\mathbf{w} = 1$, which means that there is no signal cancellation [*Shahbazpanahi et al.* (2003)]. Since maximizing the *SNR* is equal to minimizing the noise, the weights for a maximal *SNR* are obtained from the following minimization equation:

$$\min_{\mathbf{w}} \mathbf{w}^T \mathbf{R}_n \mathbf{w} \text{ subject to } \mathbf{w}^T \mathbf{R}_s \mathbf{w} = 1. \tag{3.12}$$

This defines the general type of Minimum Variance Distortionless Response (MVDR) beamformer. The standard MVDR beamformer was proposed by *Capon* (1969) and more adaptive versions were proposed and studied in the following years [see *Zoltowski* (1988), *Van Veen* (1991), *Raghunath and Reddy* (1992), *Harmanci et al.* (2000)]. The high resolution, low sidelobes and good interference suppression are some properties of the MVDR beamformer.

The solution to the minimization problem in Equation 3.12 may be found using the Lagrange multipliers method, which is commonly used to find the minimum of linear functions [*Shahbazpanahi et al.* (2003), *Vorobyov et al.* (2003)]. We define a Lagrangian function $L(\mathbf{w},\lambda)$, as a sum between the objective function $\mathbf{w}^T\mathbf{R}_n\mathbf{w}$ and the constraint 1 - $\mathbf{w}^T\mathbf{R}_s\mathbf{w}$:

$$L(\mathbf{w},\lambda) = \mathbf{w}^T \mathbf{R}_n \mathbf{w} + \lambda(1 - \mathbf{w}^T \mathbf{R}_s \mathbf{w}). \tag{3.13}$$

In the function $L(\mathbf{w},\lambda)$, $\mathbf{w}$ is an unknown optimal weight that has to be determined and used to compute the MVDR beamformer response. In order to do this, we calculate the gradient of the Lagrangian function as a function of weight vector $\mathbf{w}$ components and the Lagrange multiplier λ and equating them to zero:

$$\begin{cases} \dfrac{\partial L}{\partial w_1} = \dfrac{\partial}{\partial w_1}\left[\mathbf{w}^T\mathbf{R}_\mathbf{n}\mathbf{w} + \lambda\left(1 - \mathbf{w}^T\mathbf{R}_\mathbf{s}\mathbf{w}\right)\right] = 0 \\ \dfrac{\partial L}{\partial w_2} = \dfrac{\partial}{\partial w_2}\left[\mathbf{w}^T\mathbf{R}_\mathbf{n}\mathbf{w} + \lambda\left(1 - \mathbf{w}^T\mathbf{R}_\mathbf{s}\mathbf{w}\right)\right] = 0 \\ \ldots\ldots \\ \dfrac{\partial L}{\partial w_M} = \dfrac{\partial}{\partial w_M}\left[\mathbf{w}^T\mathbf{R}_\mathbf{n}\mathbf{w} + \lambda\left(1 - \mathbf{w}^T\mathbf{R}_\mathbf{s}\mathbf{w}\right)\right] = 0 \\ \dfrac{\partial L}{\partial \lambda} = \dfrac{\partial}{\partial \lambda}\left[\mathbf{w}^T\mathbf{R}_\mathbf{n}\mathbf{w} + \lambda\left(1 - \mathbf{w}^T\mathbf{R}_\mathbf{s}\mathbf{w}\right)\right] = 0. \end{cases}$$

(3.14)

Carrying out the derivatives, this result in the system:

$$\begin{cases} \mathbf{R}_\mathbf{n}\mathbf{w} - \lambda\mathbf{R}_\mathbf{s}\mathbf{w} = 0 \\ 1 - \mathbf{w}^T\mathbf{R}_\mathbf{s}\mathbf{w} = 0. \end{cases} \tag{3.15}$$

The first equation from the system can be written as [*Shahbazpanahi et al.* (2003), *Gershman* (1999)]:

$$\mathbf{R_n w} = \lambda \mathbf{R_s w},$$

(3.16)

where the Lagrange multiplier λ can be viewed as a generalized eigenvalue. Because $\mathbf{R_n}$ and $\mathbf{R_s}$ matrices are positive and semi-definite, λ is always a real and positive number. Multiplying the Equation 3.16 by $\mathbf{R_n}^{-1}$ we can rewrite it as:

$$\mathbf{R_n}^{-1}\mathbf{R_s w} = \frac{1}{\lambda}\mathbf{w}. \tag{3.17}$$

Since λ is positive, it follows that the minimum eigenvalue in Equation 3.16 correspond to the maximum eigenvalue in Equation 3.17. Based on this, we can say that the optimal weight vector is given by the principal eigenvector of the product between the inverse of the noise covariance matrix, $\mathbf{R_n}$, and the signal covariance matrix, $\mathbf{R_s}$, [*Shahbazpanahi et al.* (2003)]:

$$\mathbf{w}_{opt} = P\{\mathbf{R_n}^{-1}\mathbf{R_s}\}, \tag{3.18}$$

where $P\{\cdot\}$ is the operator that yields the principal eigenvector of a matrix, i.e., that corresponds to the maximal eigenvalue. But, the Equation 3.18 is applicable only up to a scaling. The correct scaling is found using $\mathbf{w^T R_s w} = 1$. Therefore, we define a vector $\mathbf{v}_1 = P\{\mathbf{R_n}^{-1}\mathbf{R_s}\}$ and then the optimal weight vector is given by:

$$\mathbf{w}_{opt} = \frac{\mathbf{v}_1}{\sqrt{\mathbf{v}_1 \mathbf{R}_s \mathbf{v}_1}}. \tag{3.19}$$

Thereafter, the output of the MVDR beamformer, y, is obtained as follows:

$$\mathrm{y}(t) = \mathbf{w}_{opt}^T \mathbf{d}(t). \tag{3.20}$$

This MVDR beamformer is difficult to apply to seismic data with the understanding that a seismic recording contains both signal and noise. Separate records for these components can be derived via processing techniques or seismic modeling, but their accuracy is altered and we know from previous studies that the effectiveness of the adaptive beamforming algorithms is affected by the presence of diverse errors [*Shahbazpanahi et al.* (2003), *Vorobyov et al*. (2003)].

To avoid using records with noise only, it is desirable for seismic purposes to find another definition of the MVDR beamformer that involves the entire data set, meaning records that contain both signal and noise. We assume that the total signal is dominantly surface wave energy so we can replace $\mathbf{R_n}$ with $\mathbf{R_d}$. The data covariance matrix, $\mathbf{R_d}$, is computed based on the records with signal and noise:

$$\mathbf{R_d} = \frac{1}{\mathrm{N_t}} \mathbf{D_d} \mathbf{D_d}^T, \tag{3.21}$$

where $\mathbf{D_d}$ is an M × $\mathrm{N_t}$ data matrix, M is the number of array elements, and $\mathrm{N_t}$ is the number of time samples. Equation 3.18 can then be written as:

$$\mathbf{w}_{opt} = P\{\mathbf{R_n}^{-1}\mathbf{R_s}\} \cong P\{\mathbf{R_d}^{-1}\mathbf{R_s}\}\,. \tag{3.22}$$

The replacement of the noise covariance matrix with the data covariance matrix was analyzed in the paper of *Reed et al.* (1974). This replacement was necessary because, in practical situations, the noise (with or without interference) covariance matrix is unavailable. It was shown that if the signal component is present in the training data, this replacement decrease the performance of the beamformer whose weights are determined using Equation 3.22, known as the Sample Matrix Inverse beamformer [*Reed et al.* (1974), *Shahbazpanahi et al.* (2003), *Vorobyov et al*. (2003)]. Therefore, other algorithms that define robust adaptive beamformers were proposed. For example, algorithms were developed in the presence of arbitrary unknown steering vector mismatches [*Vorobyov et al.* (2003)] or in the presence of mismatches between the presumed and actual desired response [*Shahbazpanahi et al.* (2003)].

Based on Equation 3.22, the optimal weights are computed using the entire data. One disadvantage is introduced through the use of the signal covariance matrix, $\mathbf{R_s}$, because it is a source of error that can degrade the quality of the MVDR beamforming response. To prevent this, we can introduce a matrix error $\mathbf{\Delta}$ in the definition of the signal covariance matrix such that it represents the possible mismatch between the presumed, $\mathbf{R_s}$, and actual signal, $\acute{\mathbf{R}}_\mathbf{s}$, covariance matrices:

$$\acute{\mathbf{R}}_\mathbf{s} = \mathbf{R_s} + \mathbf{\Delta}, \tag{3.23}$$

where $\mathbf{\Delta}$ is an M × M unknown, positive, semidefinite error matrix that describes the mismatch between the presumed $\mathbf{R_s}$ and actual $\acute{\mathbf{R}}_\mathbf{s}$ signal

covariance matrices. The norm of this matrix $\mathbf{\Delta}$ will be bounded by a constant $\varepsilon > 0$ [*Shahbazpanahi et al.* (2003), *Vorobyov et al*. (2003)]. The value of ε is determined by the analysis of eigenvalues obtained after the singular value decomposition of the presumed desired-signal covariance matrix and it has to be smaller than the maximum eigenvalue.

The error matrix $\mathbf{\Delta}$ is included in the constraint equation from the MVDR beamformer definition to make it more robust to the mismatch between the presumed and actual signal array responses. In addition, the constraint equation is written such that to maintain a distortionless response to all possible mismatched desired signals instead of one fixed distortionless response (as in Equation 3.12), Therefore, it is required that:

$$\mathbf{w}^{\mathrm{T}} (\mathbf{R_s} + \mathbf{\Delta})\, \mathbf{w} \geq 1 \text{ subject to } \| \mathbf{\Delta} \| \leq \varepsilon. \tag{3.24}$$

According to the assumptions published in *Shahbazpanahi et al.* (2003), the error matrix $\mathbf{\Delta}$ follows as:

$$\mathbf{\Delta} = -\varepsilon \mathbf{I}, \tag{3.25}$$

where $\mathbf{I}$ is the identity matrix. The Robust MVDR beamformer problem from Equation 3.12 can be reformulated as:

$$\min_{\mathbf{w}} \mathbf{w}^T \mathbf{R_d} \mathbf{w} \text{ subject to } \mathbf{w}^T (\mathbf{R_s} - \varepsilon \mathbf{I}) \mathbf{w} = 1 . \tag{3.26}$$

Again, the solution of this problem can be determined using the method of Lagrange multipliers. The optimal weight vector is given by:

$$\mathbf{w}_{opt} = P\{\mathbf{R_d}^{-1}(\mathbf{R_s} - \varepsilon\mathbf{I})\}. \tag{3.27}$$

Equation 3.27 represents the data-adaptive Robust MVDR beamformer weights not affected by the possible mismatches between the presumed and actual desired-signal covariance matrices. In addition, the Robust MVDR beamformer preserve the scale of the desired signal [*Gershman* (1999), *Shahbazpanahi et al.* (2003), *Vorobyov et al.* (2003)].

The design of the Robust MVDR beamformer for areal-array data (3D) is generally the same as for linear-array data (2D). The main difference between these is the size of the input data being a function of the number of receivers. In the 2D case the input data are vectors of size M and for the 3D case MP, where M is the number of inline and P the number of crossline single sensors. Since the size of input vectors is larger, the size of the signal and noise covariance matrices is greater, namely MP × MP. The derivation is exactly the same as for the 2D case, only now the vectors contain areal- instead of linear-array data. The result is then precisely as expressed in Equation 3.27 where the weight vector has now the size MP.

3.3 Robust MVDR beamformer on synthetic single-sensor seismic data

In this section we show the application of the 2D and 3D Robust MVDR beamformer to synthetic data obtained by seismic modeling. This was done using two modeling approaches, one by simply creating a constant-amplitude linear and hyperbolic event, and the other by the finite-difference method. The Robust MVDR results are compared with a standard array response whose weights are fixed and equal to one. The modeling with the linear and hyperbolic event was made in the presence of both phase and amplitude variations, but the first consideration presented omits these.

3.3.1 Robust MVDR on 2D modeled single-sensor seismic data without variations

We first considered a response containing a linear and a hyperbolic event as shown in Figure 3.1. The linear event is characterized by a slow apparent velocity of 440 m/s and a low frequency of 16 Hz representing, for example, a surface wave that is seen as "noise" to be attenuated. The hyperbolic event is characterized by a high apparent velocity of 2000 m/s and a higher frequency of 36 Hz, representing a reflected wave considered to be a desired signal to be protected. The depth of the reflector is 300 m. The wavelet we used is a Ricker wavelet, the second derivative of a Gaussian wave. The first response to consider was 12 traces coming from 12 single sensors spaced 5 m apart.

In seismic practice, an array consists of hard-wired connected receivers so that simulation is achieved by summing the individual recordings as one output. This is the first step in array forming [*Hoffe et al.* (2002)]; the second and final step is spatial resampling to a desired spacing. For the robust MVDR beamformer we used the optimal weights determined from Equation 3.27, the data covariance matrix $\mathbf{R_d}$ based on 12 input traces, and the signal covariance matrix $\mathbf{R_s}$ of the desired signal from 12 input traces containing only the reflected wave. Parameter ε was determined by testing different eigenvalues smaller than the maximum eigenvalue provided by the singular value decomposition of the signal covariance matrix, $\mathbf{R_s}$. Based on the analysis of the errors in amplitude computed using Equation 3.28 for different ε values, for this record a good value for ε is 0.001 (see Figure 3.2). When comparing the results,

one notices that the Robust MVDR beamformer attenuates the surface waves better than standard array forming does, but the desired reflected wave signal is slightly better preserved after standard array forming (see Figure 3.1). In addition, the remaining noise seen on the Robust MVDR beamforming response is characterized by a lower frequency 4–6 Hz response than that seen on the standard array-forming response of about 12 Hz.

The noise attenuation by standard array forming or MVDR beamforming can be quantified by defining an error between the desired response that contains only the reflected wave and the standard array-forming or MVDR beamforming response:

$$e_{tx} = \frac{1}{\mathrm{N_t}} \sum_{n=1}^{N_t} \left| y_n^o - y_n^s \right|, \tag{3.28}$$

where e_{tx} is the error in amplitude computed in the time domain, y^o is the desired response, y^s is the standard array-forming or MVDR beamforming response, and N_t is the total number of time samples. For the example shown in Figure 3.1, the error e_{tx} for the standard array-forming response is $2.39 \cdot 10^{-4}$, and for the MVDR beamforming response it is $2.03 \cdot 10^{-4}$. The smaller error obtained for the MVDR response means that it is closer to the desired-array response. In addition, the fair comparison between all these responses is allowed because the Robust MVDR beamformer preserve the scale of the desired response [*Gershman* (1999), *Shahbazpanahi et al.* (2003), *Vorobyov et al.* (2003), *Jin and Friendlander* (2005)].

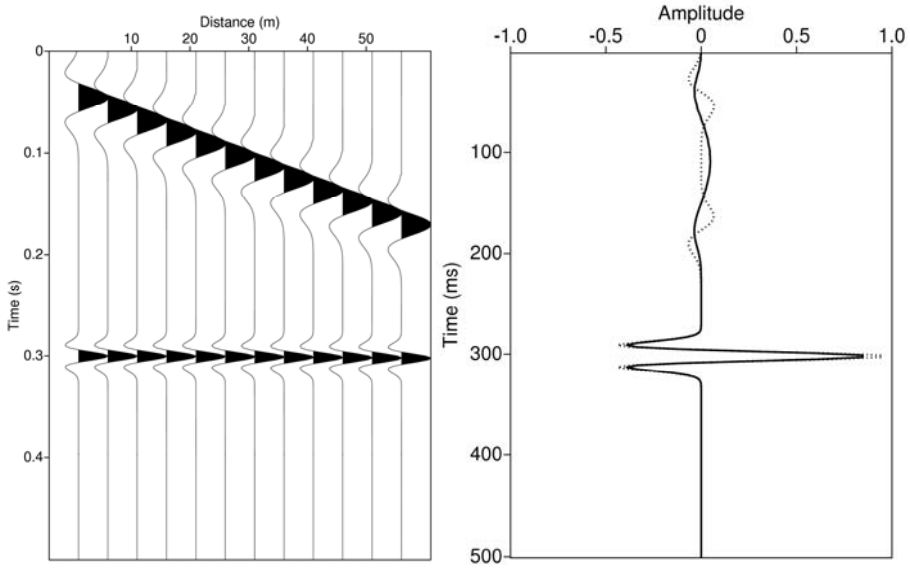

Figure 3.1. Synthetic seismogram with 12 traces (left) after standard array-forming (right, dashed line) and Robust MVDR beamforming (right, solid line)

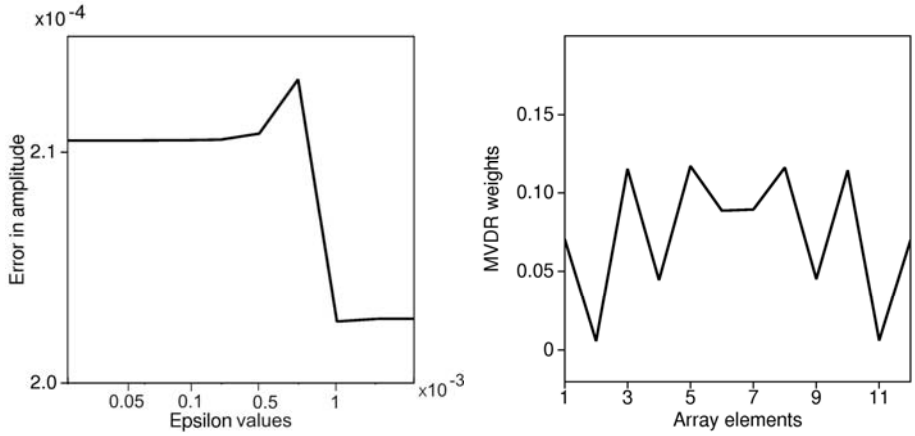

Figure 3.2 Error in amplitude calculated for different epsilon values (left) and the Robust MVDR weights (right) computed for $\varepsilon = 0.001$

To look at spatial characteristics we created a larger set of single-sensor recordings where multiple arrays are formed (see Figure 3.3). The same modeling parameters as before are used for frequencies, velocities, the depth of the reflector, and single-sensor spacing. We used 80 single sensors and applied both the MVDR and the standard array-forming processing in order to compare the attenuation effectiveness of the slow linear event. Since the goal of array forming is to spatially filter and desample the data, the whole surface wave signal does not need to be removed, but only the part that will be outside the new spatial band. As we will show later, there are situations when standard array forming does not adequately attenuate out-of-the-new-spatial-band energy, which means that part of the surface waves will be spatially aliased after resampling to a larger group interval. Attenuation is better achieved using the Robust MVDR adaptive beamformer. We applied the Robust MVDR beamforming to this record in order to attenuate the out-of-the-new-spatial-band surface waves. This algorithm was applied to an array of 12 elements. The computation of the data and signal covariance matrices was done for a sliding window of 12 traces as 1–12, 2–13, 3–14, etc. The traces used for the computation of the signal covariance matrix were chosen from the globally k-filtered single-sensor record that contains only the new-spatial-band energy determined for the desired group interval of 10 m. Furthermore, based on the singular value decomposition of the signal covariance matrix, we obtained a set of eigenvalues (see Figure 3.4, up-left).

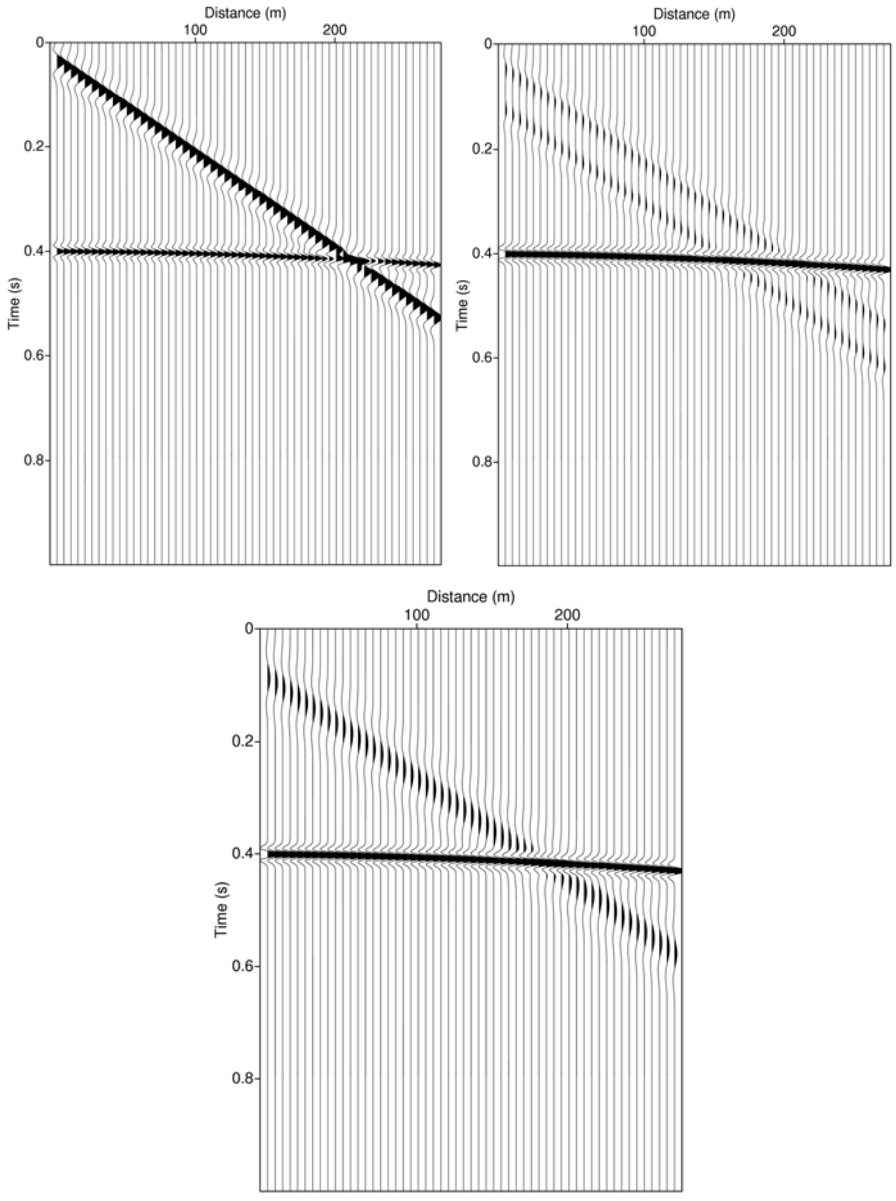

Figure 3.3. Synthetic seismogram (up, left) after standard array-forming (up, right) and Robust MVDR beamforming (down), displayed in the time domain

After the analysis of the errors in amplitude computed for different ε values, the value of 0.0005 was chosen as optimal (see Figure 3.4, up, right); the ε value is smaller than the maximum eigenvalue obtained for each group of elementary recordings. The error in amplitude is computed for the interval between the new and the old Nyquist wavenumbers:

$$e_{fk} = \frac{1}{N_f}\frac{1}{N_k}\left(\sum_{f=1}^{N_f}\sum_{k=-N_{k\_old}}^{-N_{k\_new}}\left|\tilde{y}_{f,k}^{s} - \tilde{y}_{f,k}^{o}\right| + \sum_{f=1}^{N_f}\sum_{k=+N_{k\_new}}^{+N_{k\_old}}\left|\tilde{y}_{f,k}^{s} - \tilde{y}_{f,k}^{o}\right|\right), \quad (3.29)$$

where e_{fk} is the error, $\tilde{y}^o$ is the (f, k_x)-domain amplitude spectrum of the desired response, which should be zero on these two wavenumber intervals, $\tilde{y}^s$ is the (f, k_x)-domain amplitude spectrum of the standard array-forming or MVDR beamforming response, N_k is the wavenumber sample quantity, and N_f is the number of frequency samples. The desired response is considered to be a record of all energy above the new Nyquist wavenumber zero. Then, for this ε value we computed the MVDR beamformer weights (see Figure 3.4, down).

The response of a standard array was also computed (see Figure 3.3, center). We display only the output of the first step of array forming, namely the adding of traces; the second step is represented by spatial resampling to a group interval that will not spatially alias the reflected waves. The first step is more important than the subsequent spatial resampling because it gives us a spatially broadband picture of the noise attenuation.

By comparing the responses of these two algorithms, we see that the Robust MVDR beamforming achieved better out-of-the-new-spatial-band attenuation than standard array forming. The remaining noise seen on the Robust MVDR beamforming response is characterized by a very low frequency of about 4–6 Hz compared to the original of 16 Hz. In contrast, the standard

array-forming response shows us two clear linear events with the same slowness as the original one but arriving with only slightly lower frequencies than initially, at about 12 Hz. The (f, k_x)-domain amplitude spectrum of the initial record before array forming is shown in Figure 3.5. It can be observed that neither arrival is affected by spatial aliasing because we have not yet desampled.

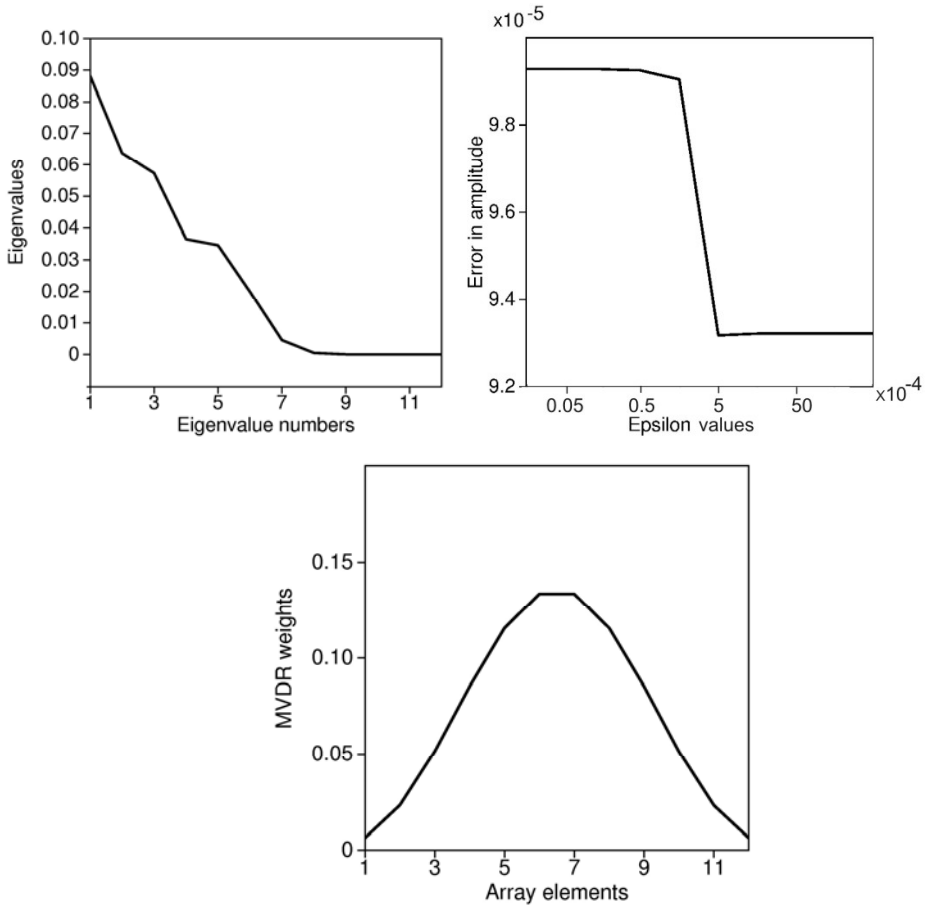

Figure 3.4. Eigenvalues (up-left), errors in amplitude for different ε values (up-right) and the Robust MVDR beamformer weights (down) determined for ε = 0.0005

We also notice that if we spatially resample both responses to a group interval of 10 m giving a Nyquist wavenumber of 0.05 m^{-1}, the remaining surface wave on the standard-array response would be more spatially aliased compared with the Robust MVDR beamforming response. In addition, if we compare the standard-array and MVDR beamformer responses with that of filtering over the wavenumber interval (- 0.05, 0.05), we notice a better attenuation of the surface waves on the first two responses (see Figure 3.5).

The attenuation of the slow linear events can be quantified by defining the difference between the out-of-the-new-spatial-band energy in the (f, k_x)-domain of the desired response and of the standard array-forming or MVDR beamforming response. A value of 0.0056 was obtained for e_{fk} in the case of standard array forming and 0.0050 for MVDR beamforming. Based on these values we obtained better noise attenuation with MVDR beamforming. If the spatial resampling were adjusted to 10 m, the remaining noise contained by the standard-array response would be more spatially aliased (see Figure 3.5).

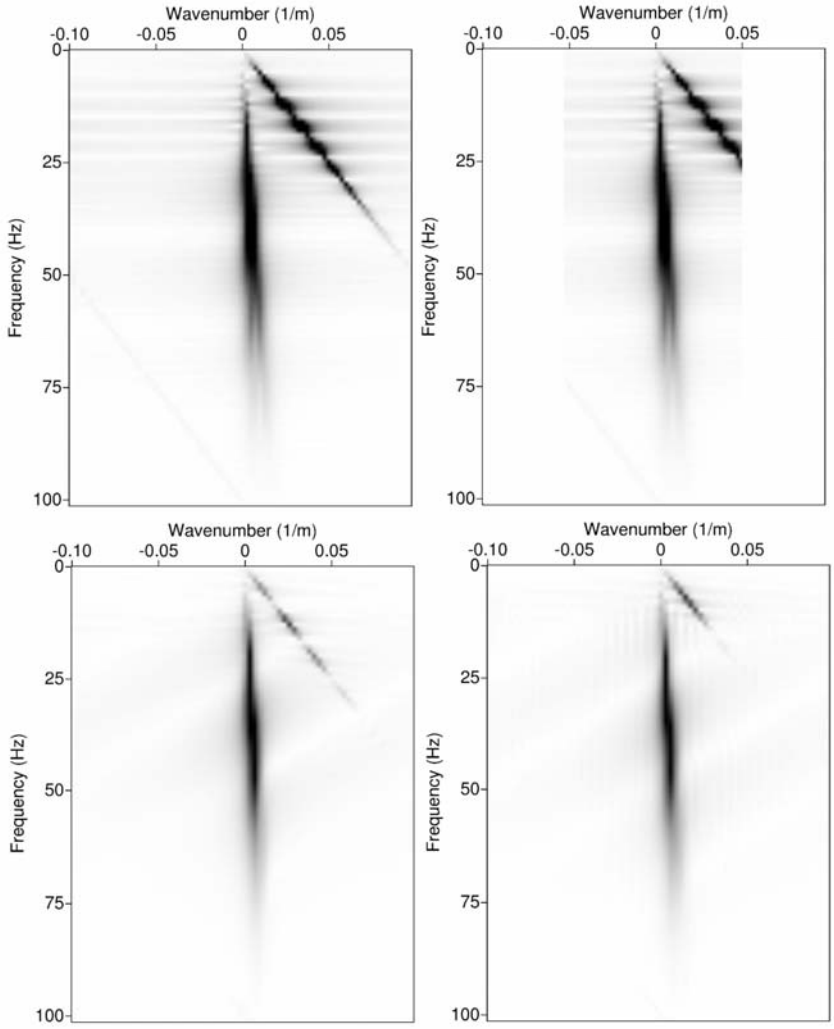

Figure 3.5. (f, k_x)-amplitude spectrum of a synthetic seismogram (up, left) after k-filtering (up, right), standard array-forming (down, left) and Robust MVDR beamforming (down, right); same display parameters are taken

3.3.2 Robust MVDR on 2D modeled single-sensor seismic data with variations

The synthetic seismogram analysed above was modeled without phase or amplitude variations. The modeling parameters were chosen in order to avoid the strong spatial aliasing for both events. Since field seismic records are usually affected by phase and amplitude variation, it is necessary to consider their effect on the Robust MVDR beamforming response. Phase variations can occur because of irregular receiver positioning, variable intra-array static effects, and a large lateral variation of velocity inside the receiver array. Amplitude variations can occur, for example, due to imperfection of the geophone ground coupling.

We considered phase variation in modeling the synthetic record. Timing errors were introduced by mispositioning all of the receivers. We again used the linear and hyperbolic event using 80 irregularly spaced single sensors. A maximum variation of 20% within the receiver spacing of 5 m apart was allowed. The seismogram is displayed in Figure 3.6 and its (f, k_x)-domain amplitude spectrum is shown in Figure 3.7. The effect of the phase variation is clear on both the (t, x)- and the (f, k_x)-domain panels. The variation generated some aliased energy seen on the (f, k_x)-domain amplitude spectrum, observable as inclined stripes.

We next applied standard array and Robust MVDR beamforming for a 12 elements array. Again, the computation of the data and signal covariance matrices was done for a sliding window of 12 traces as 1–12, 2–13, 3–14, etc. The traces involved in the $\mathbf{R_s}$ computation have been chosen from a globally k-filtered record that contains only the new-spatial-band energy determined for the desired group interval of 10 m. In case of the Robust MVDR beamformer, the weights are computed for $\varepsilon = 0.0004$. The results are shown in Figures 3.6

and 3.7. In observing the responses for the (t, x)-domain, we noticed good noise attenuation for the standard array-forming response but greater attenuation to the Robust MVDR beamforming result.

The undesired striping energy of the (f, k_x)-domain is well attenuated by both standard array forming and MVDR beamforming (see Figure 3.7).

The good results obtained by Robust MVDR beamforming are supported by the quantification of the error e_{fk}, determined by Equation 3.29 as equal to 0.0052 for the MVDR beamforming response. For the standard array this error is 0.0055.

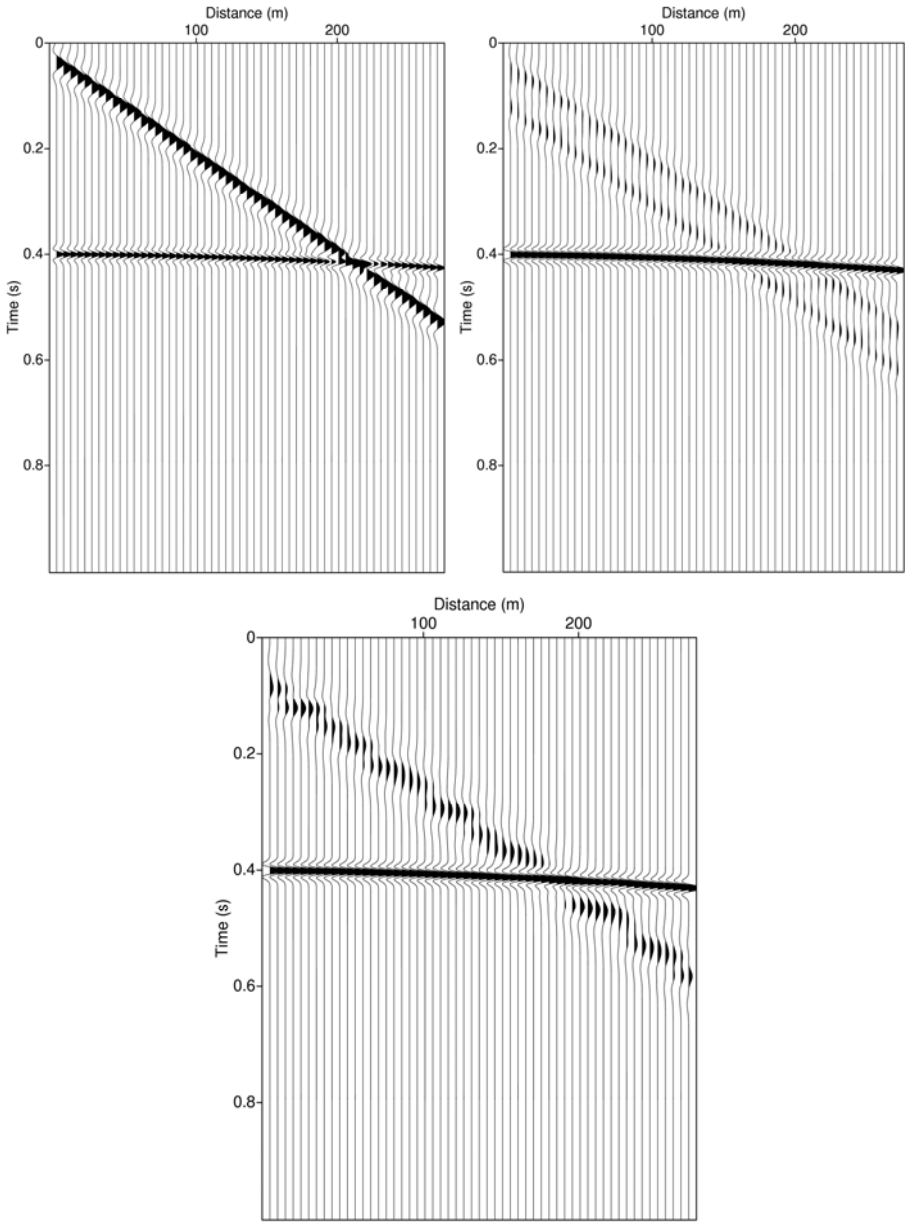

Figure 3.6. Synthetic seismogram with irregular single-sensor spacing, maximum error 20% of 5 m, (up, left) after standard array-forming (up, right) and Robust MVDR beamforming (down)

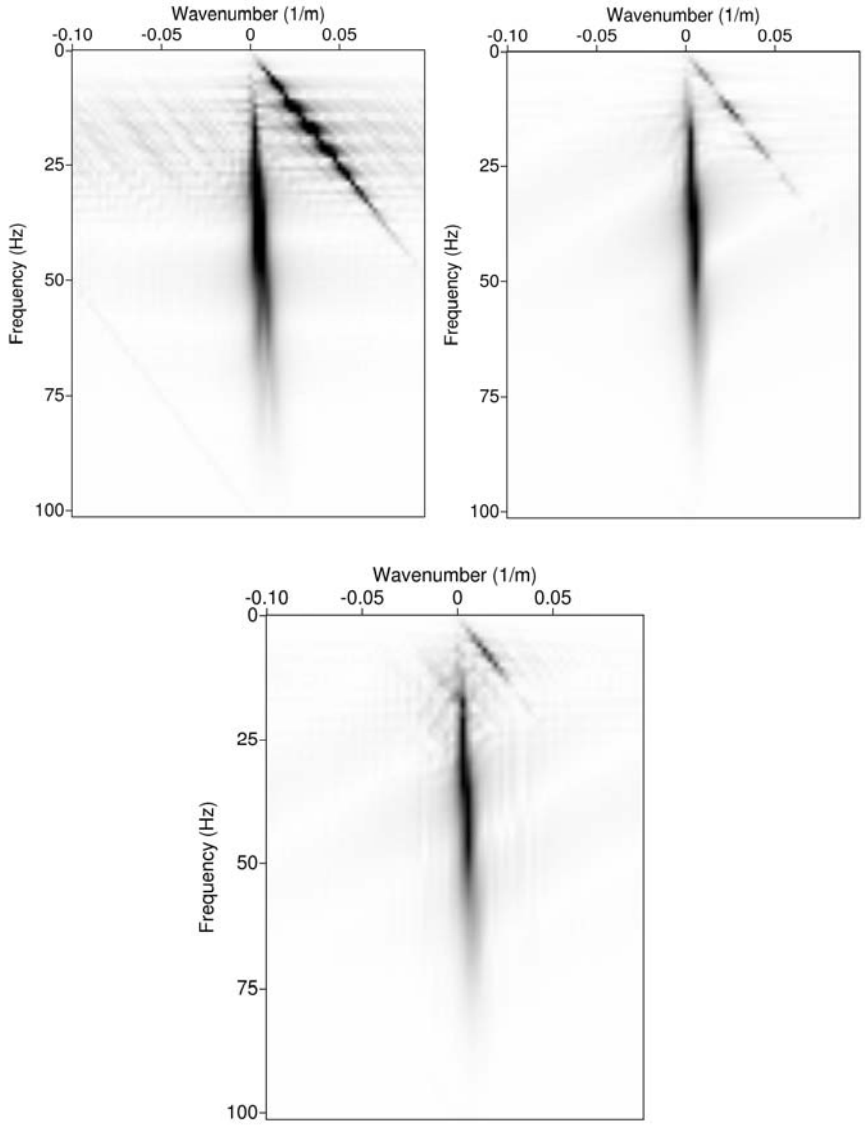

Figure 3.7. (f, k_x)-amplitude spectrum of synthetic seismogram with irregular single-sensor spacing, maximum error 20% of 5 m, (up, left) after standard array-forming (up, right) and Robust MVDR beamforming (down)

The effect of amplitude variation was analyzed working with synthetic records and we noticed that the effect is less than that compared to those with phase variation (see Figures 3.8); the effect of the amplitude variations is clear on the (f, k_x)-domain (see Figure 3.9). The aliased energy generated by this type of variation is well attenuated by the Robust MVDR beamformer, whose weights were computed for $\varepsilon = 0.0001$.

Also, the Robust MVDR beamformer works well in the presence of groups of noisy traces (see Figure 3.10). Same array parameters have been used in order to compute the standard array and MVDR beamformer responses (see Figure 3.10). The optimal weights were computed for $\varepsilon = 0.001$. The quantification of the error e_{fk}, was done using Equation 3.29 being equal to $76 \cdot 10^{-8}$ for the MVDR beamforming response. For the standard array this error is $278 \cdot 10^{-8}$. Therefore, the Robust MVDR beamformer works better than standard array.

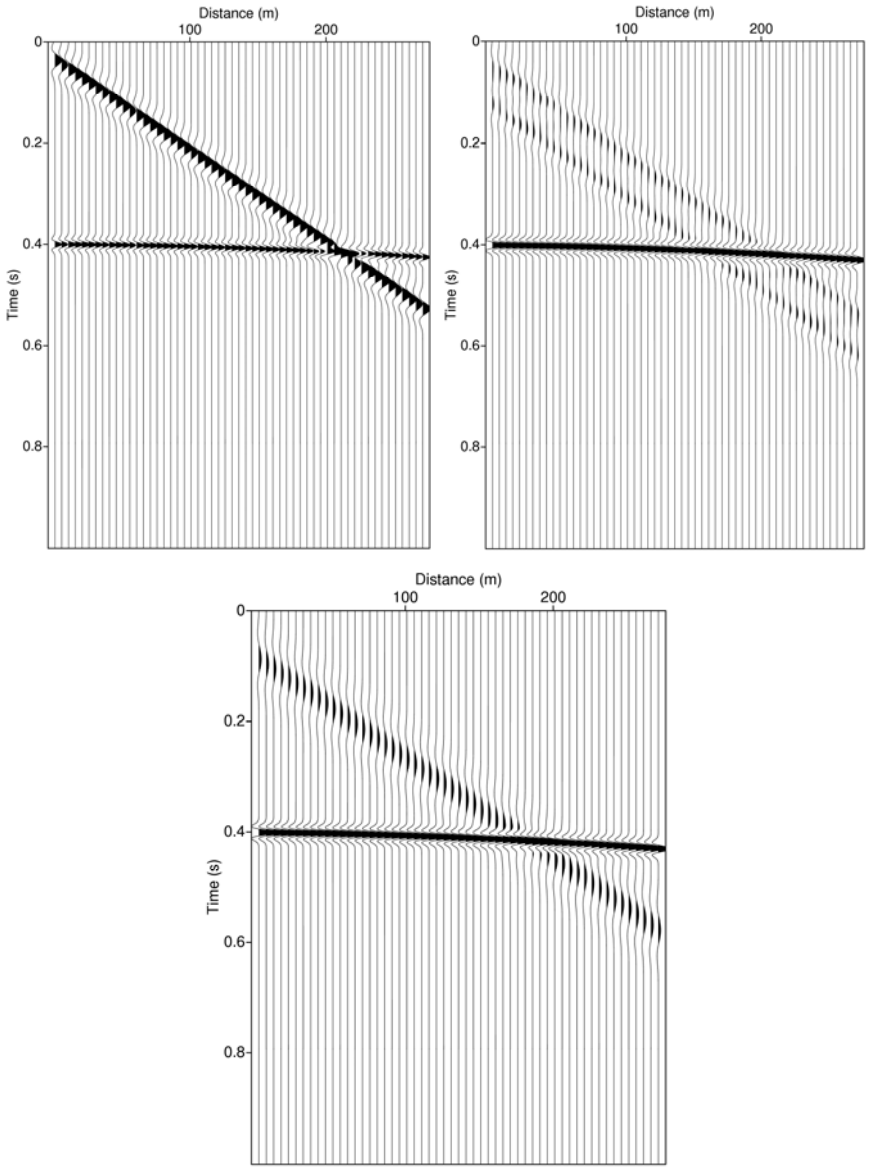

Figure 3.8. Synthetic seismogram with amplitude variation, maximum error 20%, (up, left) after standard array-forming (up, right) and Robust MVDR beamforming (down)

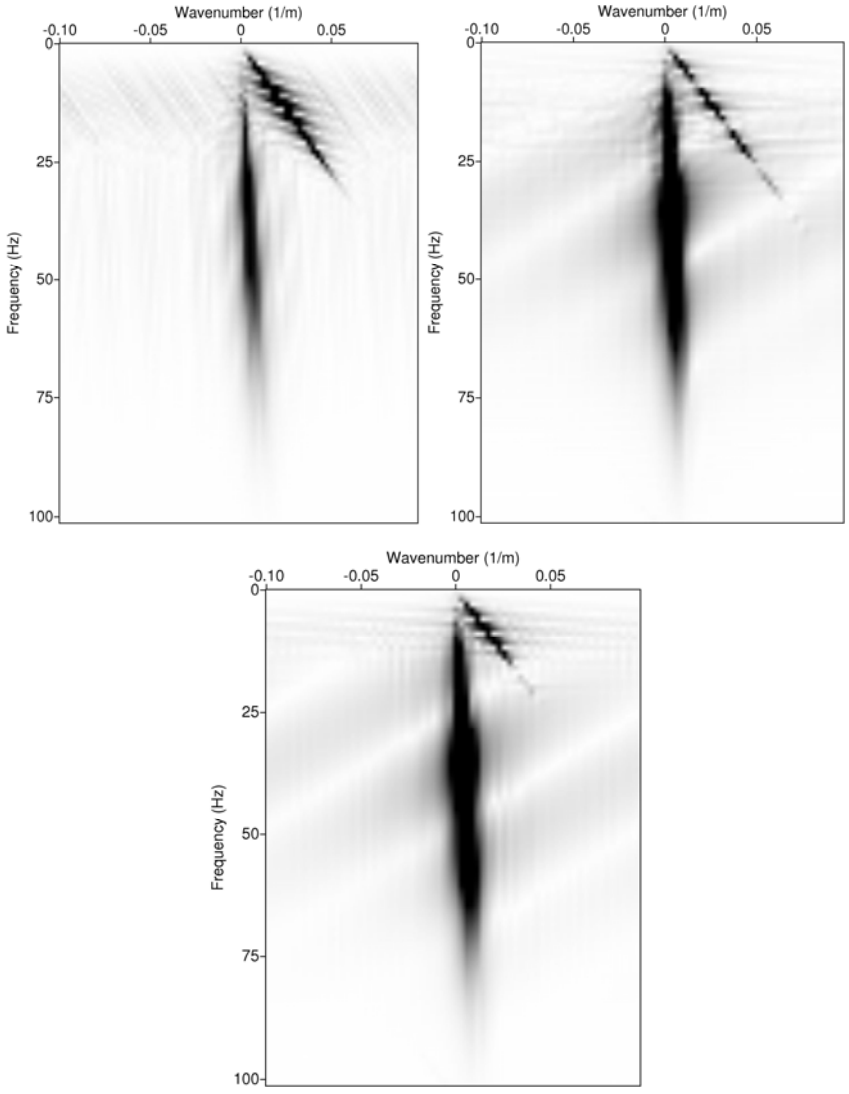

Figure 3.9. (f, k_x)-amplitude spectrum of synthetic seismogram with amplitude variation, maximum error 20%, (up, left) after standard array-forming (up, right) and Robust MVDR beamforming (down)

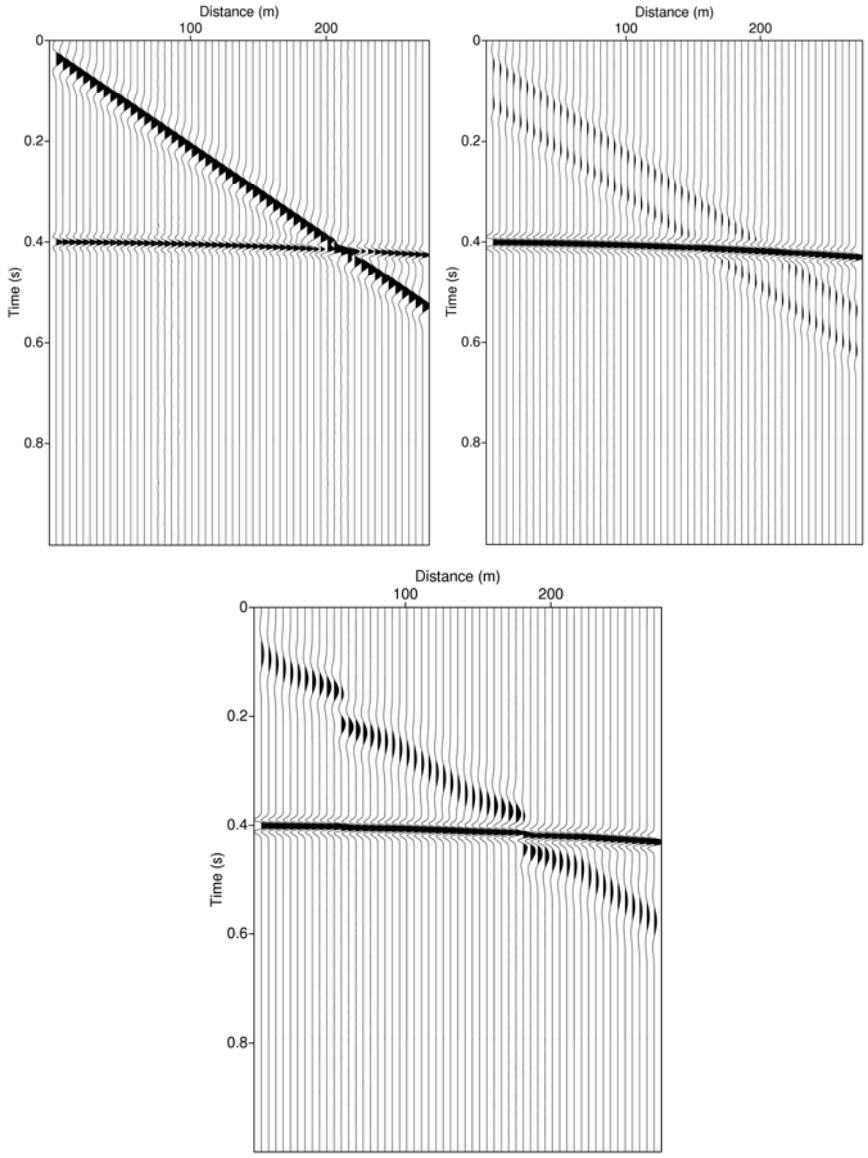

Figure 3.10. Synthetic seismogram with noisy traces (left) after standard array-forming (center) and Robust MVDR beamforming (right)

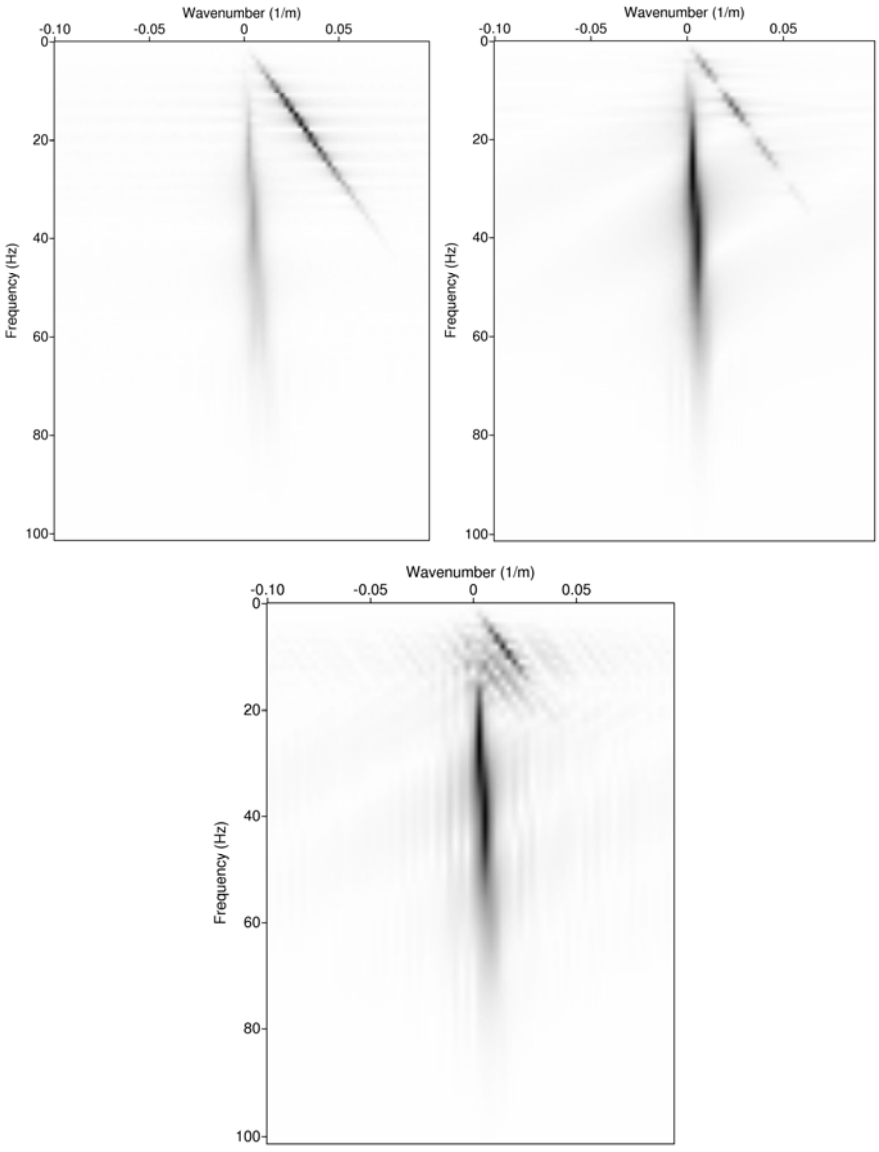

Figure 3.11. (f, k_x)-amplitude spectrum of synthetic seismogram with noisy traces (left) after standard array-forming (center) and Robust MVDR beamforming (right)

3.3.3 Robust MVDR on 2D finite-difference modeled single-sensor seismic data

We have so far shown the better performance of Robust MVDR compared to standard array forming when considering the simple response of a linear and hyperbolic event. To increase the complexity of the records but still have some control over the outcome we then created synthetic records using the finite-difference method based on the elastic wave equation. The 2D depth model has four horizontal layers with the density and P- and S-wave velocities varying with depth. These parameters are constant along the profile (Figure 3.12). A model shot record is displayed as Figure 3.13. Reflected waves are covered by dispersive surface waves at small offsets, and head waves are abundant at large offsets. Head waves are not well attenuated by array forming because of their high apparent velocity and frequency, which are comparable with reflections.

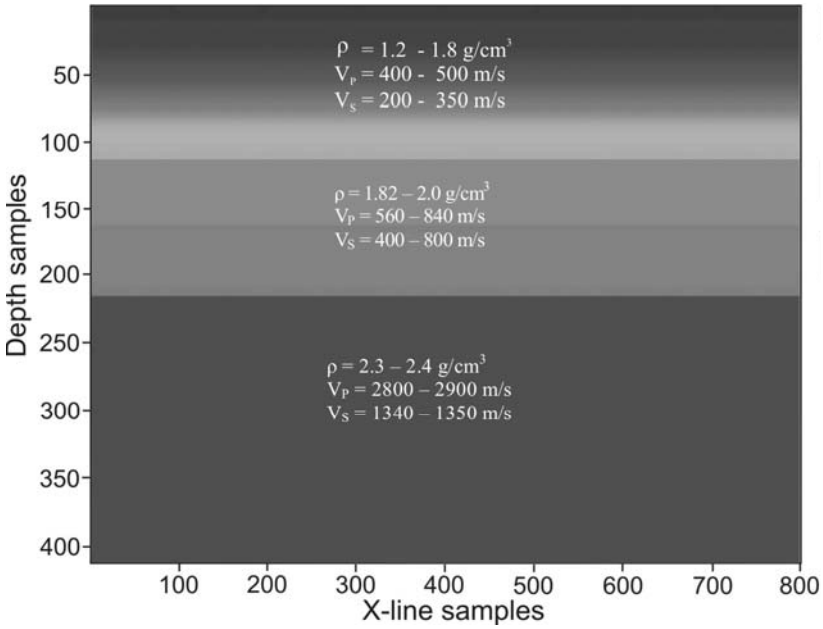

Figure 3.12. Depth model used for elastic finite-difference modeling

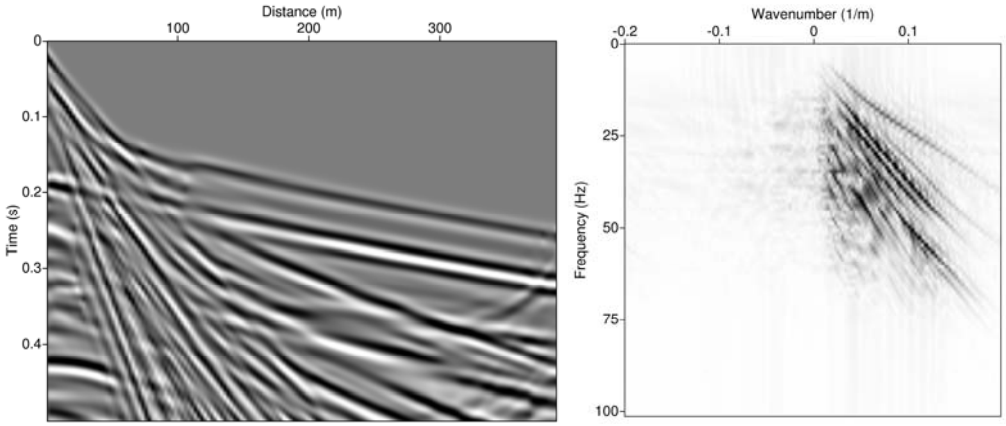

Figure 3.13. Synthetic seismogram (left) and its (f, k_x)-amplitude spectrum (right). Modeling parameters: 160 single sensors with 2.5 meters spacing, time sampling interval is 1 ms

To prevent spatial aliasing of the reflected waves, an array of 12 elements, meaning an array length of 30 m, was used in this case. For the chosen array length, the standard array-forming response did not show good noise attenuation. We therefore expected that the Robust MVDR beamformer would show better out-of-the-new-spatial-band surface wave attenuation. For an accurate comparison we used the same 30 m array length. The application of this algorithm required the knowledge of the data covariance matrix $\mathbf{R_d}$ and the signal covariance matrix $\mathbf{R_s}$. For $\mathbf{R_d}$ a group of raw 12 traces was used, so $\mathbf{R_d}$ is always a local covariance. For the signal covariance a full record was used and for this the out-of-the-new-spatial-band energy was zeroed. These k-filtered data were then used for the matrix $\mathbf{R_s}$ for all groups of 12 elementary recordings 1–12, 2–13, 3–14, and so forth, given by individual sensors. In this way the *globally* filtered record was used for the computation of all the *local* beamformers in that record. It is important to note here that the presumed and actual desired-signal responses were different but the MVDR discussed in the design section takes account of this. The matrix $\mathbf{R_s}$ was used for the computation of parameter ε, via singular-value decomposition. The optimal beamformer weights were computed for a value of ε smaller than the maximum eigenvalues obtained after singular value decomposition; in our case, this value was 0.0001. Then, the optimal weights were computed for each group of single-sensor recordings. In Figure 3.14 we display two groups of 12 single-sensor recordings, chosen from the record displayed in Figure 3.13, that were involved in the standard-array and MVDR beamformer responses computation. The first one contains the traces from the distance interval 10 – 37.5 m; here, the reflections are clear (see Figure 3.14, left). The second one contains the traces from the distance interval 40 – 67.5 m where the noise is dominant (see Figure 3.14, right). Using these two records as input, we obtain the data covariance matrices, $\mathbf{R_d}$. The same windows of traces were chosen from the globally

filtered record in order to compute the matrix $\mathbf{R_s}$. This matrix is necessary to compute the eigenvalues required by the MVDR beamformer weights computation.

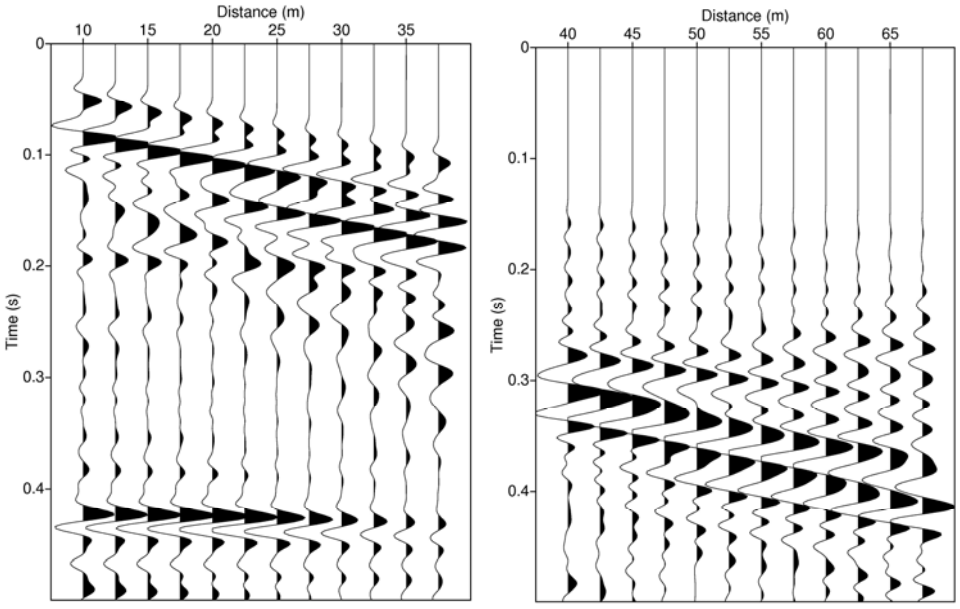

Figure 3.14. Group of traces located between 10 – 37.5 m (left) and 40 – 67.5 m (right), chosen from synthetic record displayed in Figure 3.13

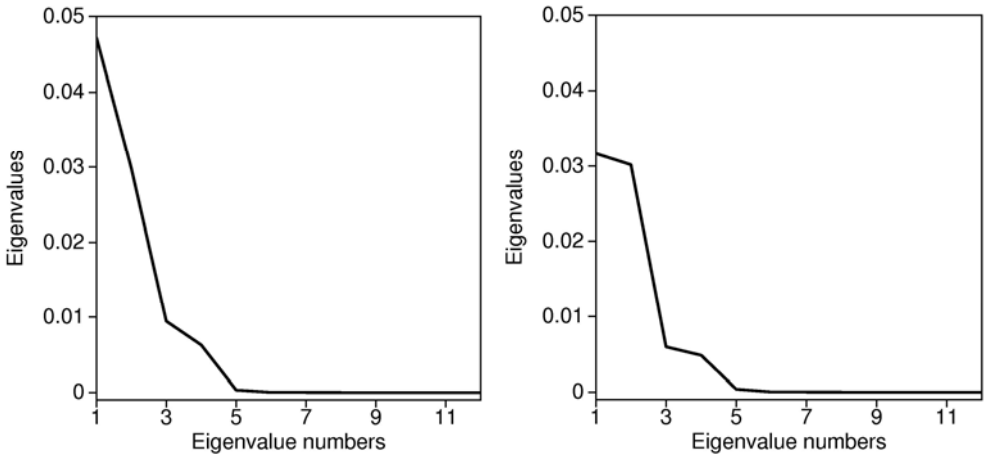

Figure 3.15. Eigenvalues for the group of traces located between 10 – 37.5 m (left) and 40 – 67.5 m (right)

We display in Figure 3.15 the eigenvalues determined for the group of traces placed at small (left) and large (right) distances from the shot-point. Based on the analysis of these sets of eigenvalues, the ε value chosen as optimal was 0.0001. Next, the MVDR beamformer weights were calculated and applied to these group of traces before their summation. If we compare the weights obtained for these two groups of 12 traces records we notice that they are almost constant along the array, in cases where the desired signal is dominant, or show a significant variation, in cases where the noise is dominant (see Figure 3.16).

Looking at the Robust MVDR beamforming response displayed in Figure 3.17a, we note appreciable attenuation of the out-of-the-new-spatial-band surface waves with clear reflected waves at larger offsets than in the initial record (see Figure 3.13).

As expected, the refracted waves are still high in amplitude but the same result is seen for the standard array-forming response. Significantly, the out-of-

the-new-spatial-band surface waves are not greatly attenuated after standard array forming (see Figure 3.17a). Furthermore, when considering the (f, k_x)-domain representation as shown in Figure 3.17b, the Robust MVDR result appears more positive.

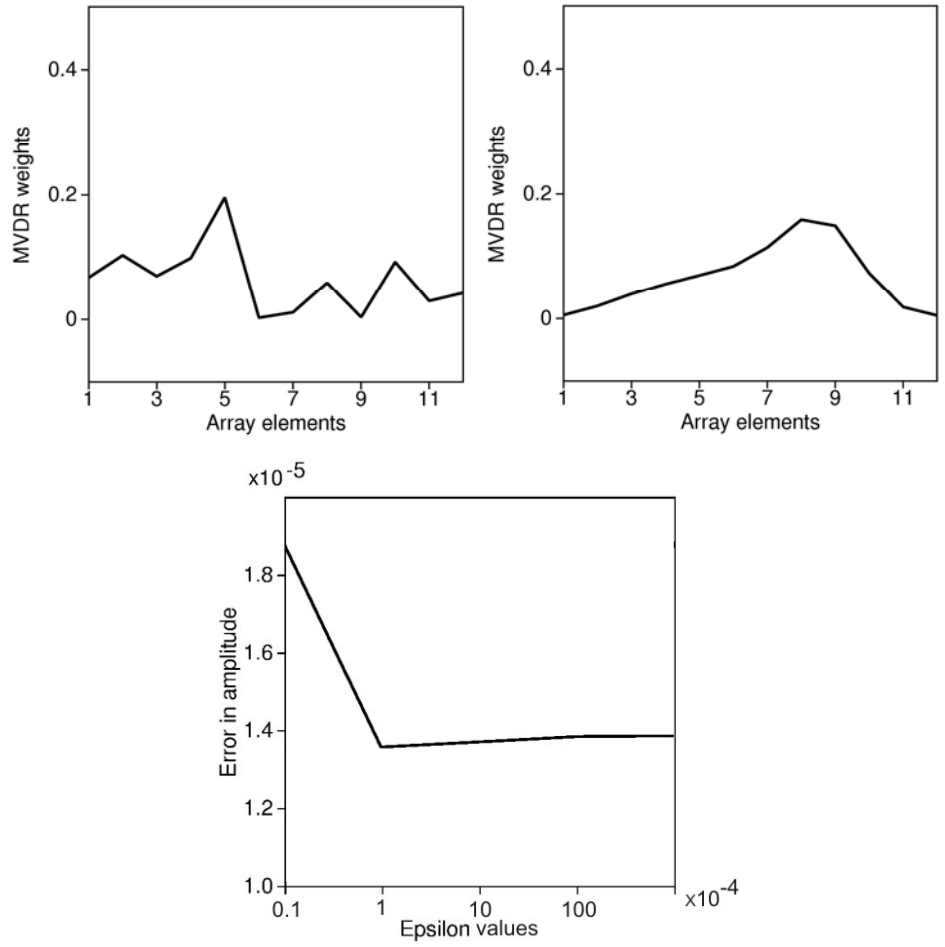

Figure 3.16. Robust MVDR beamformer weights for the group of traces located between 10 – 37.5 m (up, left) and 40 – 67.5 m (up, right) and the error in amplitude for different ε values (down)

If we attempted the second step of spatial resampling, for example to a group interval of 10 m, meaning a Nyquist wavenumber of 0.05 m^{-1}, the remaining surface waves would be spatially aliased in the standard-array case, much less so for MVDR (see Figure 3.17b).

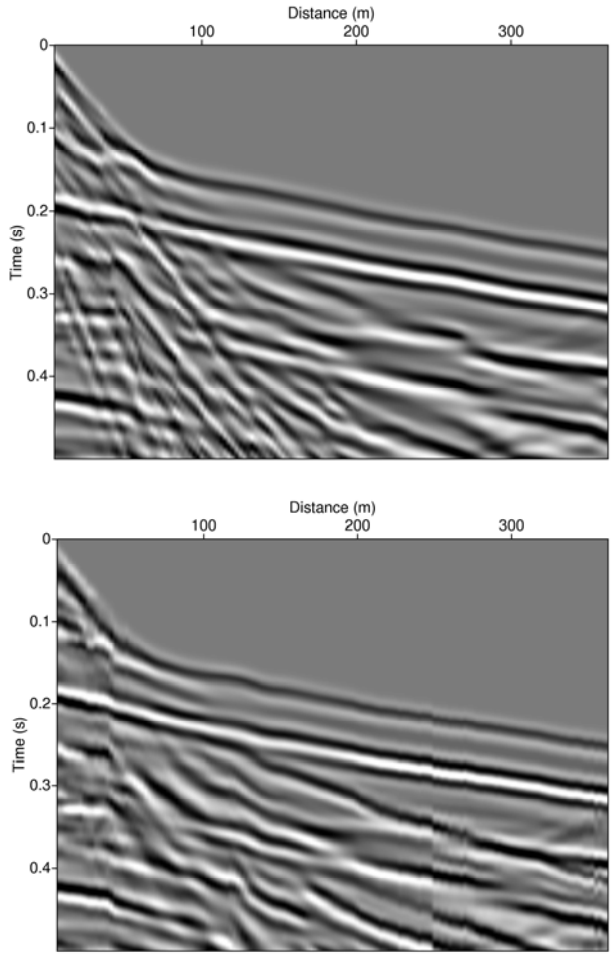

Figure 3.17a. Synthetic seismogram after standard array-forming (left) and Robust MVDR beamforming (right) displayed in the time domain

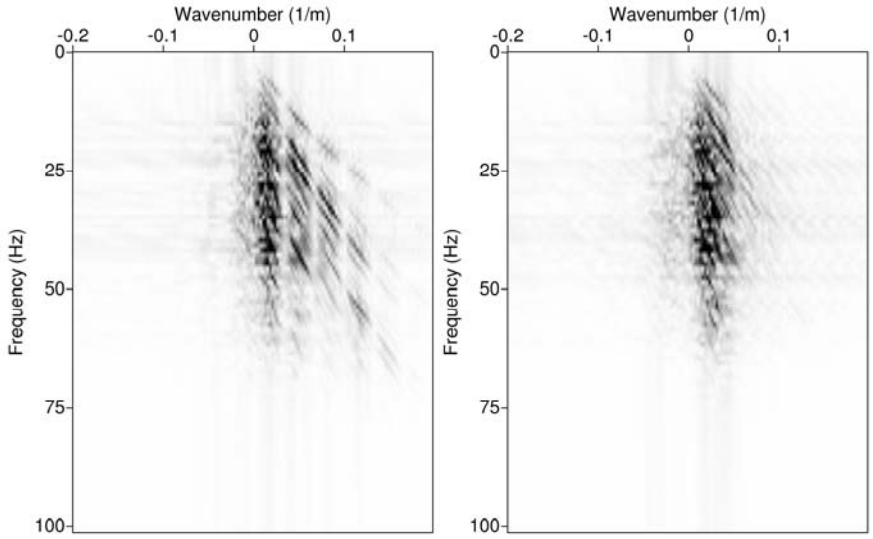

Figure 3.17b. (f, k_x)-amplitude spectrum of synthetic seismogram after standard array-forming (left) and Robust MVDR beamforming (right); same display parameters are taken.

Since the (f, k_x)-domain amplitude spectrum of the Robust MVDR beamformer shows better out-of-the-new-spatial-band attenuation, its spatial resampling would give a record with surface waves scarcely spatially aliased.

As a quantification of noise attenuation efficacy by the Robust MVDR beamformer, error e_{fk} based on Equation 3.29 is 0.0048 for the standard-array response and 0.0030 for the MVDR beamforming response, so the MVDR result is better.

3.3.4 Robust MVDR on 3D finite-difference modeled single-sensor seismic data

In the previous account we analyzed the effect of the Robust MVDR beamformer on 2D synthetic seismic data. We noticed that the surface waves were well attenuated, even in the presence of phase and amplitude variation. Considering that we wish to analyze a partial-3D field data set we must look at the effect of the 3D MVDR beamformer on 3D synthetic data. We modeled a synthetic data set using the elastic finite difference code. The 3D depth model used is an extension of the 2D model shown in Figure 3.12.

The synthetic record was modeled using a strip of five lines of single sensors spaced at 5 m in the inline and crossline directions (see Figure 3.18); the source was located on the third line. The array with 6 inline and 5 crossline elements was chosen to prevent the spatial aliasing of the arrivals contained by the modeled record. The group interval was 10 m and the beamformer weights were computed with a value of $\varepsilon = 0.001$. The desired signal is a record showing zero out-of-the-new-spatial-band energy; consequently, we filtered all the traces in the *global* record. The covariance matrix of the desired signal involved in the weight definition is then the presumed signal covariance matrix. The actual signal covariance matrix of the *local* array was slightly different but our Robust MVDR takes account of this. The data covariance matrix was computed using the synthetic record that contains desired signal and noise; to this end we only used the raw traces that belong to the local array.

Looking at the Robust MVDR beamforming response displayed in the (t, x)- and (f, k_x)-domains in Figures 3.19a and 3.19b, we notice a greater out-of-the-new-spatial-band energy attenuation for the MVDR compared to the result for standard array forming.

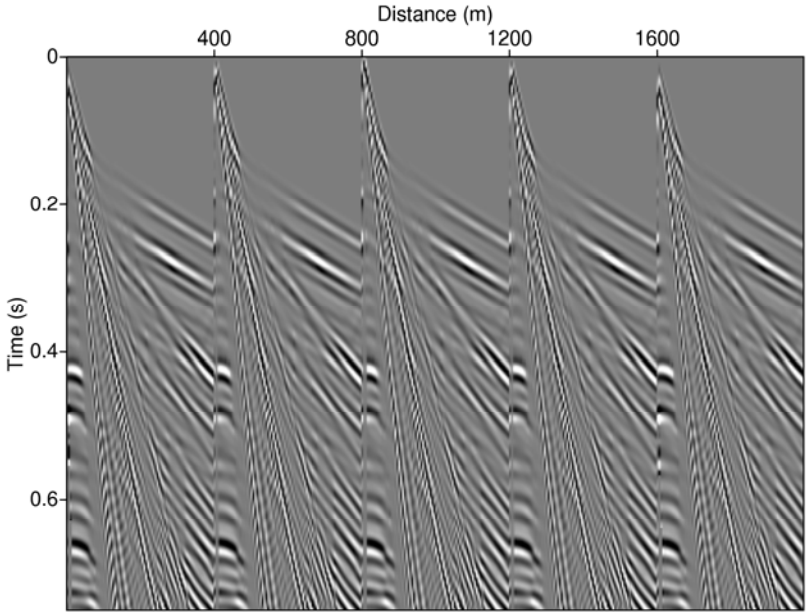

Figure 3.18. Synthetic record with 5 seismograms for 80 single-sensors with 5 meters spacing (inline direction). Depth model parameters as defined in Figure 3.12.

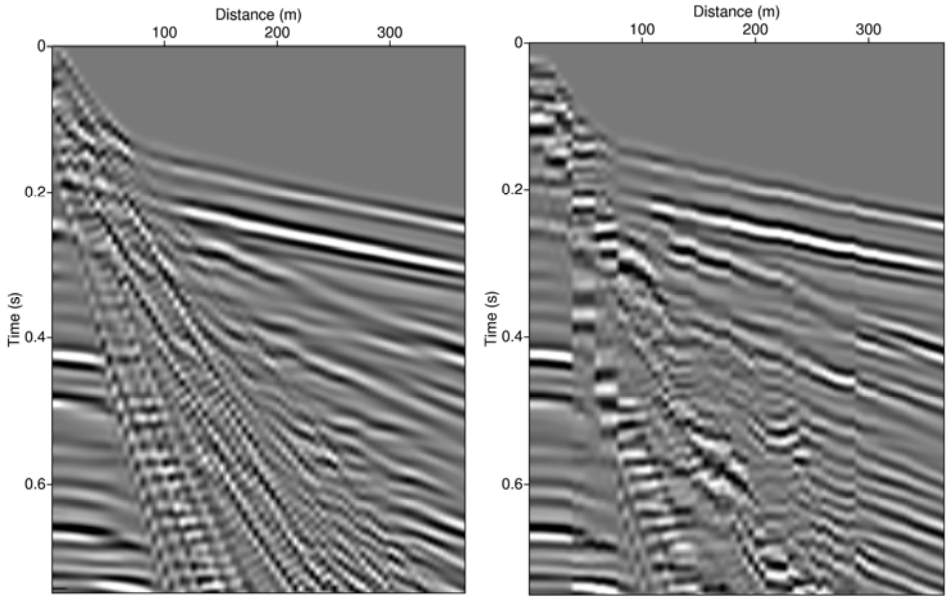

Figure 3.19a. Standard array-forming (left) and Robust MVDR beamforming (right) responses for arrays with 6 × 5 elements for finite-difference modeled data. Depth model parameters as defined in Figure 3.12.

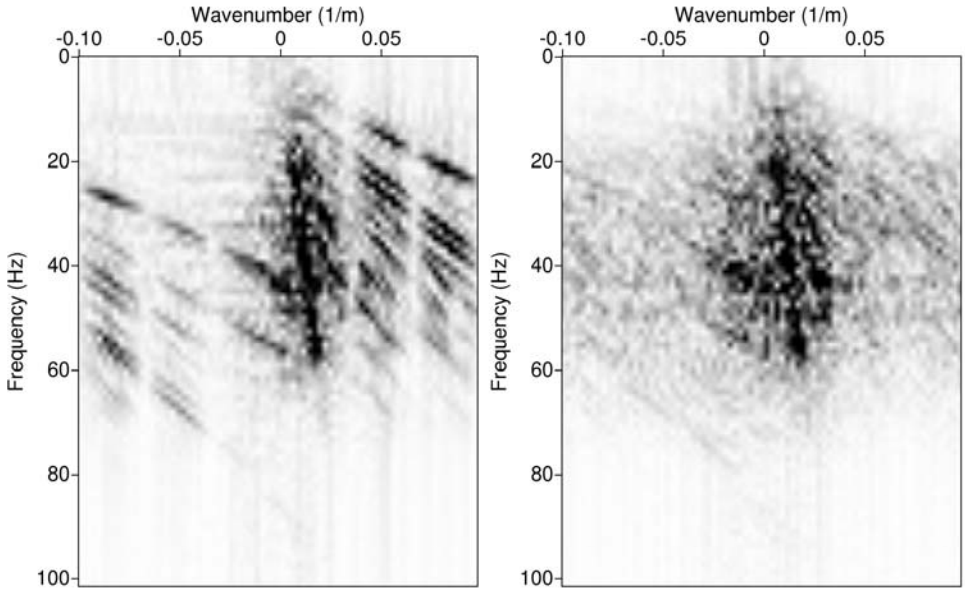

Figure 3.19b. (f, k_x)-amplitude spectrum of standard array-forming (left) and Robust MVDR beamforming (right) responses for arrays with 6 × 5 elements for finite-difference modeled data. Depth model parameters as defined in Figure 3.12.

The remaining surface waves are clear on the standard array-forming response displayed in the (t, x)- and (f, k_x)-domains (see Figures 3.19a and 3.19b).

The same procedure as for the 2D case was followed here in order to quantify the noise attenuation performed by the 3D MVDR beamformer. A value of 0.0149 was obtained for error e_{fk} with the 3D MVDR beamformer, which is much less than 0.0630 obtained for the standard array. This indicates that the MVDR beamformer gives a result much closer to the desired array response compared with standard array forming.

3.4 Robust MVDR beamformer on single-sensor field data

In this section we consider the 2D and 3D MVDR beamformer used on single-sensor field data. These data were recorded using a strip of five lines of single sensors spaced at 5 m in the inline and crossline direction. The seismic energy was generated with dynamite, the source spacing as 20 m, and the source locations were only on the central line of the single sensors. One purpose of the project whose records are used in this section was to apply the MVDR technique and compare it with standard array forming. In this particular case the field data were affected by variation in the amplitude and phase because data acquisition took place in a hilly area with a notable elevation difference along one receiver array (see Figure 3.20). In addition, lateral velocity variation is known in this area, especially in the shallower layers. Amplitude variation occurred because of soil conditions that locally did not provide good soil-geophone coupling.

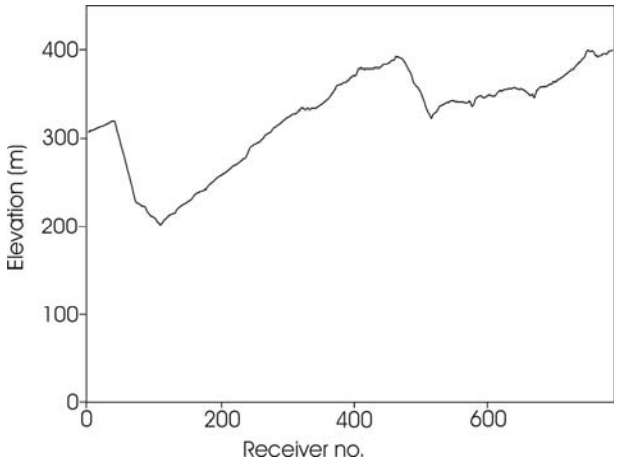

Figure 3.20. Elevation variations along the seismic profile of field data.

3.4.1 Robust MVDR on 2D single-sensor field data

We first applied the beamformer to a one shot record (see Figure 3.21a). Looking at the two time responses, we notice that the remaining surface waves are easier to identify on the standard array-forming response than on the Robust MVDR beamforming response (see Figure 3.21a). We used an array with 12 elements. If we compare the standard array-forming with the MVDR beamforming response in the (f, k_x)-domain as depicted in Figure 3.21b, we notice clear aliased energy to be concentrated around a wavenumber of 0.05 m^{-1} and a frequency of 10 Hz on the standard array-forming response. Conversely, this aliased energy is seen to be more attenuated after MVDR beamforming (see Figure 3.21b). The parameter ε required for the computation of the MVDR weights was determined using the singular-value decomposition of the signal covariance matrix, $\mathbf{R}_s$; this matrix was again computed using a filtered version of the analyzed record over the interval ($-k_{N,new}$, $+k_{N,new}$) obtained for the 10 m group interval. The second matrix involved in the weight computation is the data covariance matrix, $\mathbf{R}_x$, and it was computed based on the raw single-sensor records. The best out-of-the-new-spatial-band energy attenuation obtained was for ε = 0.02. To quantify the effectiveness of noise attenuation performed by the 2D Robust MVDR beamformer using Equation 3.29, we noted e_{fk} = 0.0088 for the MVDR beamforming response and the higher value of e_{fk} = 0.0118 for the standard-array response.

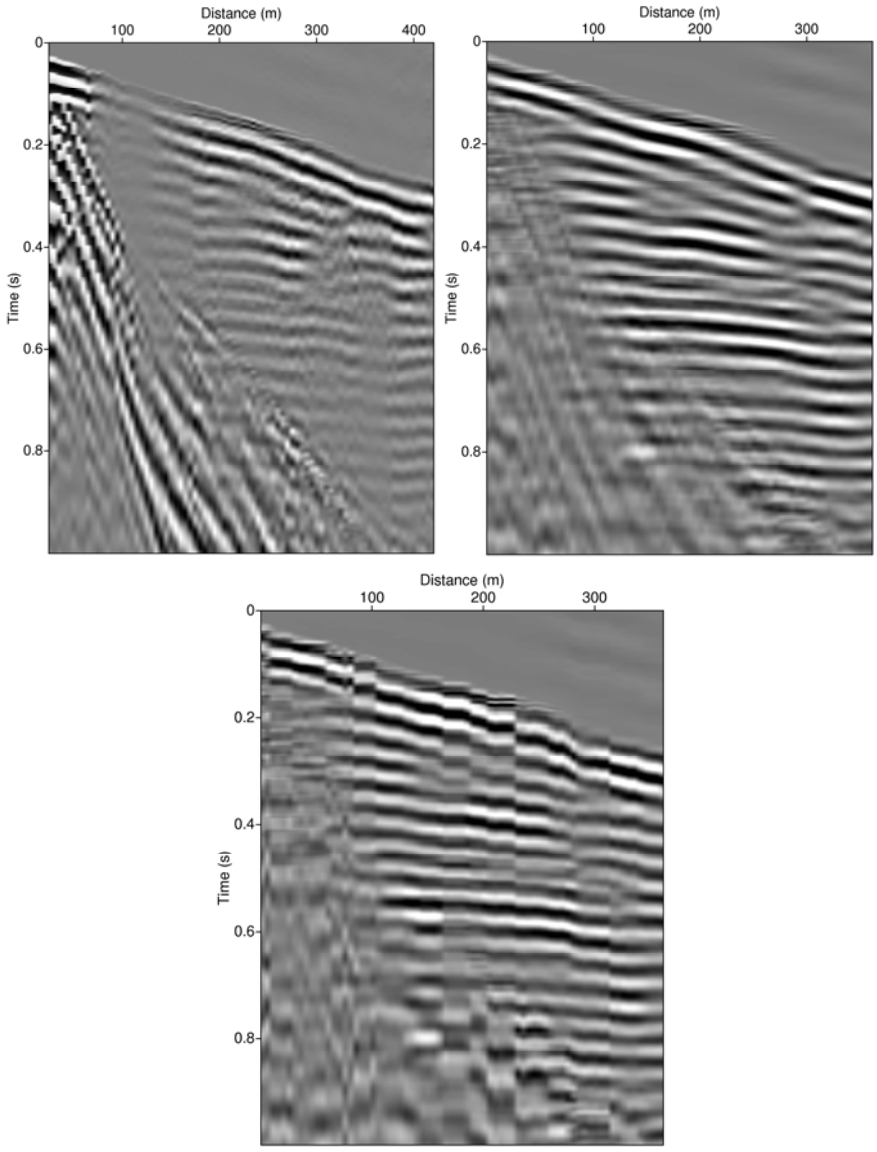

Figure 3.21a. Field record (left) after standard array-forming (center) and Robust MVDR beamforming (right) displayed in the time domain.

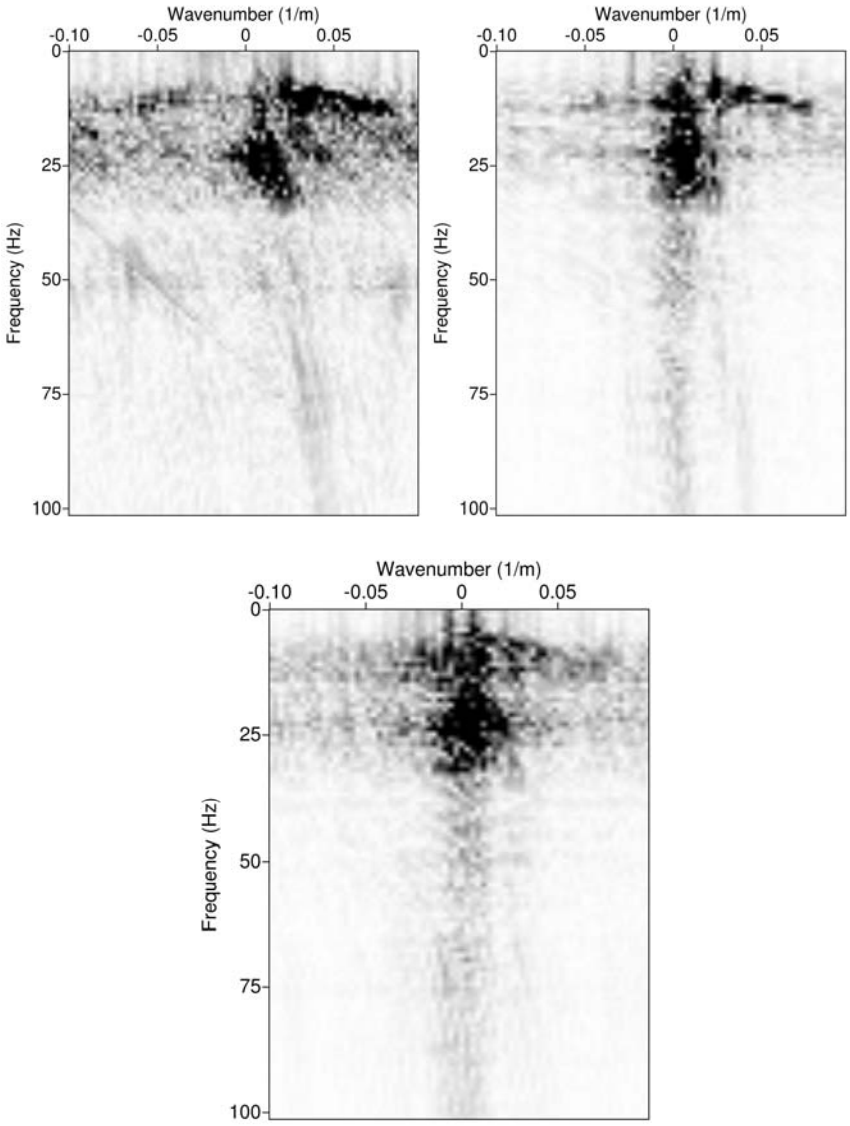

Figure 3.21b. (f, k_x)-amplitude spectrum of field record (left) after 2D standard array-forming (center) and 2D Robust MVDR beamforming (right); same display parameters are taken.

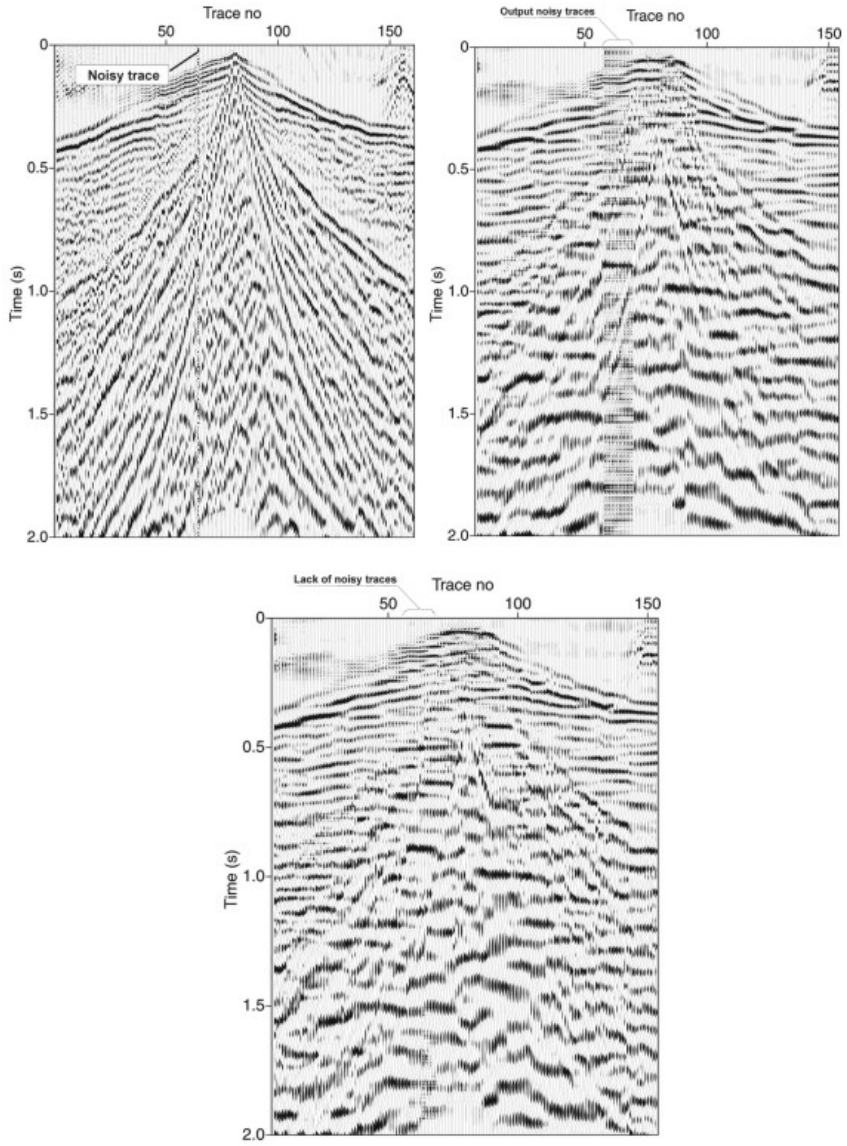

Figure 3.22. Field record (up-left) after standard array-forming (up-right) and Robust MVDR beamforming (down) displayed in the time domain.

Also, the Robust MVDR beamformer can attenuate the noisy traces that do not carry seismic information. In this example, one noisy trace can appear multiplied on the standard-array response while its presence is completely attenuation on the MVDR beamformer response (see Figure 3.22).

3.4.2 Robust MVDR on partial-3D single-sensor field data

We next considered a partial-3D shot record with the 3D Robust MVDR beamformer (see Figure 3.23). In this case, we applied the MVDR algorithm for an array with 12 inline × 5 crossline traces. The standard array-forming and MVDR beamforming responses are displayed in Figure 3.24a. By comparing these two results, we notice better out-of-the-new-spatial-band energy attenuation by the MVDR algorithm (see Figure 3.24a). The size of the new spatial band depends on the value of the group interval, here 10 m. Looking at both responses displayed in the (f, k_x)-domain (see Figure 3.24b) we can clearly see that the standard array-forming response has a remaining surface wave energy concentrated around a wavenumber of 0.05 m^{-1} and a frequency of 10 Hz, whereas the MVDR beamforming response is much less. The error in amplitude e_{fk} shows a value of 0.0142 for the MVDR beamforming and e_{fk} = 0.0158 for the standard array-forming response.

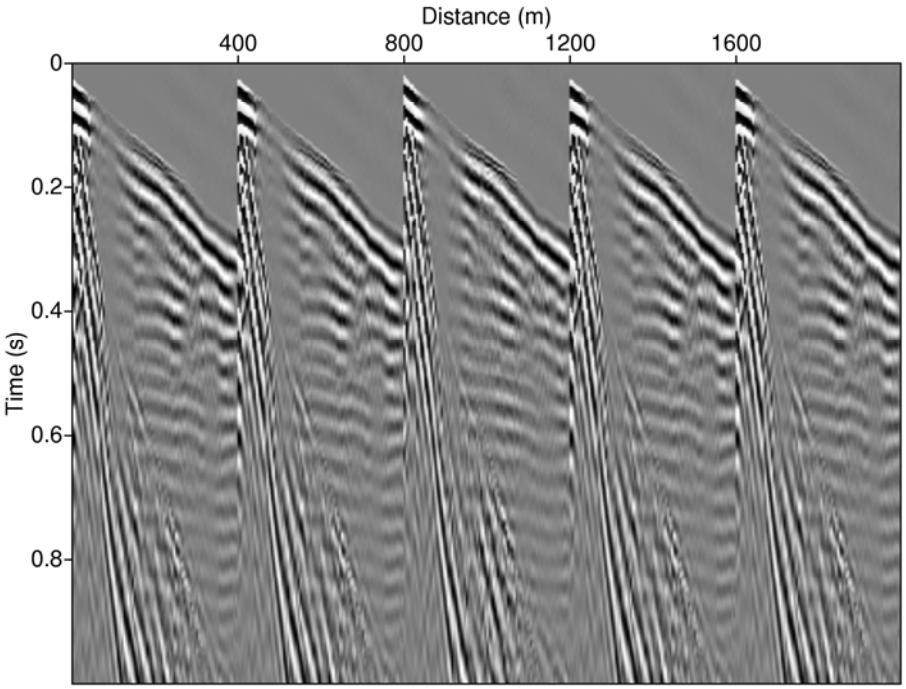

Figure 3.23. One record of field data

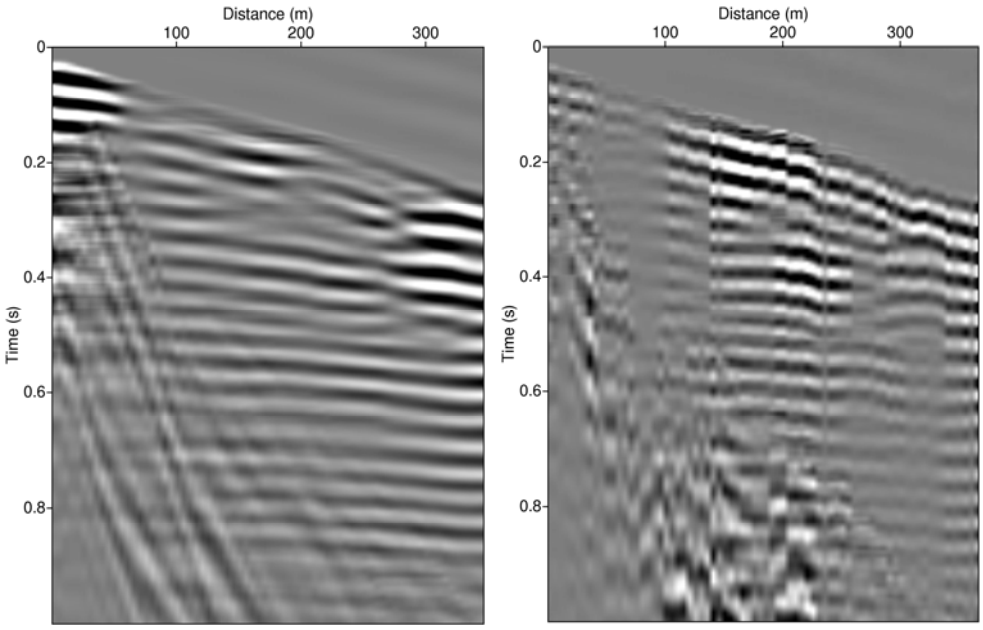

Figure 3.24a. Field record after 3D standard array-forming (left) and 3D Robust MVDR beamforming (right) displayed in the time domain

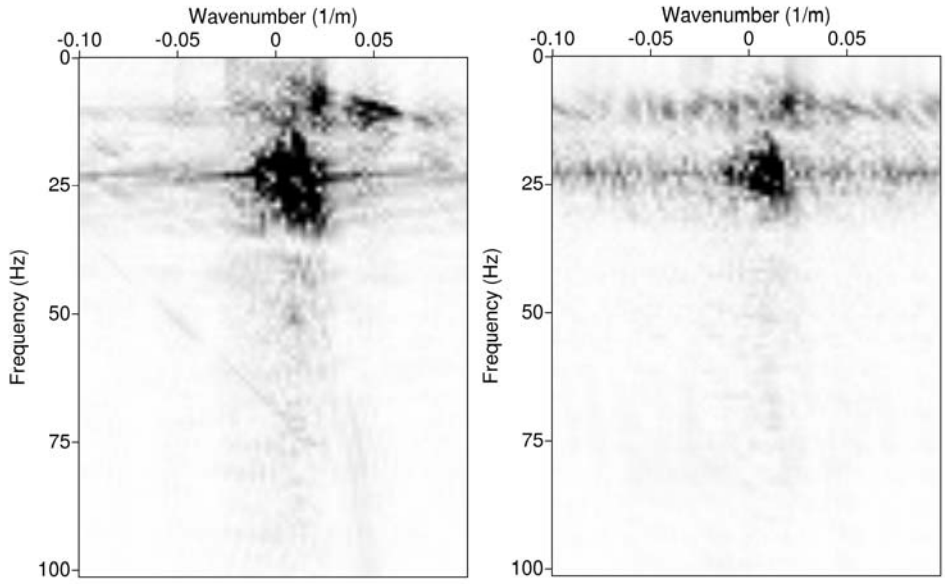

Figure 3.24b. (f, k_x)-amplitude spectrum of the field record after standard array-forming (left) and Robust MVDR beamforming (right); same display parameters are taken.

3.4.3 Data processing of the 3D standard array-forming and 3D Robust MVDR beamforming responses

The effectiveness of the noise attenuation performed by the Robust MVDR algorithm can also be seen on stacked sections. A usual way to attenuate the noise is to stack the seismic data in the CMP (common midpoint) domain after the normal moveout corrections. When we use a standard array to record the seismic data, the noise is first attenuated by this array and then by the CMP stacking. Thus, we use two ways to increase the signal-to-noise ratio, apart from other techniques such as filtering.

We have so far demonstrated that only on shot records does the MVDR algorithm result in better surface-wave attenuation than standard array forming. The analyzed data set contains 157 records, each representing five seismograms with 160 traces spaced at 5 m. This data set was introduced to 3D standard array forming and 3D Robust MVDR beamforming. The results of the two approaches were further processed using the same flow to allow for comparison (see Table 3.1). Static corrections were applied first, using a replacement velocity of 1750 m/s for a final datum of + 450 m above sea level. The remaining surface waves were further eliminated using an *f-k* filter, *f-x* deconvolution, and a band-pass frequency filter of 20–24–64–70 Hz. The second step of array forming, namely the resampling to a new group interval of 10 m, was next done. Amplitude equalization was achieved using automatic gain control for a window of 300 ms. Top mute was applied to remove the first arrivals and the advance noise. The CMP stacking of seismic data used a 2D velocity model provided by the velocity analysis.

When we compare the two time sections obtained in this way we notice an improvement in the continuity of some reflectors all over the section when applying the 3D MVDR responses (see Figure 3.25). For example, looking on the left side of both time sections, the continuity of those reflections located between 0.5 s and 1 s is stronger. These same reflections are weaker and discontinuous with the 3D standard array-forming result (see Figure 3.26).

Both sides of the time sections show high reflectivity. This is due partially to the favorable signal-to-noise ratio that characterizes the recordings and partially to the 3D robust MVDR beamforming algorithm. The central part of the section has a very low signal-to- noise ratio because of the low quality of input data; this is a result of the field conditions of rugged topography and unconsolidated soil giving a bad geophone coupling. Use of the 3D beamformer enhanced the signal-to-noise ratio of the analyzed recordings.

Processing steps	*Parameters*
Input seismic data	2 s trace length 157 shots
Geometry	2D land geometry
Static corrections	Replacement velocity = 1750 m/s Final datum = + 450 m.asl
Desampling in time	2 ms
Trace muting	Top (first arrivals and noise before)
Automatic Gain Control	300 ms
f-k filter	Accept, fan polygon
Trace muting	Top (remaining noise)
Automatic Gain Control	300 ms
Band-pass frequency filtering	Zero phase, frequency, 20–24–64–70 Hz; Notch filter, 50 Hz, window of 4 Hz
f-x Deconvolution	Wiener Levinson, 500 ms, 20–70 Hz
Automatic Gain Control	500 ms
Spatial resampling	Group interval of 10 m
Velocity analysis	Yes
NMO corrections	Yes
Stacking	Yes

Table 3.1. Data processing steps of field data set, and parameters used.

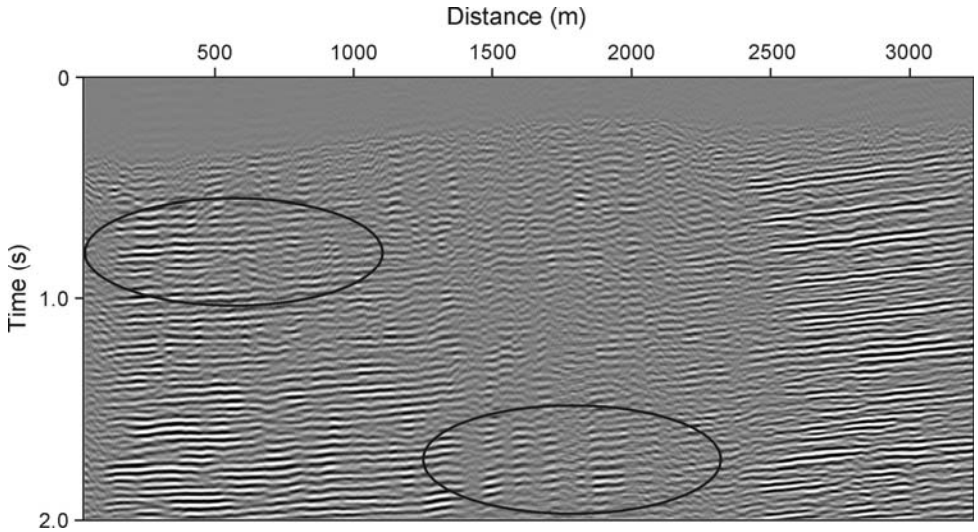

Figure 3.25. Time section of field data set, based on 3D Robust MVDR beamforming

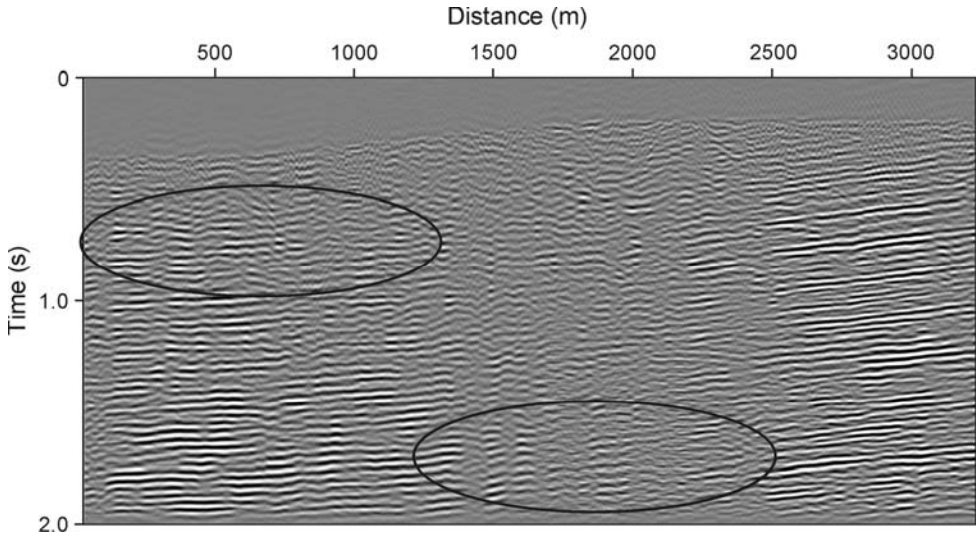

Figure 3.26. Time section of field data set, based on 3D standard array-forming

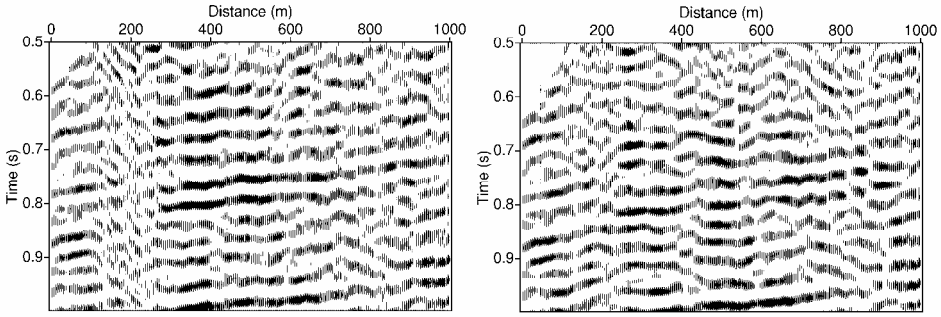

Figure 3.27. Windowed time sections based on 3D robust Robust MVDR beamforming (left) and 3D standard array-forming (right)

The amplitude of some reflectors was higher after Robust MVDR beamforming than after standard array forming. See, for example, the group of reflectors located between 1500–2000 m on the time section at the time interval of 1.6–1.9 s (see Figure 3.25). Some shallow reflectors also appear to be more continuous (see Figure 3.27).

3.5 Conclusions

The Robust MVDR beamformer is an algorithm proposed to attenuate undesired energy located within the new spatial band defined by the value of the group interval. Modeling results show that it can be successfully used for seismic data in combination with single-sensor recordings. The application of 2D or 3D Robust MVDR beamforming to synthetic data showed noise attenuation appreciably better than that provided by either 2D or 3D standard array forming. Qualitative and quantitative estimation of this attenuation made by comparing the responses displayed in the (t, x)- and (f, k_x)-domains support

this observation. The error shows smaller values for Robust MVDR beamforming in all cases, for both synthetic and field records, which means that this algorithm provides us with more acceptable responses than those obtained by alternative processing.

Application of the 3D Robust MVDR beamformer to post-stack data enhanced the signal-to-noise ratio more than standard array forming, including in those areas where the SNR is very low. We notice more continuous reflections and higher amplitudes in the time section based on the Robust MVDR responses. In addition, the Robust MVDR algorithm works well with data that have a very low signal-to-noise ratio, which is encouraging because land seismic data often have this characteristic.

Chapter 4

The use of single sensors in processing; stereotomography[2]

4.1 Introduction

In this chapter the use of densely spaced single sensors in processing is exploited. In the previous chapter the effect of two types of algorithms was analyzed regarding the noise attenuation (a source-generated coherent noise, i.e., ground-roll). Here we do not do any (in-line) array-forming but treat the dataset as a single-sensor dataset to be processed. Since it is a single-sensor dataset, the output stacked section contains more traces than the section that

[2] This chapter is based on: Panea, I., Landa, E., Drijkoningen, G.G., Baina, R., 2005. Imaging using post-stack stereotomography in areas with low signal-to-noise ratio, Journal of the Balkan Geophysical Society, Vol 8(4), pp. 161-174

would have been obtained if the array data was used. Actually, the analysis and processing we are going to discuss in this chapter would not have been possible at all if we would have used array data because then there would have been too few traces in the final section. On top of that, since the topography of the area was quite substantial, arrays would have destroyed part of the desired signal (reflected waves) due to static errors. It is obvious for such areas that single-sensor data allows tackling these problems.

The processing step we are going to discuss in this chapter is stereotomography. Stereotomography is a method that determines a macro-velocity model from seismic reflection data [*Billette and Lambaré* (1998)]. In its original form, it was based on the automatic picking of locally coherent events on pre-stack data (common shot, offset, midpoint and receiver gathers). Since the automatic picking on pre-stack data characterized by low signal-to-noise ratios does not provide reliable picks, the resulting velocity model can be far away from the true model. Therefore, *Lavaud et al.* (2004) proposed a modification to stereotomography based on the automatic picking of local coherent events on post-stack data, namely on a Common-Reflection-Surface (CRS) stack. We will use this approach in this chapter. Next, the velocity model is determined based on the inversion of the travel-times picked on the CRS stack. The combination of these two steps is known as "post-stack stereotomography".

The post-stack stereotomography was applied with good results on synthetic seismic data and marine seismic dataset [*Lavaud, Baina and Landa* (2004), *Lambaré, Alerini and Podvin* (2004)]. In addition, the post-stack travel-time picking seems to be a robust and reliable procedure commonly used in seismic interpretation *[Lavaud et al.* (2004)]. This method belongs to the slope tomography methods proposed during the last decade [*Billette and Lambaré* (1998), *Chauris, Noble, Lambaré and Podvin* (2002), *Duvenek and Hubral*

(2002)]. The optimal wavefront parameters are obtained during the generation of the CRS stack *[Jäger, Mann, Höcht and Hubral* (2001)]. The stereotomography has been implemented in 2D [*Billette, Le Begat, Podvin and Lambaré* (2003)] and 3D [*Chalard, Podvin, Le Begat, Berthet and David* (2002)].

In this chapter we focus on a field dataset with a low signal-to-noise ratio; this dataset was recorded using single sensors. Because of its low signal-to-noise ratio, the velocity analysis performed on the CMP gathers with the standard procedure did not provide a very reliable 2D velocity model. Most of the CMP gathers were avoided during this analysis because of their low desired signal level. Next, the depth migration does not run well because the interval-velocity model derived from the conversion of the stacking velocities is not good enough. Knowing that the signal-to-noise ratio can be improved, also, by stacking of the data it seems that the post-stack stereotomography can be used with good results. In addition, there is a possibility to verify the accuracy of the velocity model by a Common-Image-Gathers (CIG) analysis, during the migration step.

In this chapter we first briefly describe the principles of the stereotmography method based on the CRS-stack approach. Then, we introduce the single-sensor dataset used for analysis and discuss the two approaches in two separate sections. In this way we compare the standard CMP-based approach with the CRS-stereo-tomography approach. Although the algorithm used is 2D, some 3D effects have been used too. Cross-line arrays would, in theory, help increasing the signal-to-noise ratio even more. Via a single-sensor field dataset we will also show that the results are even improving when the data is stacked in the cross-line direction.

4.2 Background to the post-stack stereotomography

We start with a short description of the stereotomography method, also known as the "pre-stack stereotomography" [*Billette and Lambaré* (1998)]. Stereotomography is a method used for estimating velocity macro-model from seismic reflection data and belongs to the slope tomographic methods.

The velocity model is obtained by the inversion of the travel-times picked on locally coherent events in a gather of traces (for example common source, common receiver, common offset, common CDP gathers). In addition, two slopes are determined for each event; the first one in the common source gather and the second one in the common receiver gather. These slopes correspond to the horizontal component of the slowness vectors, according to the ray theory [*Billette and Lambaré* (1998)]. Each locally coherent event picked on a given trace is described by source and receiver positions ($S = (x_S, z_S)$ and $R = (x_R, z_R)$), a two-way travel-time t_{SR}, and two local slopes ($p_{Sx} = \Delta t/\Delta x_p$ and $p_{Rx} = \Delta t/\Delta x_p$); this information define the "observed" data part of stereotomography, noted with $d_i^r = [(S, R, p_{Sx}, p_{Rx}, t_{SR})_i]_{i=1}^{N_e}$ for N_e picked events.

The source and receiver positions are known from the navigation files obtained in the field. The two-way traveltime is read on the data. The slope is defined as the tangent of a coherent event measured from pre-stack seismic trace gathers [*Billette et al*. (2003)]. In a 2D trace gather (can be a common source, common receiver, common offset, common CMP gather), we can measure the slope, p_x, of a given coherent event at a given receiver or source location (see Figure 4.1). On a common source gather or common receiver gather, the local slope of a reflected event provides a direct estimation of the horizontal component of the slowness vector. Next, these slopes can be used to reconstruct the path to the reflecting / diffracting point X starting from the surface. This reconstruction requires, also, an initial velocity model. Based on

this information, the rays are traced down from the surface until a point where they should intersect if the velocity model is good. In this case, the picked travel-time has to be equal with the sum of the two one-way travel-times computed for both rays that cross each other. If the picked event is a primary reflection or diffraction it can be associated with a reflecting / diffracting point X. This point X is localized at the intersection of the two ray segments; the first one goes from the source point, S, down to the reflecting / diffracting point X, $S \rightarrow X$, and, the second one, goes from the reflecting / diffracting point X up to the receiver, R, $X \rightarrow R$. A ray segment means a part from a ray trajectory completely defined by a starting point and an ending point, the initial or final direction and the travel-time.

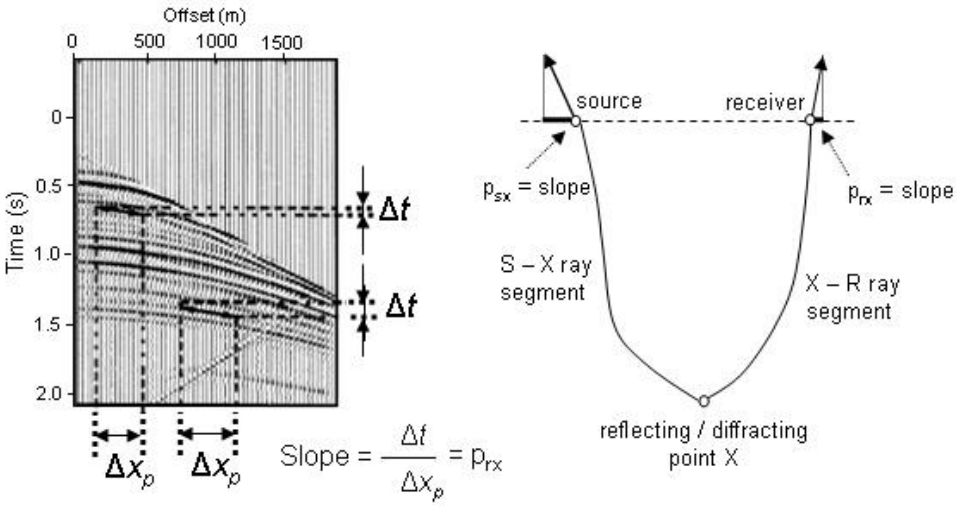

Figure 4.1. The slope on a common-source gather and the slope in ray theory [after *Billette and Lambaré* (1998)]

Two conditions have to be satisfied by these rays, namely they have to cross each other at their ending point and they have to fit the data in positions,

slopes and two-way travel-times. These conditions, also known as boundary conditions, are not entirely satisfied in case of an incorrect velocity model; therefore, one of them has to be variable. Three cases were proposed here.

In the first one, none of the boundary conditions are fixed, which means that the ray segments do not have to join each other in depth or fit the data at the surface (see Figure 4.2). This is the general case of the slope tomographic methods; here, the velocity and ray segments update until all the boundary conditions fit the data and the ray segments join each other at a point in depth.

The second case is found in the Controlled Directional Reception (CDR) method [*Sword* (1987)]. It assumes the surface boundary condition fixed, meaning that the upper extremities of the two ray segments have to fit the data at the surface; the lower extremities do not have to fit in depth (see Figure 4.3).

In the last case, the crossing point is fixed (the rays have to cross each other at the deepest point) and the surface boundary condition is relaxed (both rays do not fit the data at the surface). This is the assumption take it into account in *stereotomography* (see Figure 4.4).

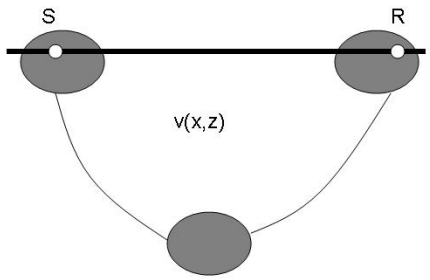

Figure 4.2. No boundary condition is fixed: ray segments do not have to join each other in depth or fit the data at the surface [after *Billette and Lambaré* (1998)]

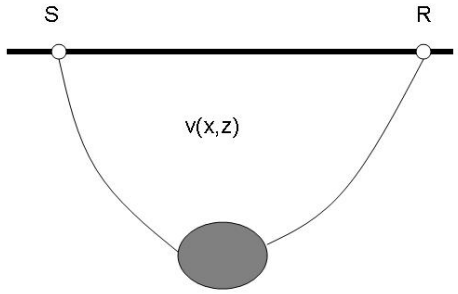

Figure 4.3. Surface boundary conditions are fixed (the upper extremities of the two ray segments have to fit with data at the surface); their other extremities do not have to fit in depth [after *Billette and Lambaré* (1998)]

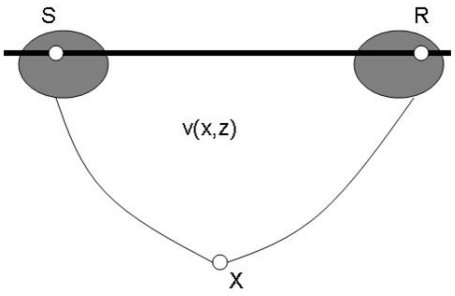

Figure 4.4. Crossing-point is fixed; the two ray segments do not have to fit the data at the surface [after *Billette and Lambaré* (1998)]

Stereotomography characterizes each picked event by a pair of ray segments that terminate at the same point in depth (called X). These ray segments propagate upwards from the point X into an initial velocity model with known directions to the source and receiver and two one-way travel-times; this information define the so-called model part, *m*, of stereotomography, $m = [[(X, \beta_S, \beta_R, T_S, T_R)_i]_{i=1}^{N_e}, [C_j]_{j=1}^{J}]$. Based on the model part analysis, a "computed" dataset is obtained, $d_i^c = [(S, R, p_{sx}, p_{rx}, T_{SR})_i]_{i=1}^{N_e}$ (see Figure 4.5).

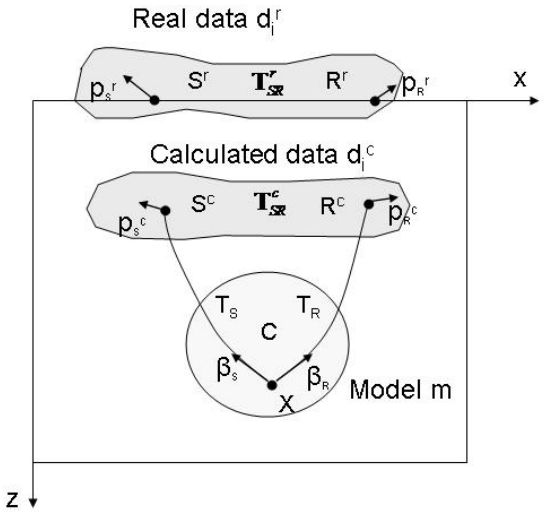

Figure 4.5. Calculated data, d_i^c, are obtained from an initial model, *m*; they do not match real data, d_i^r [after *Billette and Lambaré* (1998)]

The travel-times and local slopes contained by the "observed" dataset, d_i^r, are determined by automatic picking. The stereotomographic picking can be done in the time domain. Also, *Chauris et al.* (2002) demonstrated that it can be done in the depth migrated domain because of higher signal-to-noise ratio, better coverage of the model and easier quality control of the picks. The second step, after the automatic picking, is the visual check of the picks and manual correction [*Alerini et al.* (2003)]. *Lambaré et al.* (2003) proposed a picks selection based on the statistical properties of the population of stereotomographic picks; this is done based on an interactive visualization of the picks as a function of thresholds. The outlier pick, in terms of slopes, equivalent model parameters, picks with too small coherency or energy are eliminated [*Lambaré et al.* (2004)]. The following control parameters are used

in order to increase the accuracy of automatic picking: the distance between analyzed traces, the time sampling increment, the width of Hamming window, a threshold on the semblance value, a threshold on the product of the semblances from common shot, common receiver and common offset gathers.

As is written above, the model part of stereotomography, *m*, is represented by a velocity macro-model, C_m, and a set of pairs of ray segments parameters associated with each picked event ($[(X, \beta_S, \beta_R, T_S, T_R)_i]_{i=1}^{N_e}$ for N_e locally coherent picked events). The initial velocity model is considered homogeneous and described by a number of nodes. The location of the reflecting / diffracting point, X, is obtained during the picking procedure. The angles are computed based on simple geometrical considerations, assuming a homogeneous medium. Each of the two one-way travel-time pairs is set to half of the corresponding two-way travel-time picked from the data. Initially, the ray paths do not reach the surface in the observed positions; their correction is made assuming the initial model correct and varying the ray segments parameters *[Billette et al.* (2003)]. A first version of the velocity model is obtained by a stereotomographic inversion that consists in fitting all the picked data with the data calculated by ray-tracing [*Chalard et al.* (2002)]. Next, all picks are used to upgrade simultaneously the associated rays and velocity perturbation having as result the final velocity model.

More accurate picks are obtained if we use stacked data because the noise level is lower on the stacked data compared to that one from pre-stack data. The so-called post-stack stereotomography uses picked travel-times on the Common-Reflection-Surface stack, so the post-stack domain. The CRS stack gives an accurate zero-offset approximation of the seismic section; in addition, the procedure used to generate the CRS stack is also used to compute the wavefront parameters for each CMP position and time sample (emergence angle of the zero-offset ray and two radii of wavefront curvatures R_N and R_{NIP}).

These three parameters are associated with two hypothetical waves, namely, the normal wave (N) and the normal-incidence-point wave (NIP). The N and NIP waves, also known as eigenwaves, result from two hypothetical experiments, where a point (diffractor-like) and a reflector are the secondary source in the subsurface. For example, Figure 4.6 shows a model with three homogeneous layers for these two types of cases. The NIP wave is obtained by placing a point source on a reflector (see Figure 4.6, left), so like a point-diffractor, and the N wave is obtained after a simultaneous excitation along a reflector (see Figure 4.6, right), so like an exploding reflector. In the vicinity of a point from the acquisition line, x_0, both wavefronts can be approximated by circles with radii of curvature R_{NIP} and R_N, respectively [*Jäger et al.* (2001)].

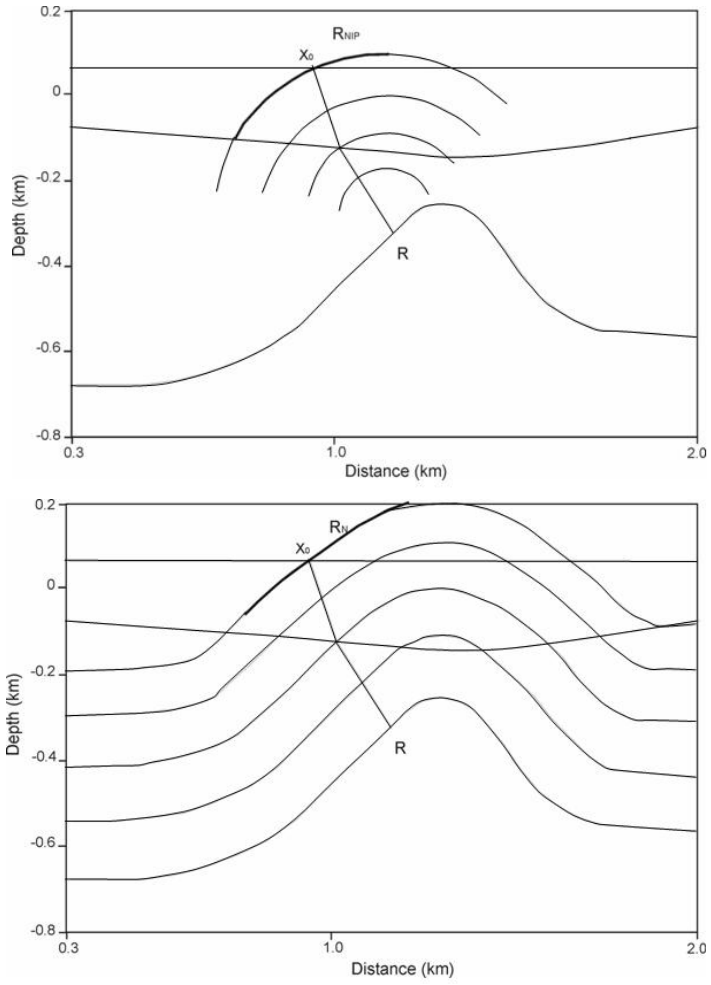

Figure 4.6. NIP wave for a point source at R position (up) and N wave for an exploding reflector at R position (down), [after *Jäger et al.* (2001)].

The computing of the CRS stack does not depend on a macro-velocity model [*Jäger et al.* (2001)], as opposed to the CMP stack. The CRS-stacking operator is defined as:

$$t_{CRS}^2(x_0,h)=\left(t_0+\frac{2\sin\beta}{v_0}\left(x_{cmp}-x_0\right)\right)^2+\frac{2t_0\cos^2\beta}{v_0}\left(\frac{\left(x_{cmp}-x_0\right)^2}{R_N}+\frac{h^2}{R_{NIP}}\right), \qquad (4.1)$$

where x_0 is the output position, x_{CMP} is the position of midpoint between source and receiver (= $(x_R + x_S)/2$), h is the half offset (= $(x_R - x_S)/2$), v_0 is the near surface velocity, t_0 is the zero-offset two-way traveltime.

The three parameters (β, R_N and R_{NIP}) define the stacking surface associated to the zero-offset traveltime, t_0. If the point $P_0 = (x_0, t_0)$ is known, all we need is the near-surface velocity, v_0 [*Jäger et al.* (2001)]. This parameter is assumed to be known, e.g. from other seismic studies performed in the studied area.

It has been shown that a CRS stack improves the signal-to-noise ratio and provides a better continuity of reflectors; this statement is based on synthetic and field data analysis. Each trace from the CRS stack is obtained by summing the traces from a super CMP gather so that a better noise attenuation is achieved. In addition, it is known that the procedure used to compute the CRS stack is also used to extract the information from the pre-stack data about the wavefront parameters; these parameters are determined for each point, P_0, of the zero-offset section [*Jäger et al.* (2001)].

Once we have the CRS stack, an automatic travel-time picking is performed, as a first step of the post-stack stereotomography method; here, only the locally coherent events are picked. The 2D velocity model is obtained after an iterative inversion process of the picked travel-times; it is a smooth model and contains interval velocities as a function of depth. Then, the velocity model will be used for the pre-stack depth migration of the stacked seismic data.

4.3 Application of post-stack stereotomography on a single-sensors seismic dataset recorded in a low signal-to-noise area

4.3.1 Seismic dataset: Acquisition and pre-processing

The post-stack stereotomography method is applied to a shallow land seismic dataset in order to get a more accurate velocity model necessary for the depth migration. The depth migrated section should show us a good depth image of the studied area, namely the proper positioning of the reflectors in depth. Before using this method, the land seismic data need a pre-processing in order to obtain common-midpoint (CMP) gathers having a signal-to-noise ratio as high as possible. The shallow seismic reflection dataset was recorded as a part of larger seismic survey (see Figure 4.7). Dynamite was used as a source and the seismic information was recorded using vertical-component geophones (see Table 4.1 for the data acquisition parameters).

In general, the quality of the seismic records is better toward the profile edges; clear reflectors can be seen even on the raw seismograms. The static effects are important; they can be identified on the raw seismograms. The elevation values vary along the seismic profile; the spread of the receivers for the first shot (1 – 160) covered 800 m and the maximum difference in elevation is 110 m (see Figure 4.8).

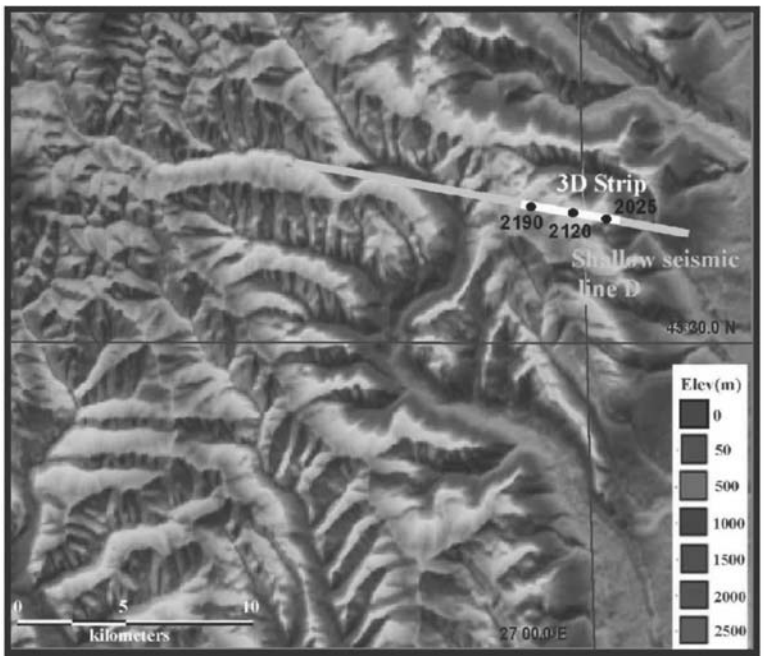

Figure 4.7. Topographic map of the studied area (Dumitresti-Ramnicu Sarat)

Parameters	
Receiver spacing	5 m
Receiver number	160
Source spacing	20 m
Source type	dynamite
Source size	200 g
Source depth	2 m
Sampling time interval	1 ms
Time length	4 s

Table 4.1. Data acquisition parameters

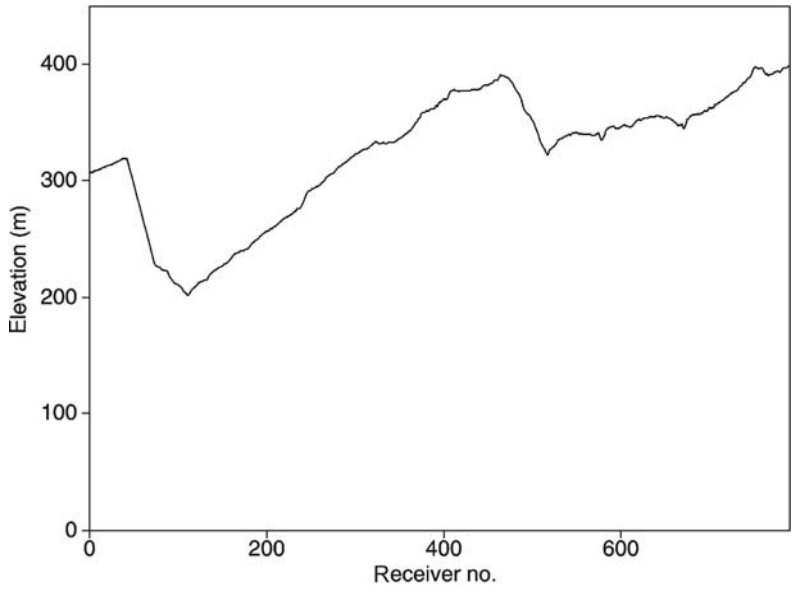

Figure 4.8. Elevation variation along the seismic reflection profile

It is known, from previous seismic studies, that there are important near-surface velocity variations. Together with the elevation effect, they create statics that have to be extracted from the recorded data. A final datum of + 450 m has been chosen in order to compute the static corrections and a replacement velocity equal with 1750 m/s has been used.

The signal-to-noise ratio of the seismic data is enhanced by different filtering techniques (band-pass, *f-k*, *f-x* Deconvolution). First, we tried to remove the ground-roll from the analyzed dataset by applying the *f-k* filter, followed by the other filters to eliminate the remaining noise (see Table 4.2 for the pre-processing steps). The top mute is used to remove refracted waves and noise before the first arrivals. Some of the very noisy traces were zeroed. The automatic gain control is used to normalize the energy along the traces.

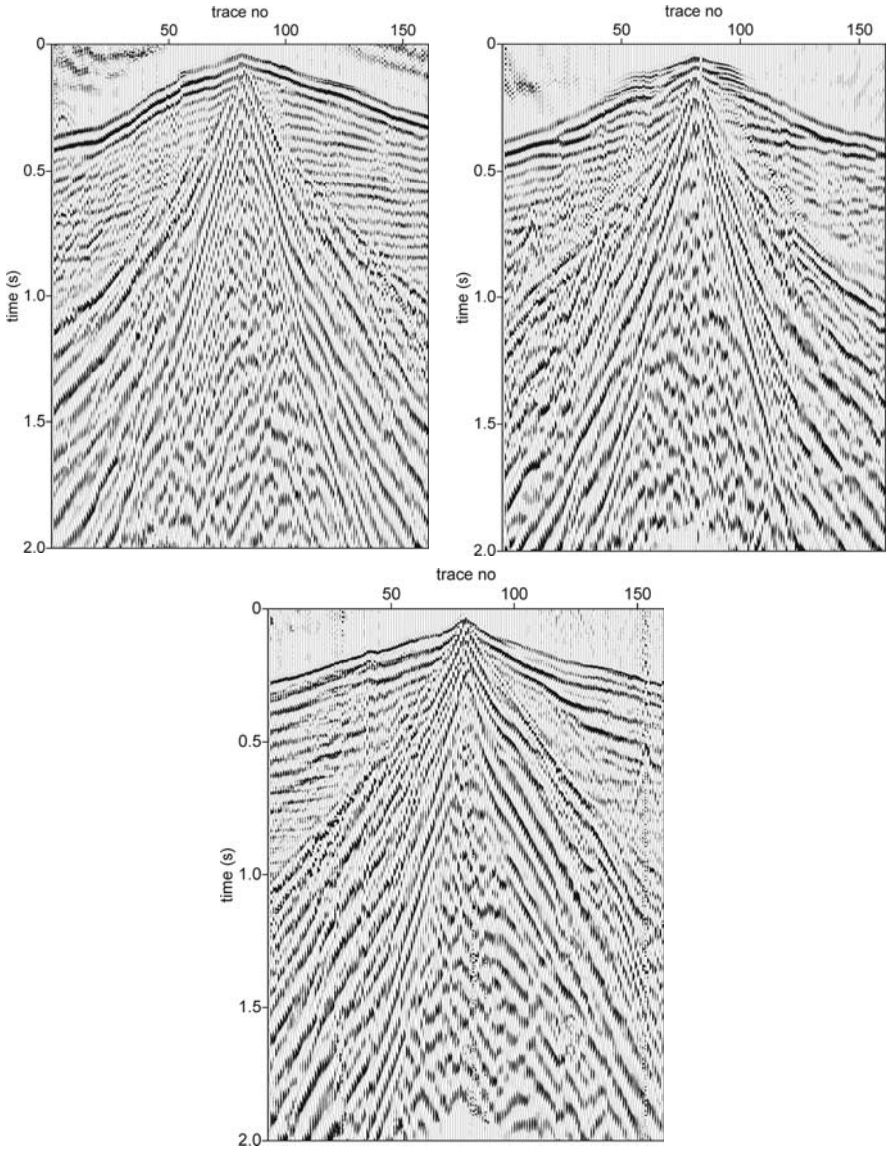

Figure 4.9. Raw seismograms: 2025 (up, left), 2120 (up, right) and 2193 (down), (their positions on the seismic profile are shown in Figure 4.7)

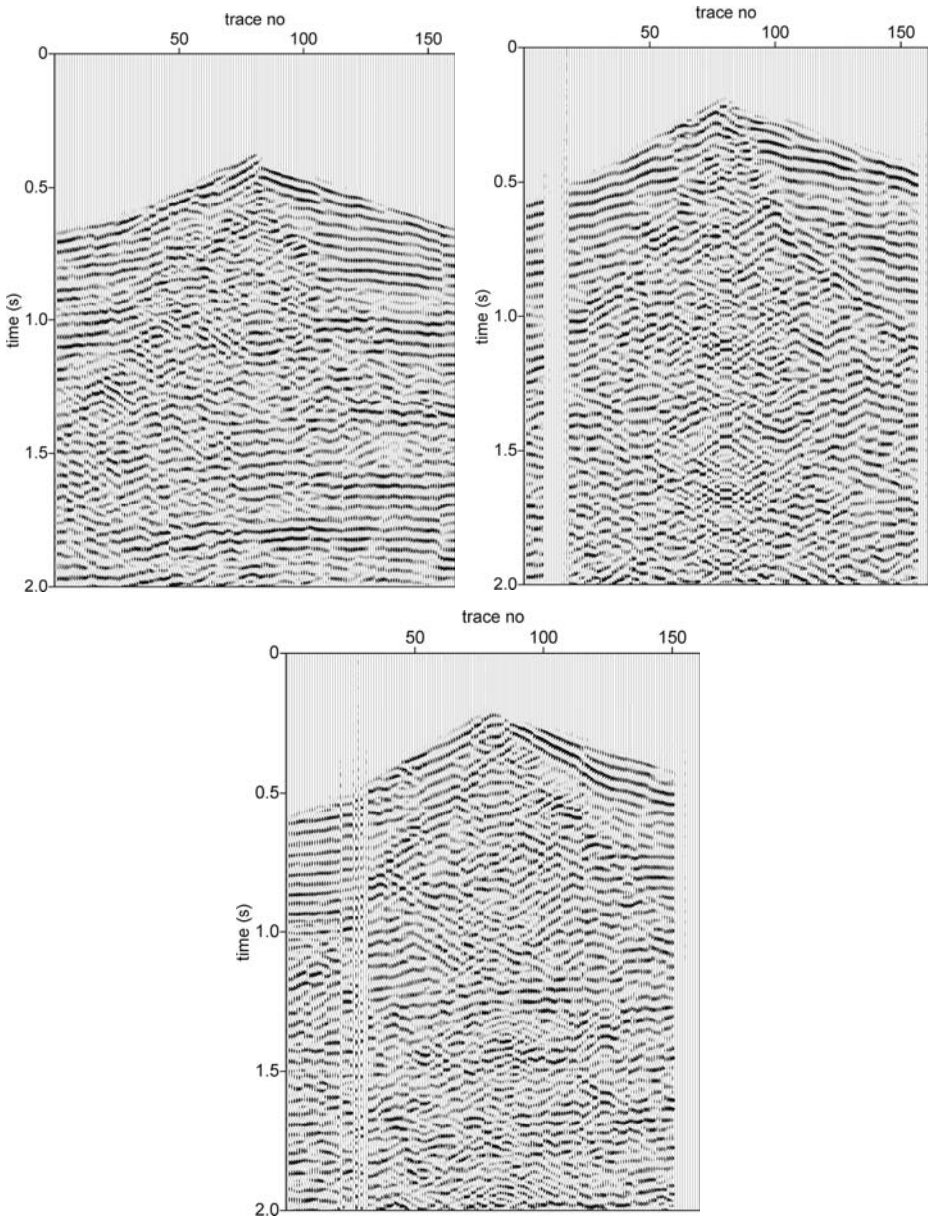

Figure 4.10. Pre-processed seismograms with static corrections applied: 2025 (left), 2120 (center) and 2193 (right), (their positions on the seismic profile are shown in Figure 4.7)

The full pre-processing flow is given in Table 4.2. In Figure 4.9, we display three of the most representative shots from the entire dataset and the results after pre-processing in Figure 4.10. The signal-to-noise ratio of these seismograms is indeed enhanced.

Pre-processing steps	*Parameters*
Input seismic data	2 s trace length 157 shots
Geometry	2D land geometry
Static corrections	Replacement veloc = 1750 m/s Final datum = + 450 m
Desampling in time	2 ms
Trace muting	Top (first arrivals and noise before them)
Trace Kill/Reverse	Kill (very noisy traces)
Automaic Gain Control	300 ms
f-k filter	Accept, fan polygon
Trace muting	Top (remaining noise)
Automatic Gain Control	300 ms
Band-pass frequency filtering	Zero phase, frequency, 20 – 24 – 64 – 72 Hz; Notch filter, 50 Hz, window 4 Hz
f-x Deconvolution	Wiener Levinson, 500 ms, 20 – 70 Hz
2D Spatial Filtering	Convolutional method
Trace Muting	Top (remaining noise)
Trace Muting	Bottom (remaining noise)
Automatic Gain Control	300 ms

Table 4.2. Data pre-processing flow

4.3.2 Imaging using standard CMP-based approach

The standard velocity analysis was performed on the CMPs obtained from the pre-processed data (see Figure 4.11). Then, the 2D velocity model was used to obtain the un-migrated section (the CMP stack). The CMP stack is displayed in Figure 4.12. As expected, the reflectivity between 0 – 1 km and 2.2 - 3.2 km is higher compared to that one seen on 1.5 – 2.2 km. The reflections are clear, continuous on great distances and characterized by high amplitude. The CMP stack shows us a simple geological structure, with important geological interfaces characterized by a high contrast of acoustic impedance and represented by clear and high amplitude reflectors. The poor quality of the stacked data on the central part of the CMP stack can be a result of many factors namely, the low signal-to-noise ratio of the input data, the presence of the surface waves, rough topography and near-surface effects. The elimination, by filtering, of the surface waves identified on a group of seismograms was difficult, even using the *f-k* filter. Also, the elevation and near-surface effects are very important on this segment of the seismic profile due to the field conditions (forest, frequent elevation variations on small horizontal direction with large amplitude, lateral variations of the near-surface velocities).

We expect to obtain a higher quality of this segment of the seismic profile after the post-stack stereotomography, based on the procedure used to compute the CRS stack and the 2D velocity model.

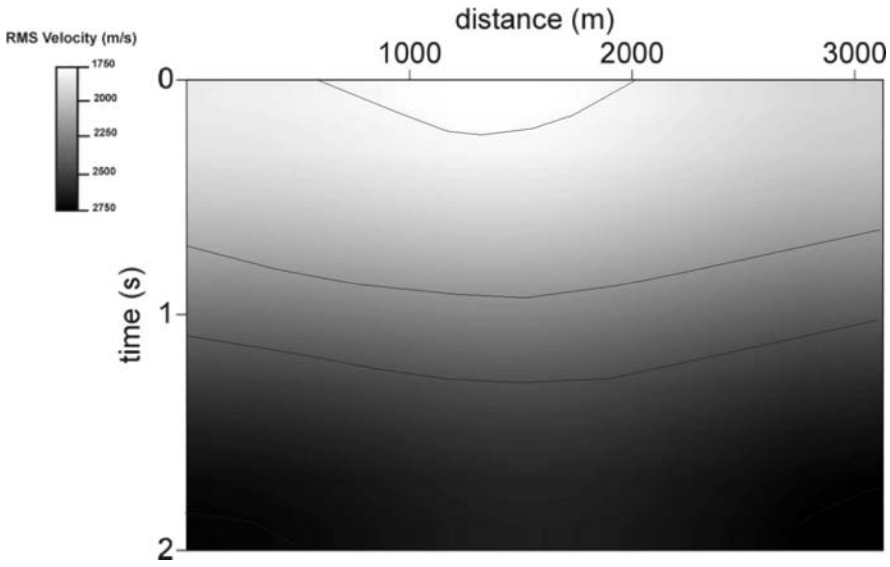

Figure 4.11. 2D velocity model based on CMP velocity analysis

4.3.3 Imaging using post-stack stereotomography

The CRS stack is a simulation of the zero-offset stack. The only difference between a CMP and CRS stack is the aperture used for stacking; the size of this aperture defines the number of the CMP gathers combined during stacking (multiple of CMP gathers in case of the CRS stack). The reflectivity of some areas characterized by low signal-to-noise ratio can be higher after this stacking (compare Figure 4.12 and Figure 4.13).

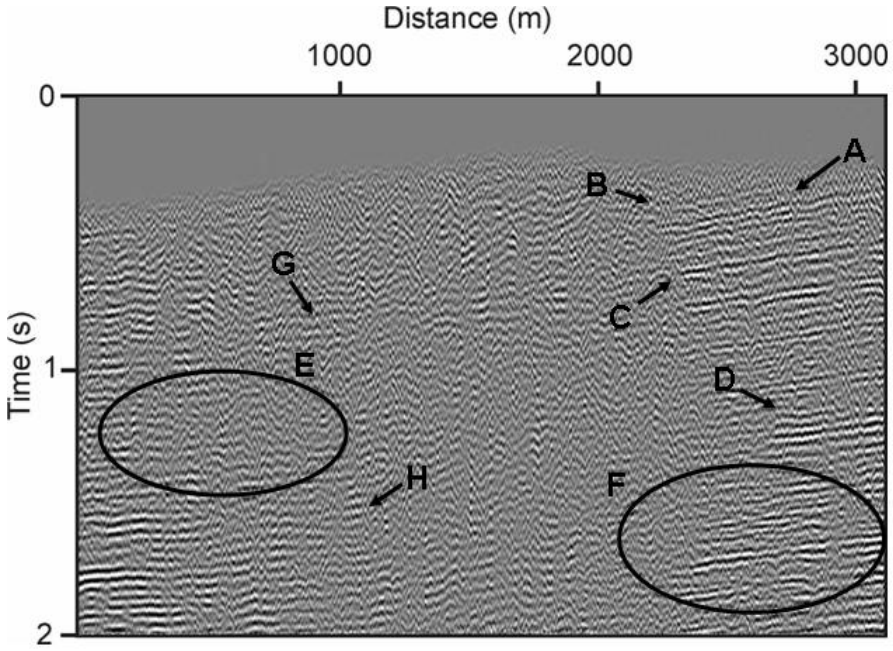

Figure 4.12. Un-migrated time section using the CMP-based stacking approach (input data is 2D single-sensor dataset)

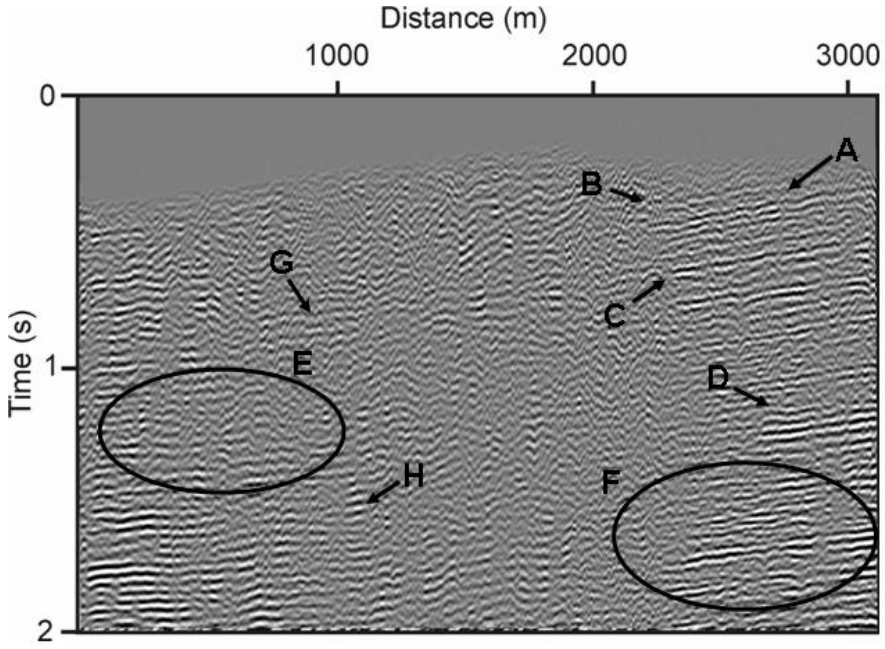

Figure 4.13. Common-Reflection-Surface (CRS) stack (input data is 2D single-sensor dataset)

The CRS stack enhanced some reflectors; their amplitude and continuity is more important compared to those from the CMP stack (see the group of reflectors C, D and F). As a counter-effect, the obtaining procedure of the CRS stack damaged the reflectivity of some areas, such as A, D and E. In addition, false reflectors (B) visible on the CMP stack, and un-supported by the known tectonic models for this area, were attenuated on the CRS stack. When we compare the central part of the CMP and CRS stacks we notice a higher reflectivity of the time interval 1.5 – 2 s, with clear short reflections (H); a reflector hard to follow on the CMP stack became more visible on the CRS stack (G).

Another important section obtained during the computing of the CRS stack is the CMP coherency section (see Figure 4.14). This section shows us high coherency values (light grey areas) where the reflections are stronger than in the rest of the section; in these areas, the corresponding attributes are considered reliable (Jäger et al., 2001). By comparing the CMP stack and the CMP coherency section we can separate the real events from those considered noise.

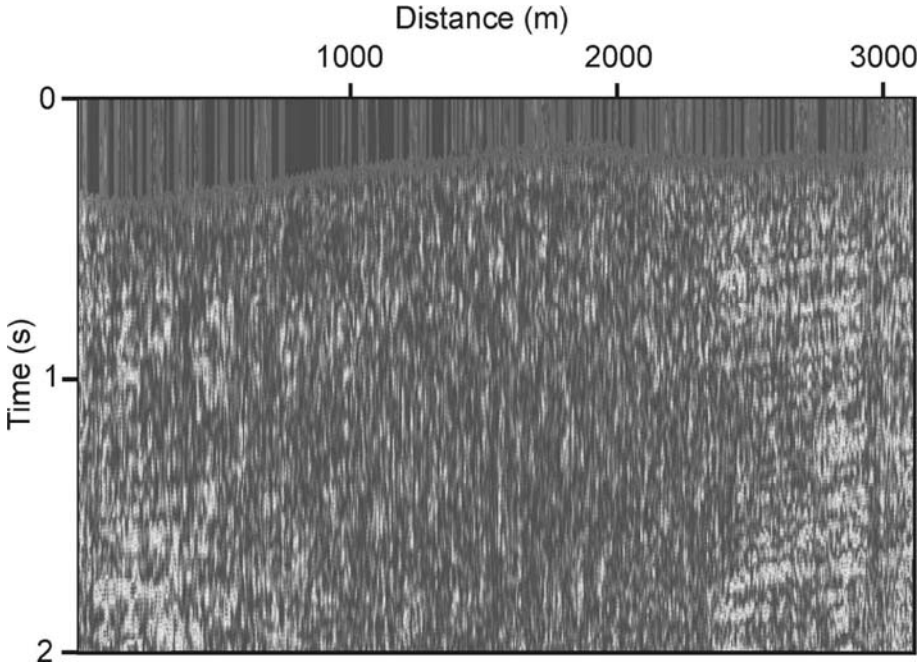

Figure 4.14. The CMP coherency section

An important parameter used in inversion is the angle β that is determined for each point of the CRS section (see Figure 4.15). The higher angle values correspond to those areas where the reflectors are clear, with high

amplitude and more continuous (light grey areas in Figure 4.15); these zones contain reliable angle information [*Jäger et al.* (2001)].

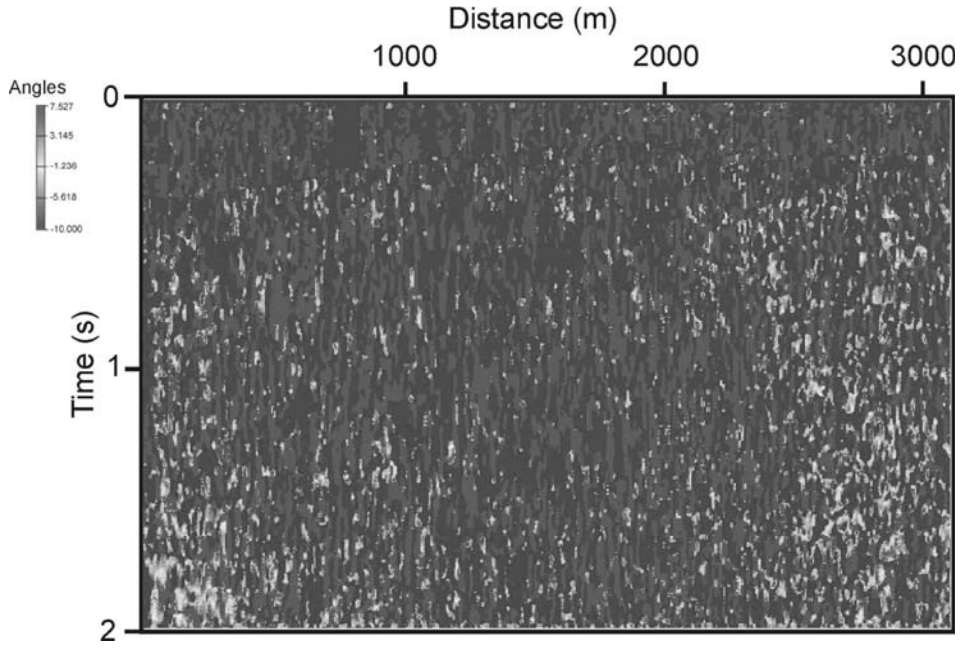

Figure 4.15. Angle section (input data is 2D single-sensor dataset)

Having all this information, the locally coherent events are automatically picked (see Figure 4.16). A half-window of 400 m and a semblance threshold of 0.75 are used for picking. Just a few events were picked on the central part of the section because of the lack of the continuous reflectors. The 2D velocity model is determined after the picked travel-time inversion (see Figure 4.17); the cell size is 200 m and a number of 10 iterations have been done. It is a smooth velocity model and it contains interval velocities as a function of depth.

The velocity model obtained from stereotomography is then used for a pre-stack depth migration, again using the Kirchhoff migration method. During this migration we have the possibility to verify the accuracy of the velocity in different points of the model. Two groups of Common-Image-Gathers (CIG) gathers where selected from two locations along the profile (see Figure 4.18); the traces in each CIG gather are sorted after offset. After an analysis of some CIG gathers, we can say that good velocity values are obtained on the gathers that contains flat events (see Figure 4.18, right); these gathers correspond to the data recorded on the eastern part of the profile which contains clear reflectors. The CIG gathers chosen from the central part of the profile do not show us clear flat reflectors, so we can not decide if the velocity values, at these locations, are good or not (see Figure 4.18, left).

The result of the depth migration is displayed in Figure 4.19. It shows, still, a poor continuity of the reflections in the central part of the seismic section, but better than that from the standard procedure output (see Figure 4.20 where we display the pre-stack depth migrated setion using the CMP-based approach). By looking at the reflection patterns we notice a difference between the frequency content of the signal on the left part and the right part of the seismic section (see Figure 4.19). This can be explained by lateral facies variation of the Quaternary and Upper-Pliocene deposits; in addition, the tectonic models known for this area do not show the presence of important faults or faulting area that could be responsible for the poor quality of the data on the central part of the profile.

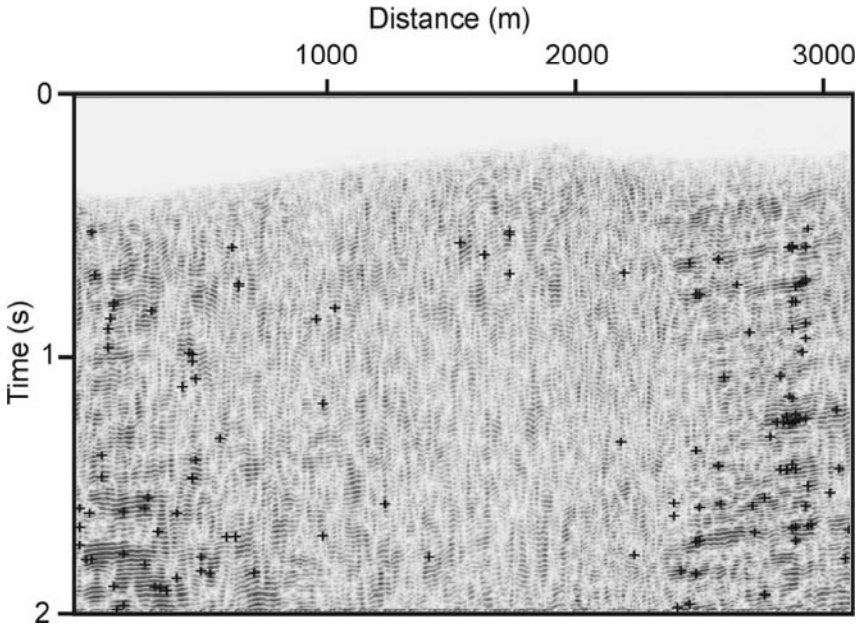

Figure 4.16. Automatically picked travel-times (input data is 2D single-sensor dataset)

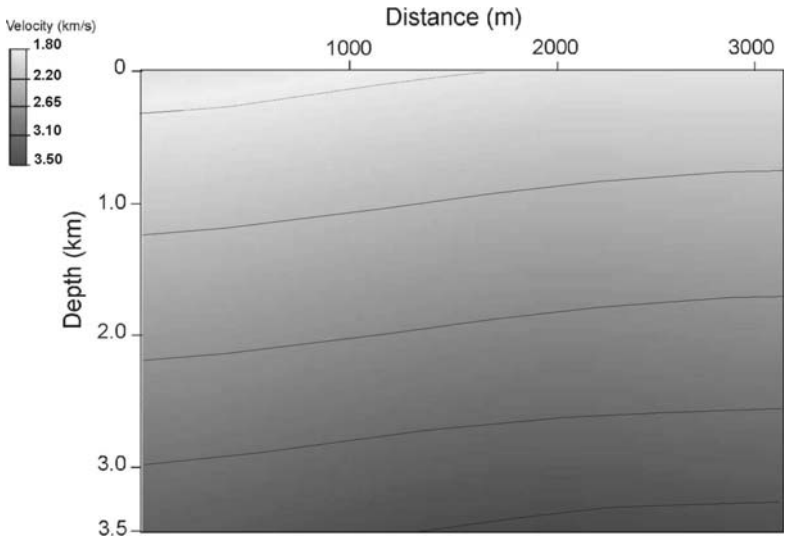

Figure 4.17. 2D velocity model from post-stack stereotomography (input data is 2D single-sensor dataset)

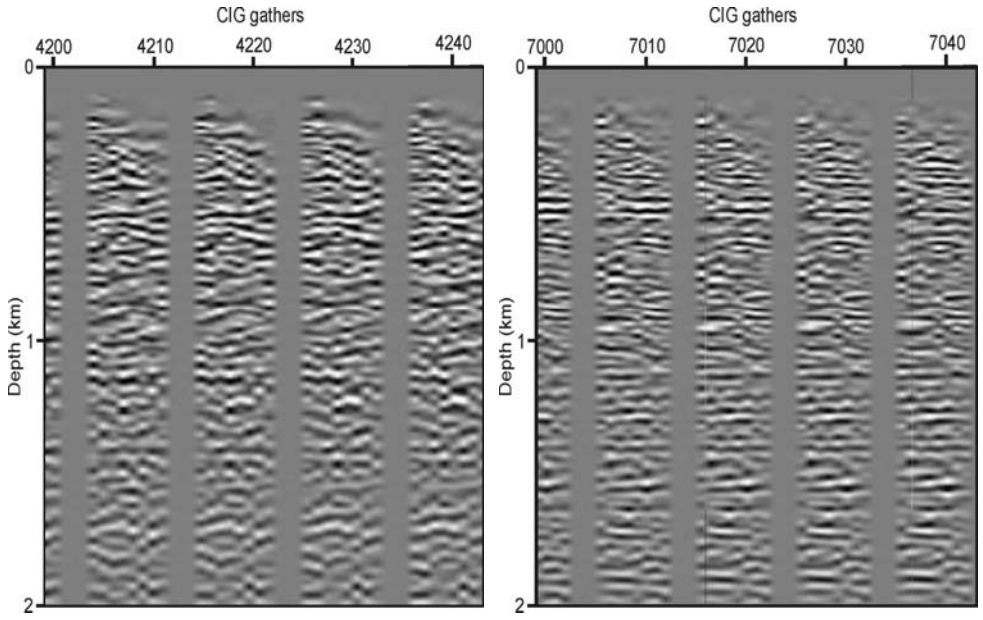

Figure 4.18. Common-Image-Gathers from the central part (left) and right end (right) of the profile (input data is 2D single-sensor dataset)

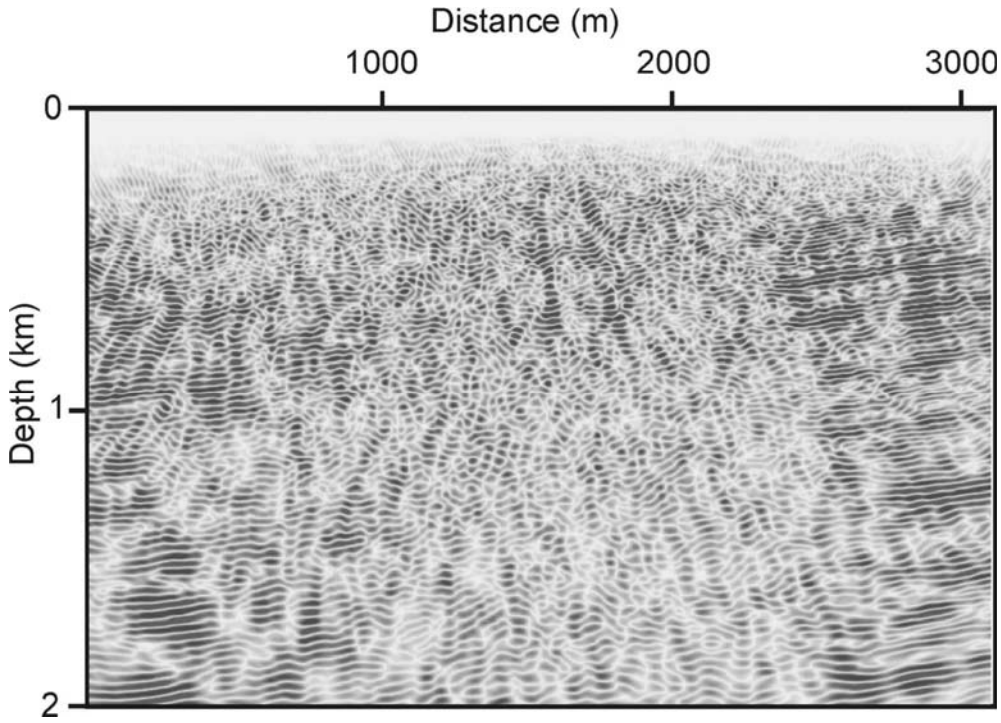

Figure 4.19. Pre-stack depth migrated stack with velocity model from travel-time inversion of picked events on CRS stack (input data is 2D single-sensor dataset)

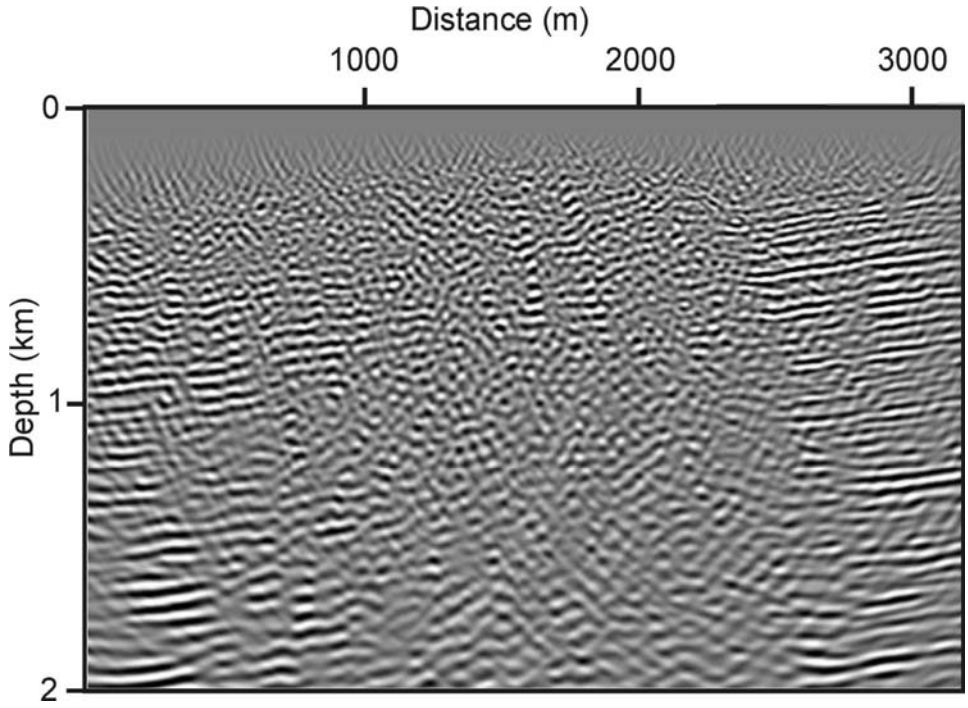

Figure 4.20. Pre-stack depth migrated section using the standard CMP-based imaging approach; the interval velocities are obtained from stacking velocities

4.3.4 2D versus 2D from cross-line stacked partial-3D data

A 2D dataset was obtained by stacking the partial-3D data in cross-line direction. This new dataset was processed following the approaches discussed in the previous sections. The un-migrated time section obtained using the CMP approach is displayed in Figure 4.21. As a first observation, we notice that the signal-to-noise ratio of the whole stack is higher than that one of the CMP stack based on 2D records (see Figure 4.12). The reflectivity is much higher on the time interval 1 – 2 s; pieces of reflections are clearer between 1000 – 2000 m.

More detailed information is obtained on the right side of the stacked section (thinner reflections can be easily seen). The signal-to-noise ratio of the whole stack can be enhanced using the CRS-stereotomography approach (partially, because we stack more traces than in the CMP-based approach). First, we computed the CRS stack (see Figure 4.22). Going further with the steps from the CRS-stereotomography approach, more picked travel-times are obtained after the automatic travel-time picking due to higher reflectivity (see Figure 4.23). Unfortunately, few picks are obtained on the central part of the stack in spite of the increased reflectivity. The velocity model obtained after the inversion of the travel-times is then used for the pre-stack depth migration, again using the Kirchhoff migration method. Its accuracy can be checked by analyzing the CIG-gathers (see Figure 4.24); we display for comparison the same CIG-gathers as position along the seismic profile obtained for the 2D dataset and 2D from crossline stacked 3D dataset. Looking at the CIG-gathers chosen from the dataset obtained after the crossline summing, we see clear flat events that indicate correct velocity values. If we compare these CIG-gathers with those obtained using 2D single-sensor records, we notice that they show flat events which are much higher in amplitude on the entire analyzed depth interval (see Figure 2.24). This is a proof that the velocity values are correct and their use during migration will place the reflectors in the right position in depth (see Figure 2.25). As expected, the depth image show more reflectors characterized by high amplitude on the edges of the depth section; the central part is still noisy. The depth migrated section obtained based on the CMP approach show little structural information compared to that obtained after the CRS-stereotomography approach (see Figure 4.26).

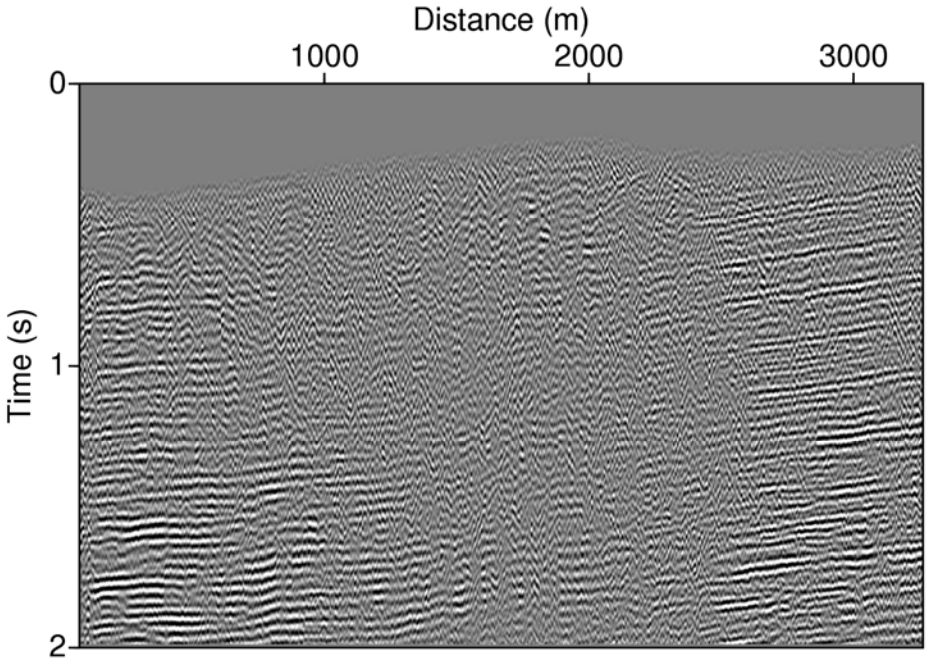

Figure 4.21. Un-migrated time section using the CMP-based stacking approach (input data is 2D from cross-line stacked 3D)

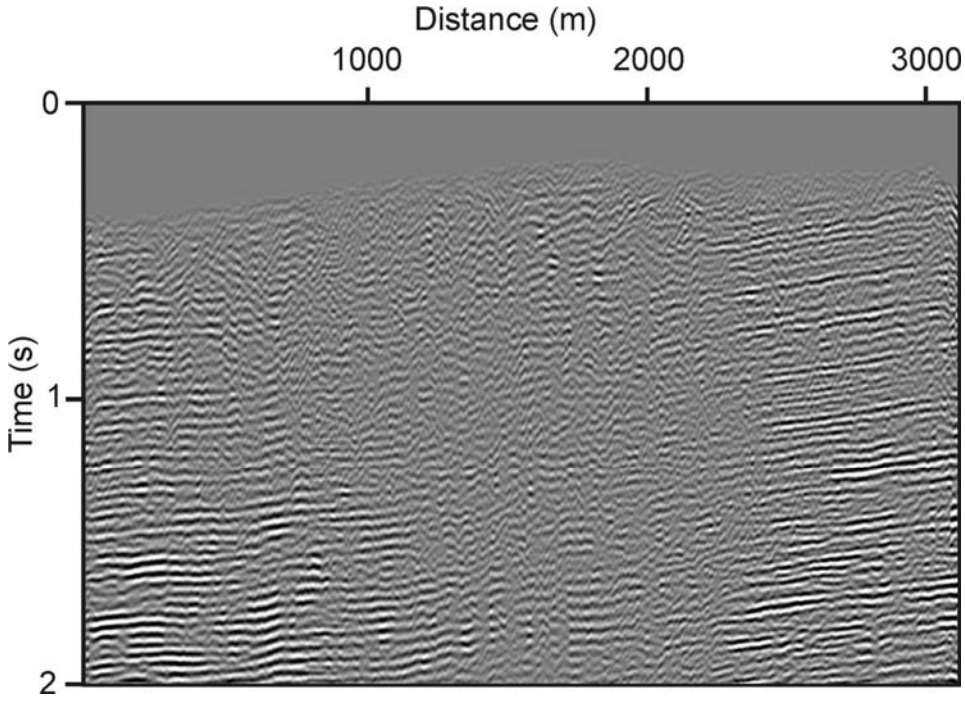

Figure 4.22. Common-Reflection-Surface (CRS) stack (input data is 2D from cross-line stacked 3D)

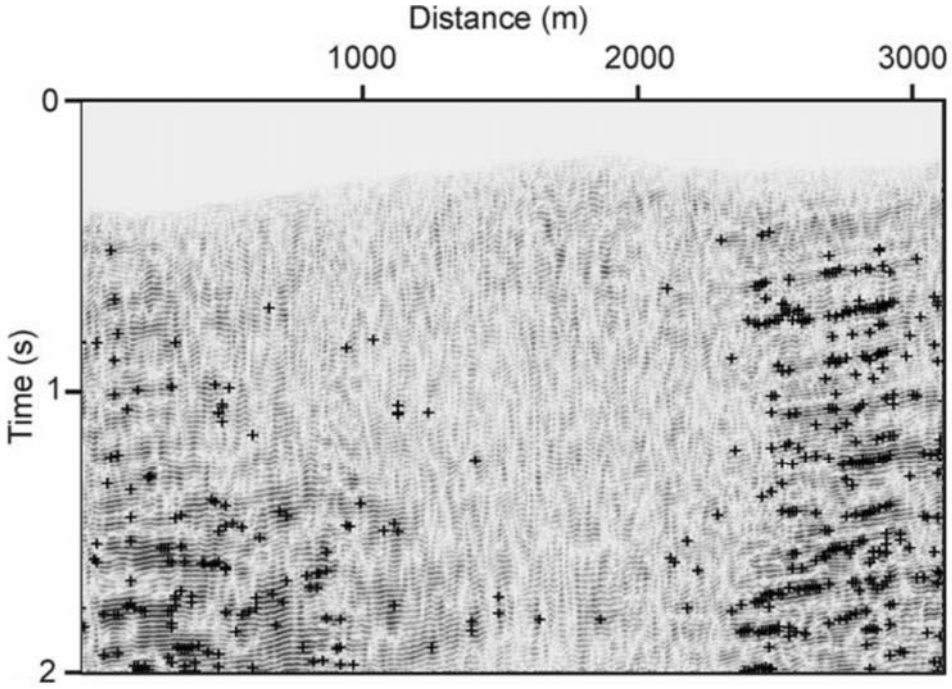

Figure 4.23. Automatically picked travel-times (input data is 2D from cross-line stacked 3D)

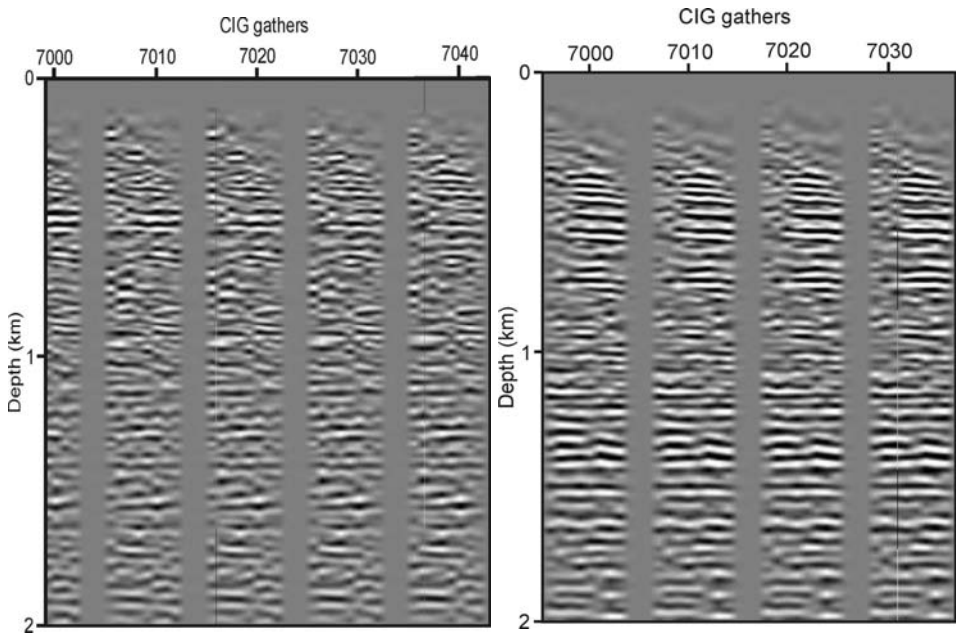

Figure 4.24. Common-Image-Gathers from 2D dataset (left) and 2D from crossline stacked 3D (right) on the right end of the profile

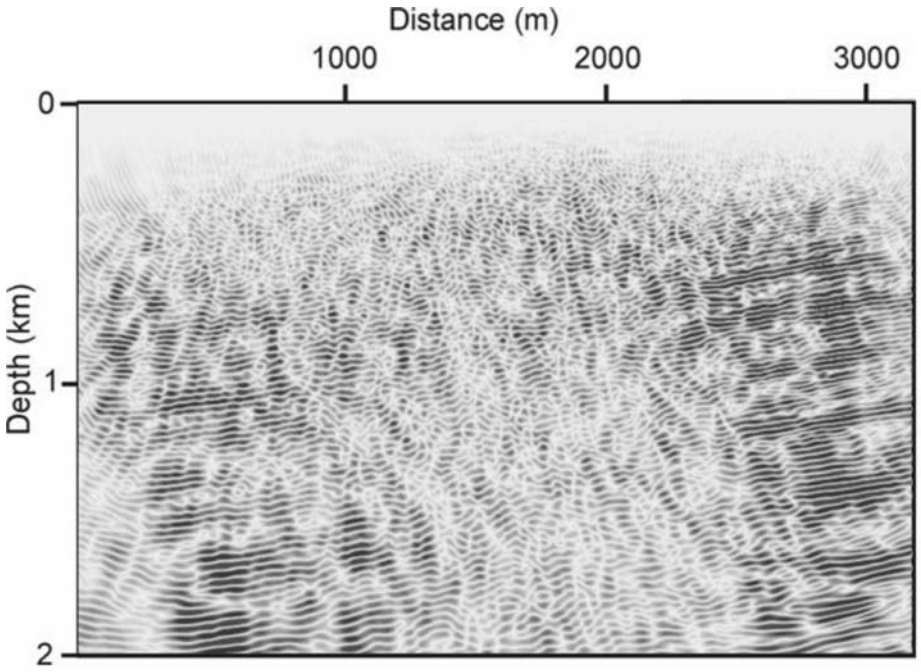

Figure 4.25. Pre-stack depth migrated stack with velocity model from travel-time inversion of picked events on CRS stack (input data is 2D from cross-line stacked 3D)

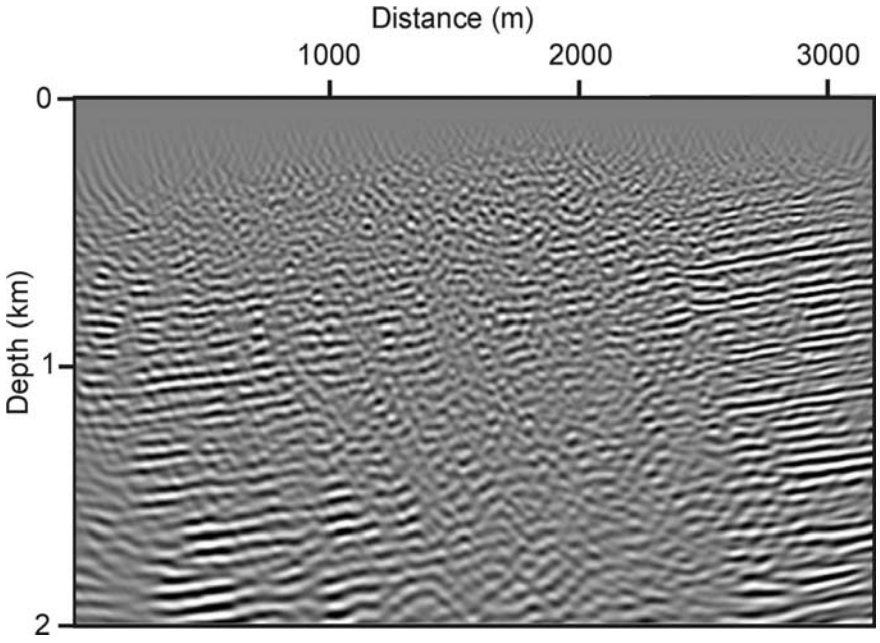

Figure 4.26. Pre-stack depth migrated section using the standard CMP-based imaging approach; the interval velocities are obtained from stacking velocities (input data is 2D from cross-line stacked 3D)

4.4 Conclusions

The post-stack stereotomography method was used to determine a more accurate 2D velocity model necessary for stacking and depth migration. Two different datasets were analyzed here. The first one is represented by the 2D single-sensor dataset, that contains the seismograms recorded on the central line of the receiver spread, and the second one is obtained after the cross-line summing of the partial-3D dataset. The results of two approaches are presented here, namely the CMP- and the CRS-stereotomography-based approaches. In case of 2D single-sensor dataset, the standard processing flow did not provide a

very good velocity model and a CMP section that shows us clear information about the geological structure of the studied area (only toward the edges of the profile). The low signal-to-noise ratio of the input data, maybe a consequence of the field conditions, can be responsible for the lack of the clear reflections on the central part of the profile. The reflectivity of this segment is somehow enhanced on the CRS stack. In addition, groups of reflections show a greater amplitude and continuity on the CRS stack compared with those seen on the CMP stack; other areas from the CRS stack show an interrupted continuity of the reflectors, while this continuity is clear on the standard processing result.

The output of the post-stack stereotomography shows an improved seismic section image, due to the improved velocity model quality. The accuracy of the 2D velocity model used for the pre-stack depth migration could be verified after a CIG gathers analysis; based on this, we can conclude that the velocity values determined especially toward the edges of the profile are good, which means that the depth migration worked well and we have a correct positioning in depth of the reflectors / geological interfaces.

The results of the CMP-based approach having as input the 2D from cross-line stacked 3D dataset show some improvements regarding the continuity and amplitude of the reflections seen on the CMP stack. Also, better signal-to-noise ratio is seen on the CRS stack. The accuracy of the 2D velocity model obtained by stereotomography is higher than that of the model obtained using 2D single-sensor records. This is supported by the image of the CIG-gathers obtained during the migration step. Therefore, the reflectors seen on the depth migrated section based on the 2D from cross-line stacked 3D dataset are positioned at the correct depth.

Chapter 5

The use of single sensors in tectonic interpretation[3]

5.1 Introduction

In this chapter, we will describe the results of a deep seismic reflection experiment (DACIA-PLAN). These results were obtained using a modern type of recorder that allowed easy deployment, the so-called "Texan" (a Ref Tek product). It is a light-weight recorder. These recorders were used in combination with single sensors. In this way an efficient way of getting data in hilly and mountainous areas was achieved.

It was decided to use single sensors for data acquisition in both deep

[3] This chapter is completely based on: Panea, I., Stephenson, R., Knapp, C., Mocanu, V., Drijkoningen, G., Matenco, L., Knapp, J., Prodehl, K., 2005. Near-vertical seismic reflection image using a novel acquisition technique across the Vrancea Zone and Focsani Basin, south-eastern Carpathians (Romania). Tectonophysics 410, p. 293 – 309.

seismic reflection and refraction projects. In the last decades, single sensors were often replaced by arrays of sensors during data acquisition, assuming that the use of arrays increases the signal-to-noise ratio of the recorded data. But, as we showed in the second chapter, the hard-wired arrays can deform or even annihilate the reflections in the presence of the local variations (generated, for example, by significant intra-array elevation statics, irregular array elements spacing, lateral variation of the near-surface velocities). This is an undesired effect that distorts the results of the interpretation. Therefore, in areas with rough topography, the use of single sensors is preferred, because it provides us higher quality data.

The DACIA-PLAN project was carried-out in August-September 2001, in Romania, at the same time with a deep regional refraction survey [VRANCEA2001; cf. *Hauser et al.* (2002)], as part of an international collaboration between the Netherlands Research Centre for Integrated Solid Earth Sciences (ISES, represented by the Vrije Universiteit, Amsterdam), the University of Bucharest, the Romanian National Institute for Earth Physics, the University of Karlsruhe, Germany, the University of South Carolina and the University of Texas at El Paso, USA.

The DACIA-PLAN seismic profile is about 140 km long and has a WNW-ESE orientation, crossing the seismically-active Vrancea zone of the south-eastern Carpathians orogenic belt and the foreland Focsani Basin (see Figure 5.1). The primary goal of DACIA-PLAN was the acquisition of a stacked deep seismic reflection image using a novel acquisition technique involving deployment of stand-alone seismic recorders ("Texans"/Ref Tek 125s).

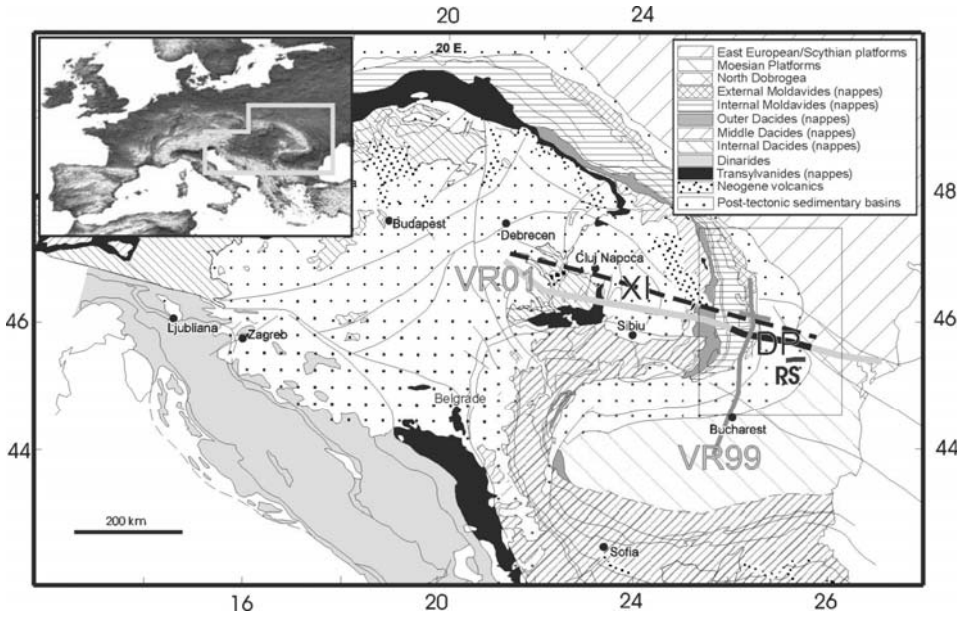

Figure 5.1. Tectonic map of the Carpathians/Dinarides/Pannonian basin system in south-eastern Europe [modified after *Sandulescu*, (1984)] showing the setting of the DACIA-PLAN profile (DP; thick black line) crossing the seismically active Vrancea zone of the south-eastern Carpathian Orogen and its foreland Focsani Basin, as well as the locations of deep refraction profiles XI [dashed black line; cf. *Rădulescu et al.* (1976)]; VR99 – VRANCEA99 [thin dark grey line; cf. *Hauser et al.* (2001)]; VR01 - VRANCEA2001 [thick grey line; *Hauser et al.* (2002)]; and deep reflection profile RS – Râmnicu-Sarat [*Răileanu and Diaconescu*, (1998)].

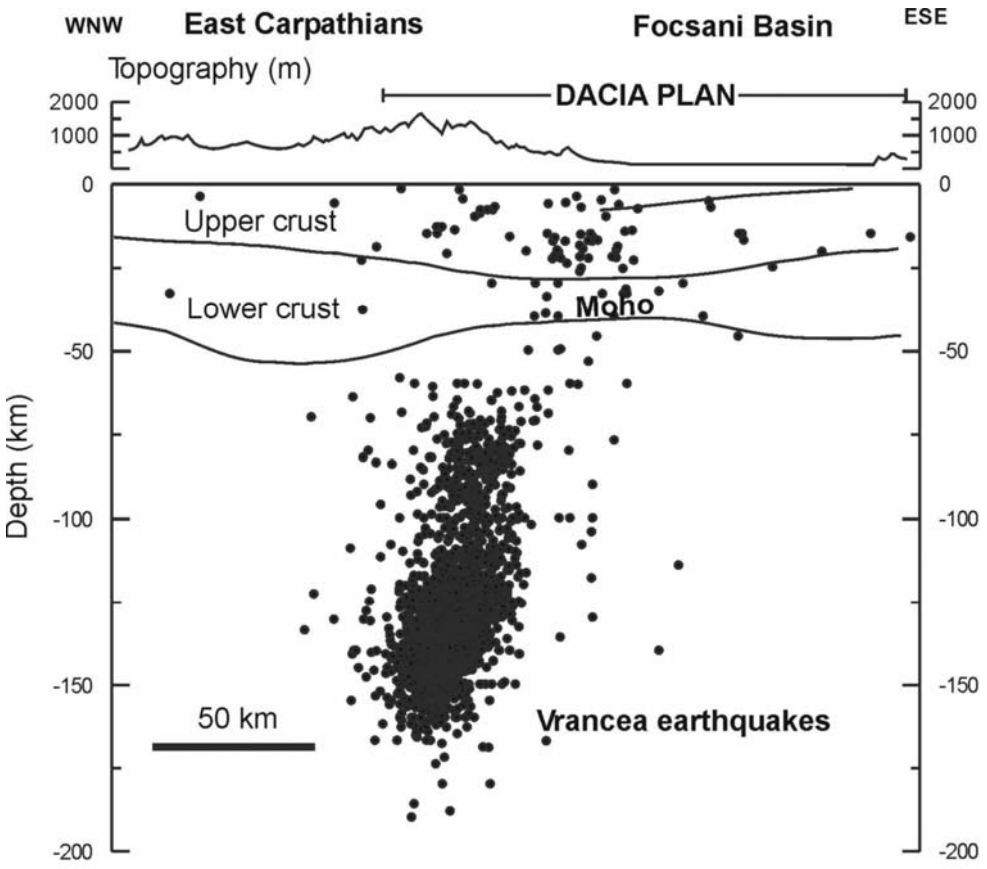

Figure 5.2. Lithosphere scale cross-section across the east Carpathians from *Rădulescu et al.* (1976). Solid dots represent earthquake hypocentres projected onto the plane of the cross-section within a corridor approx. 100 km wide. The location of the cross-section is shown in Figure 5.1 (profile XI). Also indicated are topography and the position of the DACIA-PLAN seismic profile. The dashed line in the foreland upper crust represents the approximate depth to the base of Neogene sediments in the Focsani Basin.

The Vrancea zone, which is directly crossed by the DACIA-PLAN seismic profile, is known for its intense and persistent seismic activity comprising crustal and intermediate earthquakes, with magnitudes smaller then

7.4. It has been traditionally divided into two vertical segments [e.g. *Enescu et al.* (1992)], which can be seen in Figure 5.2. The first one comprises the principal zone of intermediate earthquakes with hypocentres located between 60 and 200 km depth with an epicentral area of about 40 km by 80 km [*Oncescu and Bonjer* (1997)]. This volume forms a subvertical column and represents the main source for high energy earthquakes. The second segment, shifted east of the principal zone, is characterised by shallower earthquakes, with hypocentres between 20 and 60 km, and moderate magnitudes ($\leq$ 5.6), which are considered to be "crustal events". These two segments are separated between 40-70 km depth by an apparent seismic gap [*Fuchs et al.* (1979), *Oncescu and Bonjer*, (1997)]. Several hypotheses, implying various deep crustal geometries, have been proposed in order to explain the intermediate seismic activity in Vrancea zone [cf. *Kiratzi*, (1993), *Wenzel et al.* (1998), *Wenzel et al.* (2002), *Cloetingh et al.* (2004), *Sperner et al.* (2004), *Knapp et al.* (2005)]. *Knapp et al.* (2004) suggest that this area may uniquely offer evidence for the occurrence of active lithospheric delamination. *Chalot-Prat and Girbacea* (2000), based largely on geochemical characteristics of magmatic rocks, proposed a geodynamic model for the Mid-Miocene to Quaternary evolution of the south-eastern Carpathians in which an intra- mantle delamination process was initiated at the northern end of the East Carpathians at 9.4 Ma and the propagated laterally, normal to the strike of the delaminated slab, following the curvature of the Carpathian arc from north-west to south-east.

The study area has been investigated by a limited number of other deep seismic reflection and refraction surveys [e.g., *Enescu et al.* (1972), *Rădulescu et al.* (1976), *Răileanu et al.* (1994), *Răileanu and Diaconescu*, (1998)] as well as by extensive exploration scale reflection profiling in the foreland and easternmost thrust belt segments of the DACIA-PLAN profile [e.g., *Dicea*, (1995);

Ştefănescu et al., (2000), *Tărăpoancă et al.*, (2003)]. No seismic reflection profiling existed to the west of the Subcarpathians Nappe (see Figure 5.3). Deep Seismic Sounding profiles, including Profile XI, which is subparallel and nearly (partially) coincident with the DACIAPLAN profile (Figure 5.1), were acquired in this part of Romania during the years 1970-1974.

The broad crustal geometry shown in Figure 5.2 is derived from the XI profile, which was designed to record refracted arrivals from the sedimentary cover-basement horizon as well as the Conrad and Moho discontinuities. These data indicated a thickness of 12 km for the Focsani Basin adjacent to the Vrancea zone [*Rădulescu et al.* (1976)], consistent with modern seismic interpretations [*Tărăpoancă et al.* (2003)], and reveal lateral crustal heterogeneity across the Peceneaga-Camena and Capidava-Ovidiu faults (Figure 5.1). Among a series of experimental deep seismic reflection profiles of limited length acquired in the 1990s is the Râmnicu-Sarat profile (Figure 5.1) on the centre-eastern flank of the Focsani Basin.

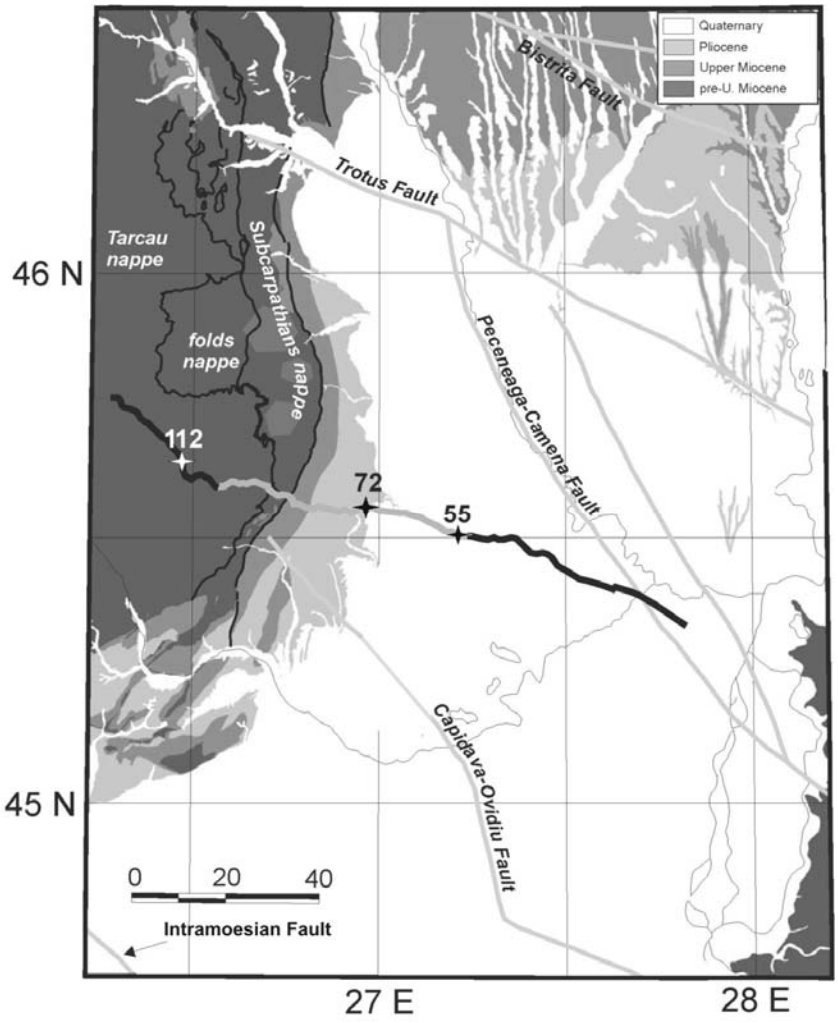

Figure 5.3. Geological map of the south-eastern Carpathians, from *Matenco* (2003), with the location of the DACIA-PLAN seismic survey with the separate recorder deployments 1-3 indicated (black/grey/black segments). Raw and processed versions of shot gathers for shots 55, 72, and 112 (white and black stars) are shown in subsequent figures and discussed in the text.

Two modern regional refraction/wide-angle surveys – VRANCEA99 and VRANCEA2001 (the latter acquired in conjunction with DACIA PLAN) – were carried out in order to study the crustal and uppermost mantle structure of the Vrancea zone and surroundings. The VRANCEA99 profile [*Hauser et al.* (2001)], 300 km long running in NNE-SSW direction (Figure 5.1), revealed an upper crust characterised by velocities of 5.9-6.2 km/s and a lower crust defined by a velocity range 6.7-7.0 km/s separated by an intra-crustal discontinuity between 18-31 km depth. The depth to the Moho increases from 38 km at the northern end of the profile to 41 km beneath the Vrancea zone (where it crosses the DACIA-PLAN profile). Towards the southern end the depth to the Moho decreases again to about 30 km [*Hauser et al.* (2001)]. The analysis of the VRANCEA2001 profile [*Hauser et al.* (2002), *Hauser et al.* (2007)] indicates a thickening of the sedimentary cover of the Focsani Basin, from east to west and a Moho depth under the Carpathians of about 40 km. The latter was based partly on the presence of a strong reflection from the crust-mantle boundary although, in general, seismic energy was highly attenuated in the Carpathian belt, related to structural complexity in the shallow geology. Tomographic travel-time inversion [*Hole* (1992)] of first arrivals along the VRANCEA2001 profile gave crustal velocities increasing up to 5.6 km/s above 10 km depth in the western part of line and similar velocities at depths less 20 km for central part [*Hauser et al.* (2002)]. A higher resolution velocity model of the upper crust from tomographic inversion of first arrival data along the DACIA-PLAN profile accurately images the transition from sediment to crystalline basement beneath the Focsani Basin, where industry seismic data are available for correlation, at depths down to about 10 km. Beneath the external Carpathians nappes, material with velocities > 5.5 km/s and with apparent structural heterogeneity lies at depths as shallow as 3-4 km, which is less than previously surmised on the basis of geological observations.

5.2 Geological setting

The south-eastern Carpathians consist of imbricated thrust sheets of different ages belonging to the Romanian segment of the Carpathian Orogen, a highly arcuate belt formed between the European and Apulian plates and related microplates during Alpine orogenesis [*Csontos et al.* (1992), *Girbacea and Frisch* (1998), *Nemcock et al.* (1998), *Matenco et al.* (2003)]. The present geometry of the south-east Carpathians is thought to be the result of the Tertiary collision between the Tisza-Dacia microcontinents (upper plate) and the East-European and Moesian Plates (senso largo – lower plate), possibly preceded by a roll-back of the subduction zone [*Royden* (1988), (1993)] and closure of a basin floored by oceanic lithosphere [*Csontos* (1995), *Linzer* (1996)]. It is assumed that plate convergence ceased during the Sarmatian, at about 10 Ma [*Săndulescu* (1988), *Roure et al.* (1993)]. The DACIA-PLAN profile has a WNW-ESE orientation and crosses both the external part of the south-eastern Carpathians nappe stack and its foreland units. The traversed nappe pile consists of the "external Moldavides system" [*Săndulescu* (1988)], which comprises thin skinned Lower Cretaceous-Miocene nappes, including the Tarcău, Marginal Folds, and Subcarpathian nappes (cf. Figure 5.3). To the south-east, the profile crosses the Moesian Platform and the westward extension of the North Dobrogean orogen, which are separated by the crustal scale Peceneaga-Camena Fault (cf. Figure 5.3).

The Tarcău and Marginal Folds nappes are made up mainly of Cretaceous marine basin sediments and Paleogene to Neogene flysch and other clastic sedimentary deposits. The Subcarpathian Nappe consists mainly of molasse, syn- and post-tectonic basin fill type sediments, deposited in a shallow marine to brackish environment. These nappes contain shales and sandstones with subordinate marls, limestones, tuffs, and conglomerates. In addition, the

Marginal Folds and Subcarpathian nappes contain lower and middle Miocene evaporitic formations including salt and gypsum [e.g., *Ştefănescu et al.* (2000)]. Previous geological and geophysical studies have suggested a thickness of about 8 km for the nappe stack in the area crossed by the DACIA-PLAN profile [e.g., *Matenco and Bertotti*, (2000)]. This was based on limited industry reflection seismic data and magnetotelluric surveys as well as geological cross-sections derived from the surface geology and some borehole data [*Cornea et al.* (1981), *Demetrescu* (1982), *Rădulescu et al.* (1981), (1984), (1988), *Enescu et al.* (1988), (1993), *Stănică et al.* (1986), *Răileanu et al.* (1994), *Matenco and Bertotti* (2000)]. However, the subsurface structure of the nappes is generally still under debate. As mentioned above, an upper crustal velocity model based on tomographic travel-time inversion of DACIA-PLAN first arrivals suggest that basement may be shallower than 8 km, perhaps less than 5 km beneath the westernmost segment of the DACIA-PLAN profile.

The Carpathian foredeep, developed in the front of the eastern and southern Carpathians is a syn- and post-colisional depression; it forms a wedge of clastic rocks (molasse-conglomerates, shale and sandstones) and evaporites that thickens from east to west, towards the thrust belt. Its width ranges from about 10 km in the northern part of the eastern Carpathians, to more than 100 km at the southern Carpathian belt (Figure 5.1). The thickest sediments are in the Focsani Basin, adjacent to the south-eastern Carpathians, where Pliocene-Miocene deposits are thought to be about 13 km thick [*Tărăpoancă et al.* (2003)]. However, the Focsani Basin displays unusual characteristics compared with typical foredeep basins, in that more than half of its sedimentary succession was deposited after the cessation of thrusting. In addition, the two basin flanks display a symmetrical, syncline-type geometry rather than that of a typical wedge-shape foredeep [see *Bertotti et al.* (2003), *Tărăpoancă et al.* (2003) for more detailed descriptions]. The contact zone between orogen and

foredeep in the vicinity of the DACIAPLAN profile is traditionally considered as a blind thrust, unconformably overlain by latest Miocene-Pliocene post-tectonic cover, this being indicative of the cessation of thrusting. However, the overall position and tilting of the sediments and particularly the eastward dip of the Upper Sarmatian unit suggest that the frontal contact between the orogen and the foredeep is a backthrust [*Matenco and Bertotti* (2000)]. As a result, in the frontal area a triangle zone is formed, with the backthrust compensating displacement on a basal sole thrust, which is called the Pericarpathian Fault [senso *Săndulescu* (1988)].

The structure of the Carpathian foreland in the area of the DACIA-PLAN profile is composed of two, internally complex, relatively stable areas, the East European/Scythian and Moesian platforms, separated by the North Dobrogea orogenic zone [Figure 5.1; further details in *Săndulescu and Visarion* (1988), *Visarion et al.* (1988)]. The East European and Scythian units are north of the Trotus Fault (Figure 5.3), characterised by a thick crust [40-45 km, *Enescu et al.* (1992)]. South of the Trotus and west of the Peceneaga-Camena faults (Figure 5.3), the Moesian block comprises a 35-40 km thick [*Rădulescu* (1988)] Precambrian-aged crustal unit [*Săndulescu* (1984)], buried under up to 13 km of middle Miocene to Quaternary sediments. The Peceneaga-Camena Fault separates the North Dobrogea and Moesian units, with an estimated decrease in the crustal thickness of the latter of 10 km, as indicated by DSS profile XI [*Rădulescu et al.* (1976)]. This fault has been repeatedly displaced during the late Alpine evolution of the overlying foredeep [e.g., *Tărăpoancă et al.* (2003)] and is currently active as part of a broad normal fault system with Moesia as the hanging-wall, with events occurring from its Black Sea extension all the way to the junction with the Trotus Fault system.

5.3 Seismic data – field acquisition, processing and results

DACIA-PLAN deep seismic reflection profile crosses the Vrancea zone in a WNW-ESE direction, with elevations along its 140 km length as high as about 1240 m, over the mountainous zone in the north-west, to only about 40 m in south-eastern part of profile. Recording was carried out in three independent but overlapping (5-10 km) segments, deployments 1, 2, and 3, from west to east (see Figure 5.3). Record length was 90 s with a sampling interval of 5 ms. Acquisition parameters are summarized in Table 5.1.

The seismic recorder used as single sensor in this project, namely "Texan" (see Figure 5.4) is a type of seismic recorder used in the seismology industry, in crustal scale reflection and refraction experiments, where hundreds of instruments are deployed over several hundred kilometers for a number of days. No connecting wires between Texans are required, making them very easy to deploy in areas with very complicated topography. Recordings are made based on pre-set time windows at different time sampling rates (e.g. 1000, 500, 250, 200, 125, 100, 50 and 25 samples per second). The Texan's data storage requirement for seismic applications is up to 21 MB.

Figure 5.4. Example of Texan (left) used for seismic data acquisition; the geophone is connected to this Texan using a wire (right)

The seismic source can be an explosive source (dynamite) and vibrator energy source. All the recorded data are downloaded, using an appropriate code, as SEG-Y files or, at an earlier stage, as SU files; SEG-Y and SU are types of seismic data formats.

A Texan recorder contain a low-noise differential input amplifier, 24-bit analog-to-digital convertor (ADC), solid-state data storage and batteries, all placed in a sealed aluminum case. Up to 15 Texans can be stored, setup and transported. For setup, the Texans are connected to a hub that provides power, connection to the host computer and time keeping signal from a GPS receiver. The hub provides several functions such as connections for 15 Texans, a connection to the USB host, one port for daisy-chaining additional hubs, routes the 130-GPS Receiver / Clock signals to each Texan for synchronizing internal time to UTC and precisely setting the internal oscillator frequency, supplies power to the Texans for setup and data. After setup, the Texans are deployed for recordings. An LED displays the operating conditions of the Texan (it should be green for good conditions). This feature clearly informs us if the battery voltage is sufficient, time is set, the acquisition program is loaded, and the unit is ready to acquire or is acquiring data. At the end of the recording campaign, the Texans are returned to the setup facility, retimed and data downloaded to the workstation for data processing.

After a first look at the recorded seismic data, in general, the upper 7 s of data contain higher frequencies and many more coherent reflections than data recorded at greater times. This is particularly true for deployment 3, in the foreland Focsani Basin, where signal-to-noise ratio is much better than for deployments 2 and 3 (see Figure 5.3). Processing, therefore, was carried out as two independent streams leading to two separate CDP stacks, one focused on the foreland sedimentary and upper crustal architecture utilizing the shallow (< 10 s) deployment 3 data only, and the other aimed at a whole crust/upper

mantle image along the entire DACIA-PLAN profile. Processing parameters are described in Table 5.2 and 5.3, and discussed separately in the sub-sections below.

5.3.1 Processing for the upper crust reflectivity ("partial-stack")

Data from deployment 3 (57 shots) were processed independently to form a "partial stack" that provides the best possible image of the architecture of the foreland Focsani Basin. The processing sequence is displayed in Table 5.2. Figure 5.5 shows a raw shot gather recorded at the westernmost end of deployment 3 (shot 55, see Figure 5.3 for location). Sedimentary interfaces within the Focsani Basin are responsible for the presence of a packet of clear reflected and refracted waves. The main coherent-noise is represented as a cone of events interpreted as surface waves (Rayleigh-type, "ground-roll"); these are characterized by a frequency interval ranging between 2-12 Hz and apparent velocities of 110-380 m/s. The seismic data were recorded in one static deployment of about 60 km length with shots "rolling along" rather than receivers. The maximum offsets lie in the range ~5-60 km depending on shot position within the receiver deployment. For further processing and stacking a maximum offset window - 10 to +10 km was adopted, this being constrained by the lateral extent of the observed reflection events. Elevation static corrections were applied after geometry set-up, trace editing (kill, reverse traces), and top muting (to remove refracted phases).

Item	**Parameter**
Seismic source	Dynamite (28 kg / shot)
Source spacing	~ 1 km
Shot depth	20 m
No. of shots / deployment	29 shots / deployment 1 47 shots / deployment 2 55 shots / deployment 3
Receivers	0Y0 4,5 Hz
Data acquisition system	1D Reftek – 125 s
Receiver spacing	~ 100 m
No. of receivers / deployment	334 / deployment 1 637 / deployment 2 632 / deployment 3
Record length	90 s
Sampling interval	5 ms
Length of profile	~ 140 km (WNW – ESE)

Table 5.1. Acquisition parameters of DACIA-PLAN profile

Processing sequence	**Parameters**
Input seismic data	10 s length
Geometry and static corrections	Replacement velocity 1600 m/s Final datum 100 m
Trace balacing	Time window = 5 s
Bandpass filter	Butterworth (4 – 24 Hz, 70 dB/octave)
f-x Deconvolution	Yes
Top muting	Removal refractions
Build a 2D velocity model	Refraction data and 1D velocity laws from boreholes
NMO correction	Yes
Stacking	Yes

Table 5.2. Partial-stack processing sequence

This was done assuming a replacement velocity of 1600 m/s (based on apparent velocities observed at small offsets) and a final datum of 100 m. The effect of a low-velocity weathered layer, given the observed apparent velocities, was assumed to be negligible. This was followed by a bandpass filter (Butterworth, 4-24 Hz with 70 dB/octave), based on an analysis of the characteristics of coherent events of interest, *f-x* deconvolution (to remove "ground roll") and, finally, trace balancing (5 s window). The result, for shot 55, is shown in Figure 5.6, where it can be compared to the raw shot gather (Figure 5.5).

What are presumably sedimentary horizons show good reflectivity, with clear and continuous events down to about 6 s; strong coherent events deeper than this are seen but are short and discontinuous (Figure 5.6). A rigorous velocity analysis proved problematic due to the lack of coherent events at depth. Nevertheless, a velocity model for normal move-out and stacking was built from a preliminary interpretation of the coincident refraction profile [i.e.,

VRANCEA 2001 – *Hauser et al.* (2002)] and from velocity data from nearby boreholes [e.g. *Tărăpoancă et al.* (2003)]. The final "partial stack" is shown in Figure 5.7a.

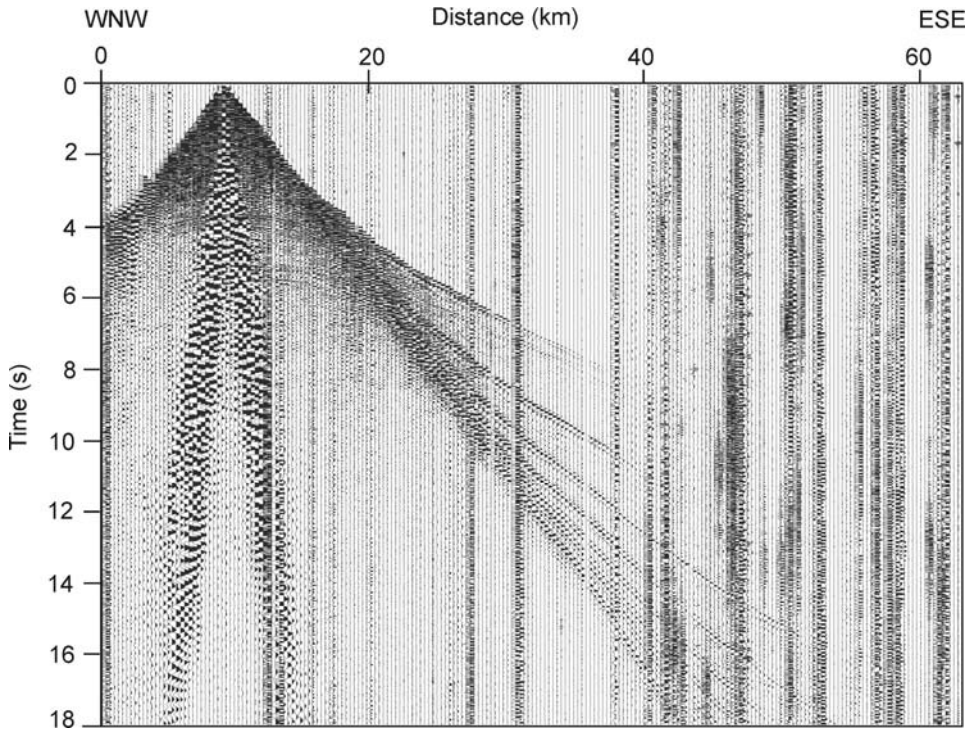

Figure 5.5. Raw shot gather for shot 55, recorded in the foredeep area (Focsani Basin) showing clear reflections down to 6 s.

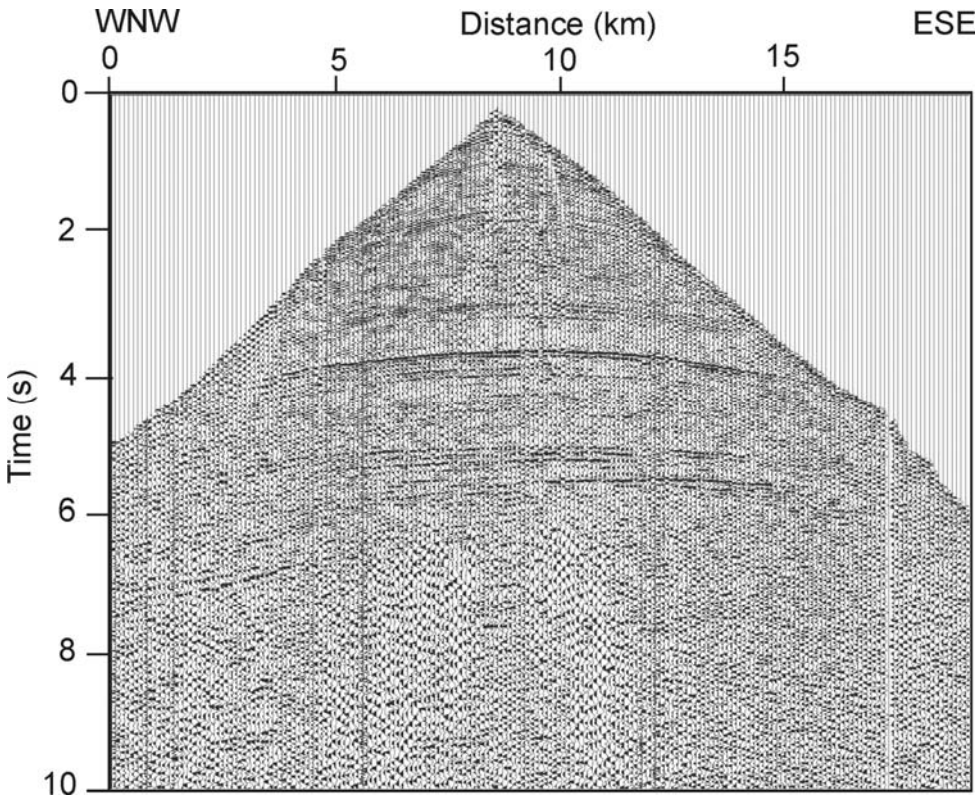

Figure 5.6. Processed shot gather (cf. Table 2) for shot 55, recorded in deployment 3 (Focsani Basin). The surface wave cone and refracted waves seen in Figure 5.5 are removed by filtering and top muting. Processing has been applied only to a -10 to +10 km offset window.

5.3.2 Interpretation of the "partial-stack"

The final "partial stack" is shown in Figure 5.7a and its interpretation in Figure 5.7b. Thickening of the highly reflective sedimentary succession (Focsani Basin) towards the Carpathian thrust front to the west is clearly seen. It increases from 2.2 s in the east to about 6 s in the west. Following the interpretation of *Tărăpoancă et al.* (2003) and *Tărăpoancă* (2004), which conform to interpretations from industry seismic profiling in the Carpathian foreland, the imaged sedimentary succession is Neogene and younger. Its oldest horizon, overlying pre-Tertiary basement, is thought to be of middle-late Miocene age (Badenian). The uppermost 2 s of the section, having a saw-tooth shape as an artifact of the processing stream, comprises Pliocene and Quaternary sediments. The top of the basement is locally visible (especially on the right half of the partial stack, see Figures 5.7ab); its interrupted discontinuity on the seismic section is interpreted to be an effect of a high level of fracturing and, according to *Răileanu et al.* (1998), the possible presence of local intrusive bodies (on the eastern half of deployment 3, see Figures 5.7ab).

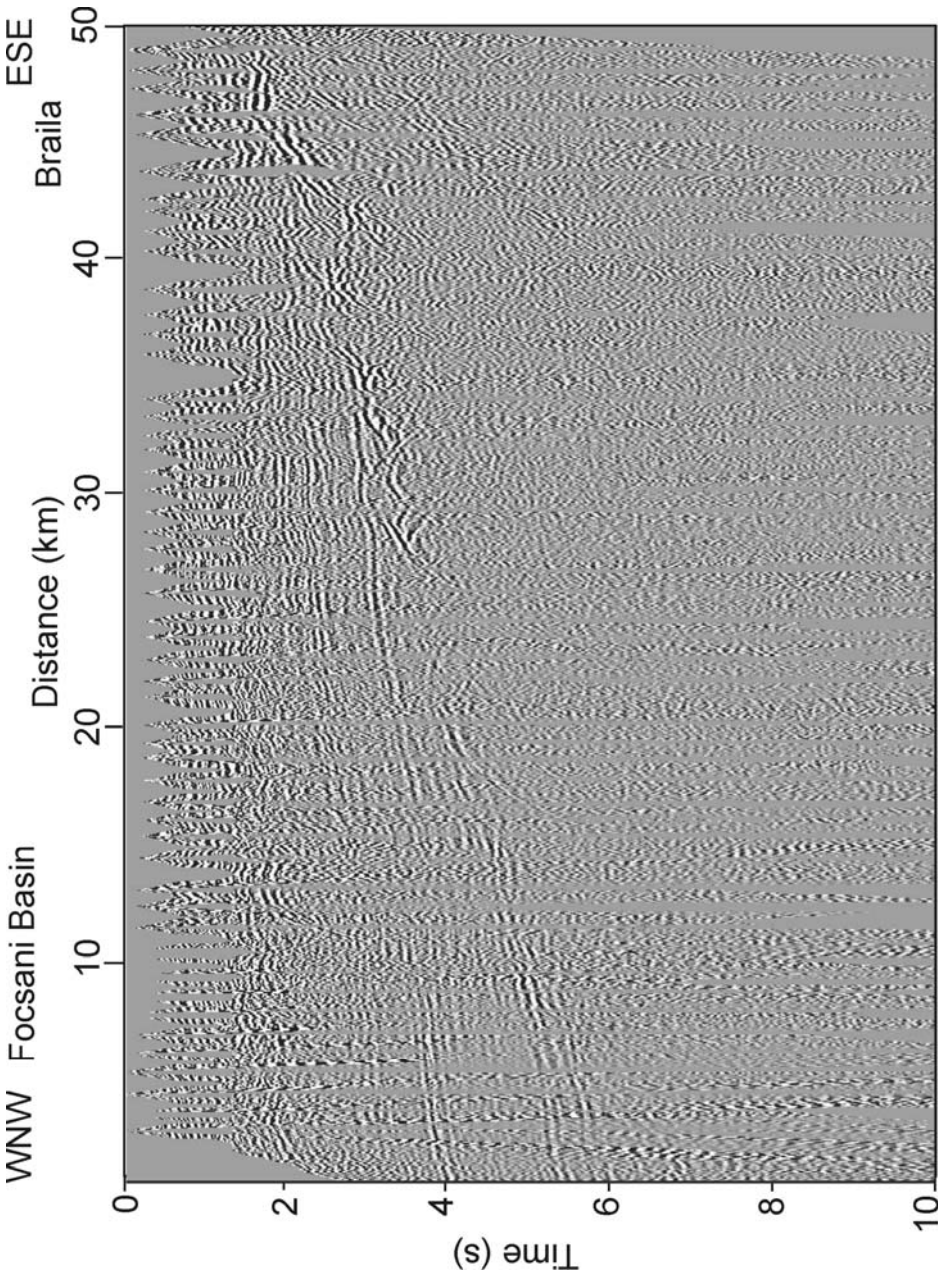

Figure 5.7a. Un-interpreted time seismic section obtained for the eastern segment (deployment 3) of DACIA-PLAN profile (processed to 10 s).

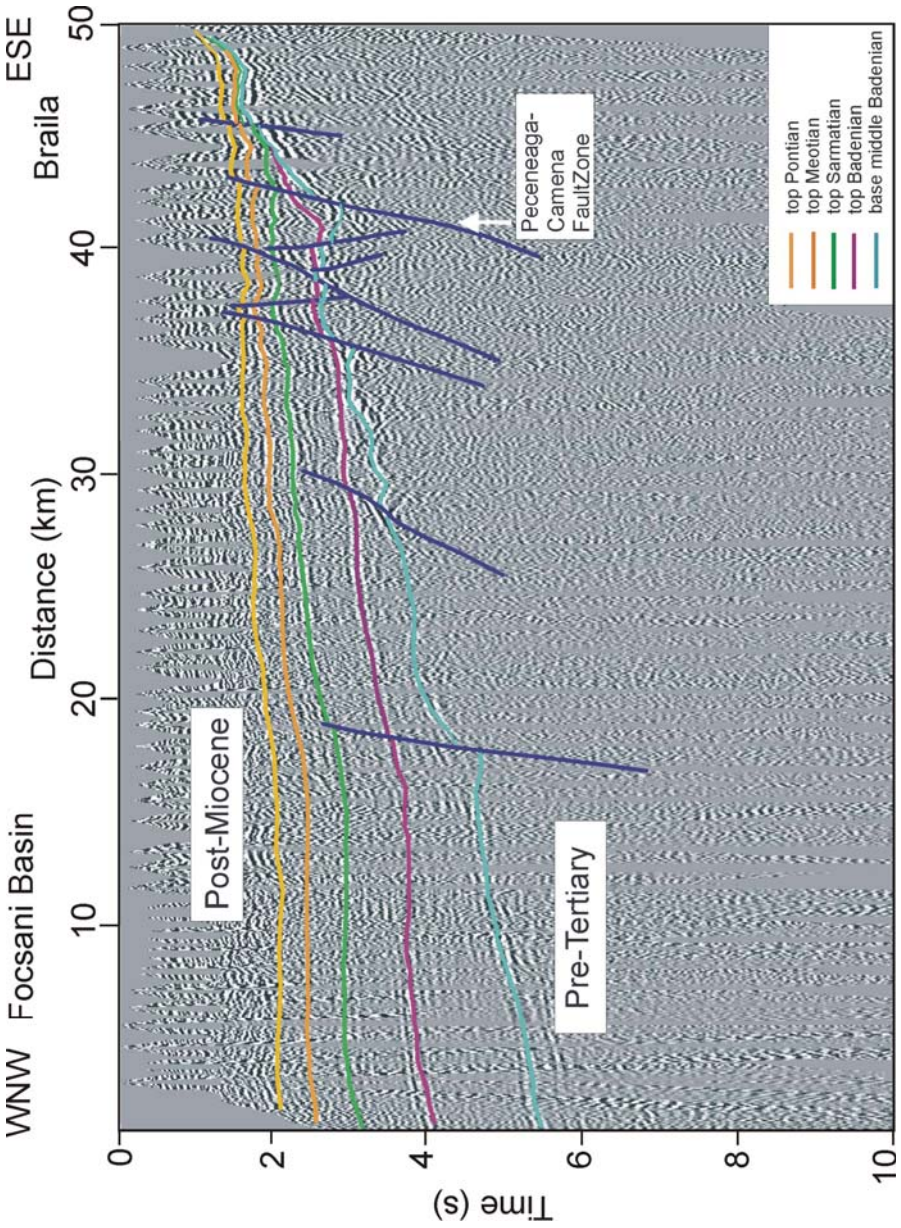

Figure 5.7b. Interpreted time seismic section obtained for the eastern segment (deployment 3) of DACIA PLAN profile (processed to 10 s). The interpretation of sedimentary horizons within the Focsani Basin conforms with *Tărăpoancă et al.* (2003).

5.3.3. Processing for lower crust reflectivity ("full-stack")

The purpose of the "full stack", based on 20 s of data for all three deployments, was to provide the best possible image of the crustal architecture of the external south-eastern Carpathians and its foreland.

The processing sequence is displayed in Table 5.3. Processing was carried out using "crooked line geometry" with an inline bin size of 50 m and a crossline size of 4500m, providing the maximum CDP coverage possible. The locations of bins compared to line geometry as well as CDP fold distribution are displayed in Figure 5.8. Maximum fold is about 60, in the central part of deployment 3. Thanks to the overlap of receiver deployments, the fold is of 5-10 between deployments. Receiver and shot statics were calculated using a datum of 0 m, a weathering layer velocity of 500 m/s, and a replacement velocity of 1600 m/s. Data quality is highly variable along the seismic line. Although reflected phases are well imaged from the sub-horizontal sedimentary deposits of the Focsani Basin in deployment 3 (cf. section 1.3.1), well resolved reflected phases are scarce to absent in shot gathers within the more geologically complicated sedimentary nappes of the south-eastern Carpathians.

Among the worst of the recorded shot gathers is 112, shown in Figure 5.9. Although first arrivals are easily seen out to an offset of about 15 km, no reflected phases can be identified, in part because of the wide surface wave cone. A time variant bandpass filter (8-24 Hz), true amplitude recovery, and trace balancing were applied but the surface wave cone was not significantly suppressed. Furthermore, because of the spatial aliasing intrinsic to the acquisition geometry, ground-roll was also not attenuated by (f, k_x)-domain filtering. Subsequent steps consisted of top-muting followed by *f-x* deconvolution and 2D spatial filtering, and the result for shot 112 is shown in Figure 5.10a. Figures 5.10b and 5.10c show filtered shot gathers (i.e., Table

5.3) for deployment 2 (shot 72; cf. Figure 5.3) and deployment 3 (shot 55; cf. Figure 5.3) respectively. Figure 5.10c differs from Figure 5.6 in terms of processing stream and processed record length.

Besides the intra-basinal reflectors in Figure 5.10c (section 3.1), there are clear coherent events within the basement to a depth of about 12 s. Some coherent energy can be seen on the filtered shot gather 72 between 6 – 11 s (see Figure 5.10b).

Processing sequence	**Parameters**
Input seismic data	20 sec length, resampled to 8 ms
Crooked line geometry	Bin size 50 x 4500 m
Static corrections	Replacement velocity 1600 m/s Final datum 0 m
Time variant scaling	Time windows: 0-1; 0.5-3; 2-5; 4-10; 9-15; 14-20; 19-30 s
True amplitude recovery	Trace window 10 s
Trace equalisation	Trace window 20 s
Time variant bandpass filter	Ormsby: 0-7s / 6-10-45-50; 6-12s / 4-8-40-45; 11-30 s / 4-6-15-20
Air blast attenuation	Velocity: 320 and 340 m/s
f-x deconvolution	Wiener Levinson filter
2D spatial filtering	2D Convolutional filter
Automatic gain control	Time window 2 s
Top muting	Removal of refracted waves
Velocity analysis	Yes
NMO corrections	Yes
Residual/fractional statics	Yes
Stacking	Yes

Table 5.3. Full-stack processing sequence

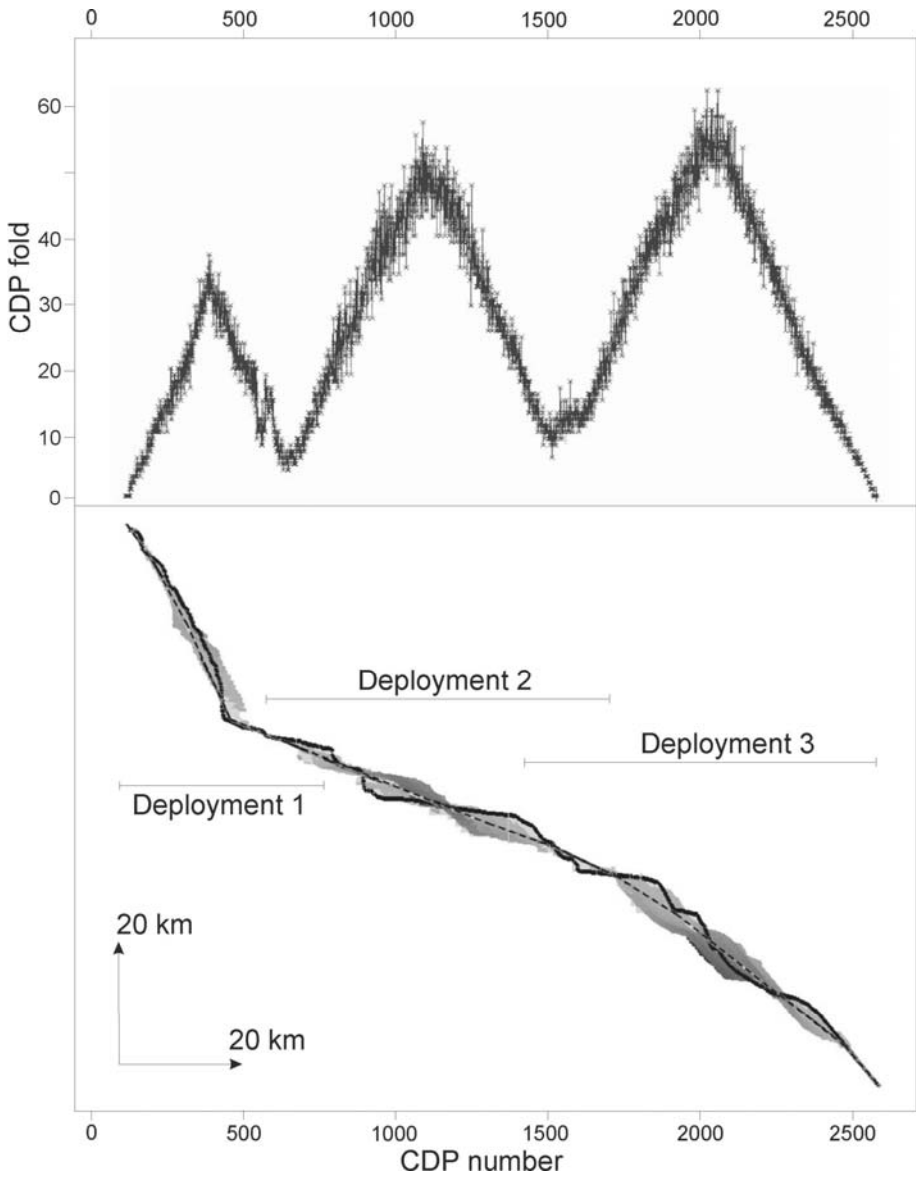

Figure 5.8. The (crooked) acquisition line (black line, comprising dots representing shotpoints), the trace of the "crooked line geometry" processed stack (dashed line; cross-line bin extends to 2250 m on either side), the number of CDPs per bin (the darker the grey the higher the number of CDPs), all in the lower panel, and CDP fold along the profile (upper panel).

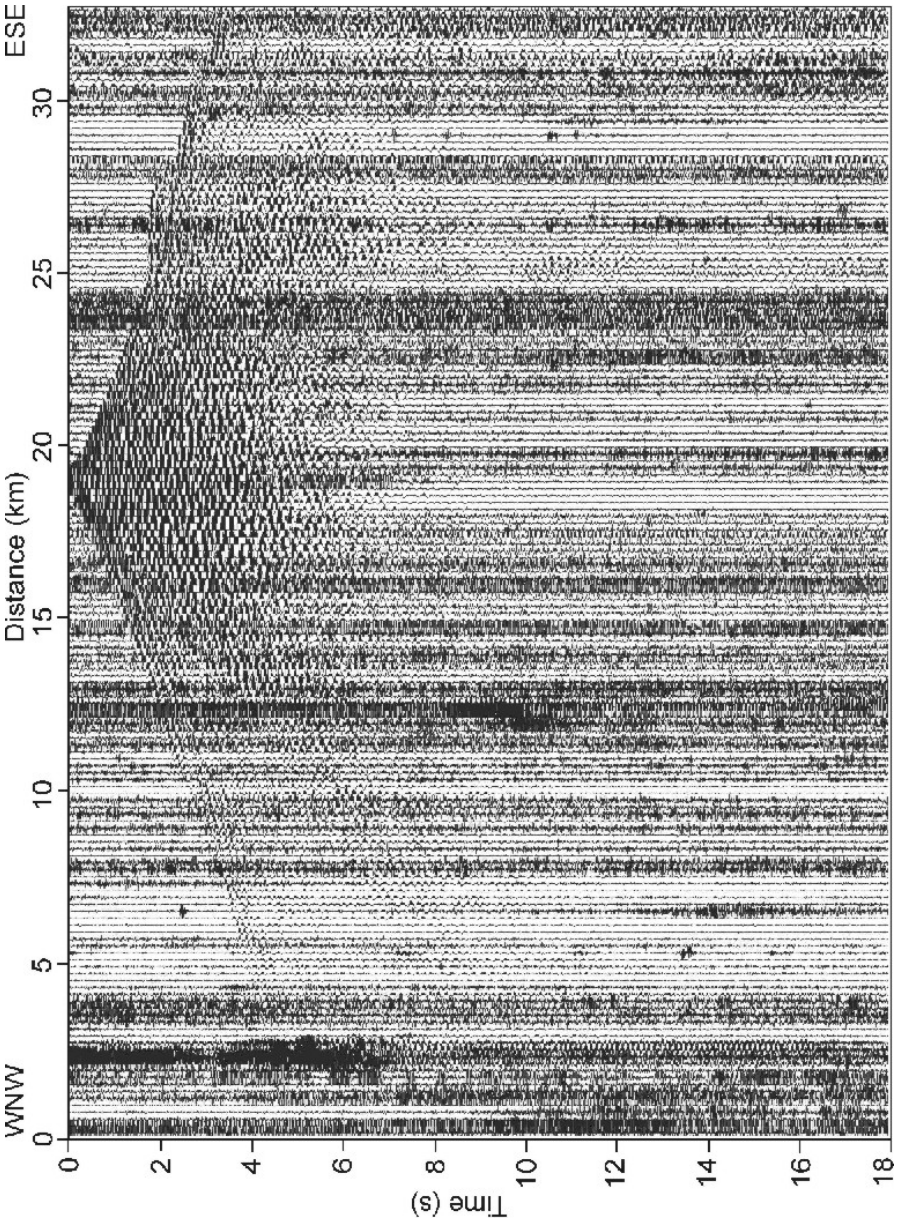

Figure 5.9. Raw shot gather for shot 112, recorded in deployment 1 (western part of DACIA PLAN, within the Vrancea zone), showing a large cone of surface waves and a lack of reflected phases.

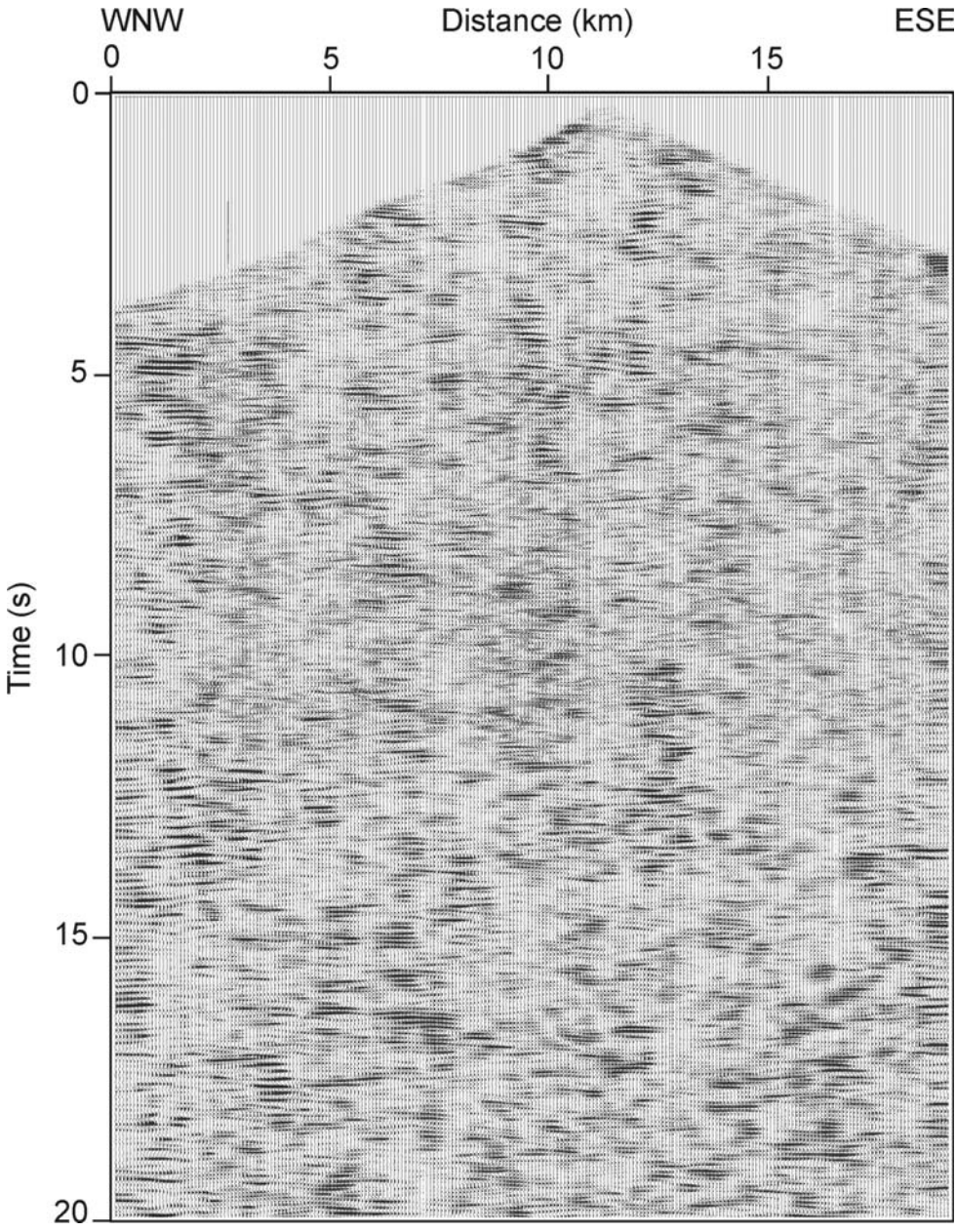

Figure 5.10a. Processed shot gather (cf. Table 5.3) for shot 112, recorded in deployment 1 (western part of DACIA PLAN, within the Vrancea zone).

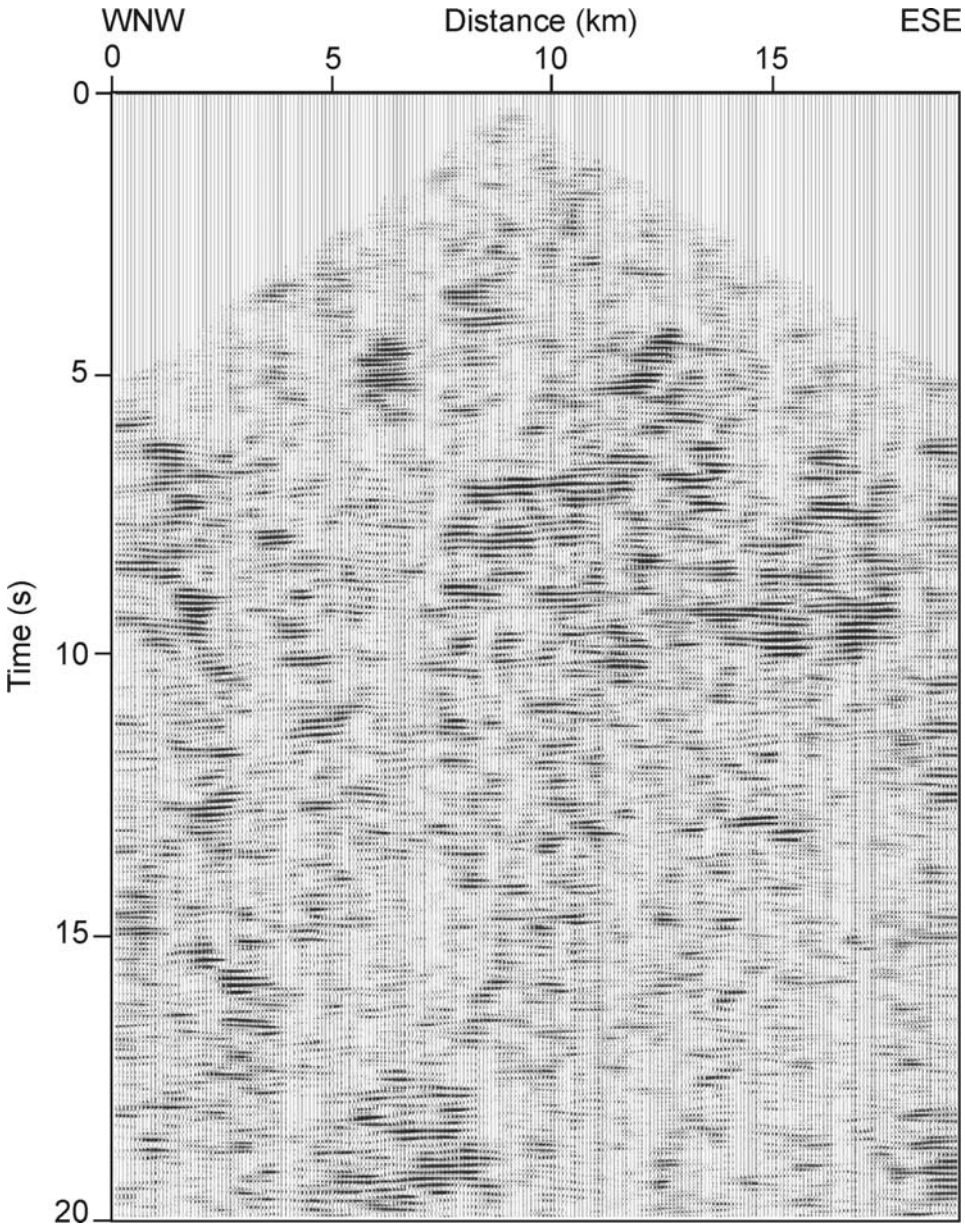

Figure 5.10b. Processed shot gather (cf. Table 5.3) for shot 72, recorded in deployment 2 (westernmost Focsani Basin).

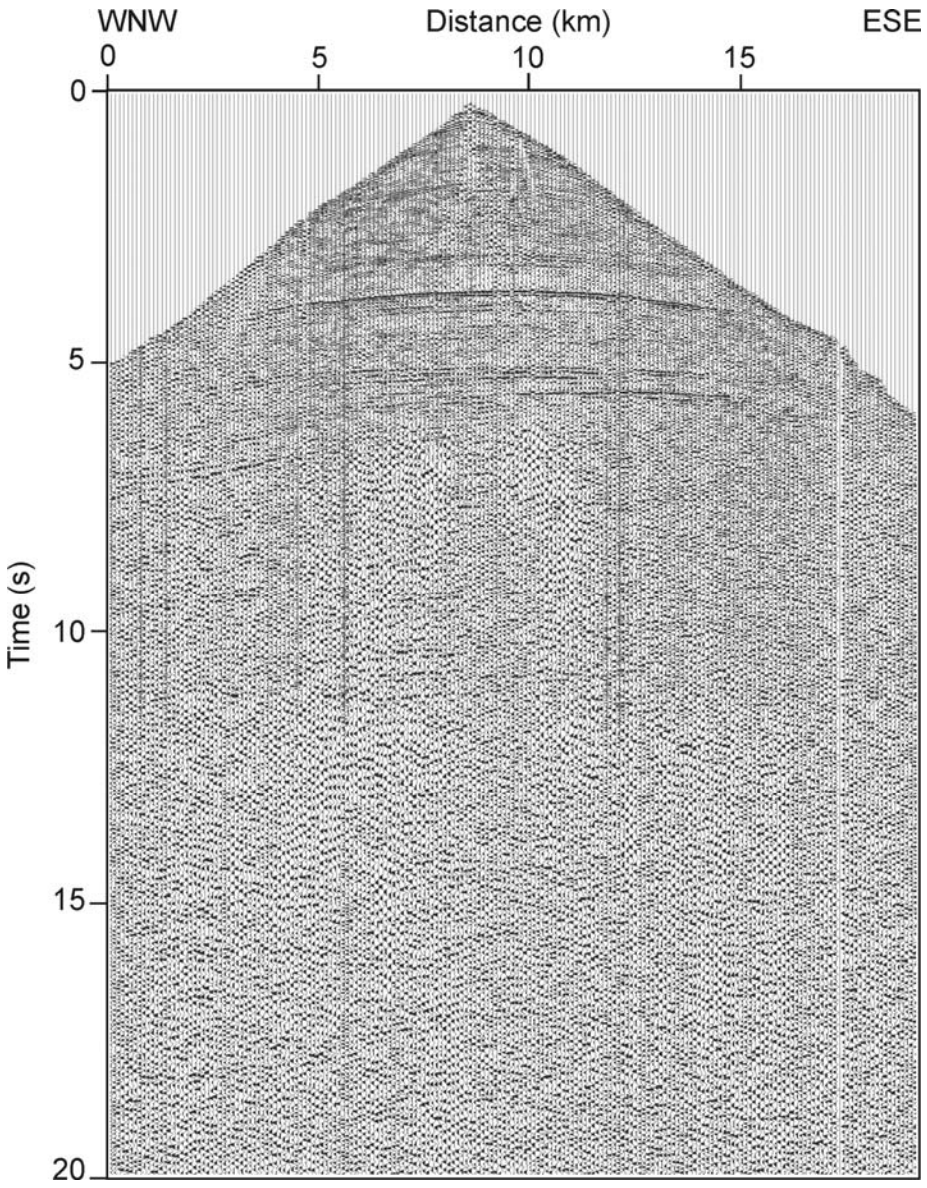

Figure 5.10c. Processed shot gather (cf. Table 5.3) for shot 55, recorded in deployment 3 (Focsani Basin).

The 2D velocity model, used for normal moveout correction and stacking, was built after a velocity analysis performed using the entire amount of processed seismic data, sorted after the common-midpoint. The analysis was correlated with two types of information, namely the results of the VRANCEA2001 data processing [*Hauser et al.* (2002)] and the 2D velocity model based on the inversion of the first arrivals picked on all seismic reflection records [*Bocin et al.* (2003)]. In the case of reflection data, the first arrivals are clear on distance intervals that vary from one record to another; they can be easily picked on large distance intervals, such as 10 – 45 km, in the case of seismic records from the plain area (see Figures 5.11ab), and smaller intervals, about 10 – 25 km, in the case of records from the mountainous area (see Figure 5.11c). The presence of very noisy or zero traces caused gaps in the travel-times readings (see Fig 5.11ac).

Data quality and the imaging of discrete coherent reflection events in the filtered shot gathers deteriorate from east to west (foreland basin to thrust belt) and the effect of this is seen in the final stacked DACIA-PLAN section in Figure 5.12a.

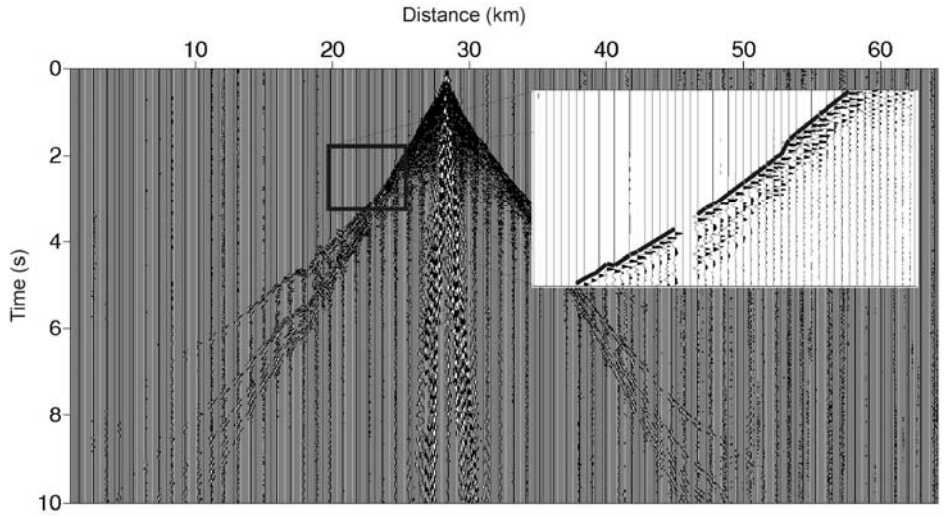

Figure 5.11a. Raw seismic record from the eastern part of DACIA PLAN profile (picked travel-time with solid black line)

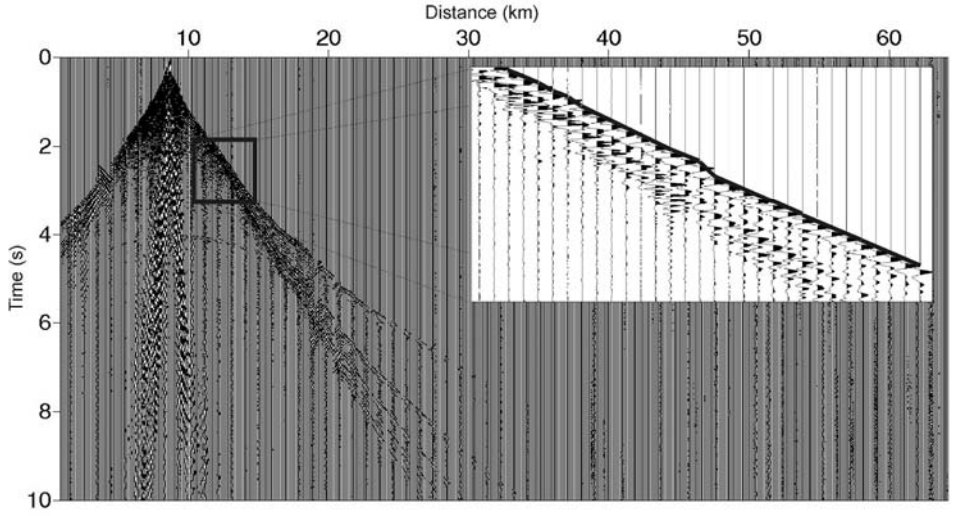

Figure 5.11b. Raw seismic record from the center part of DACIA PLAN profile (picked travel-time with solid black line)

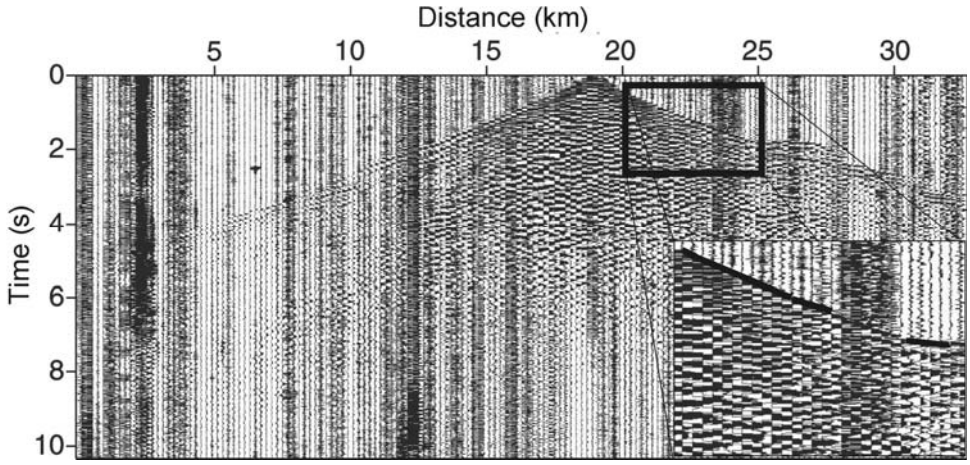

Figure 5.11c. Raw seismic record from the western part of DACIA PLAN profile (picked travel-time with solid black line)

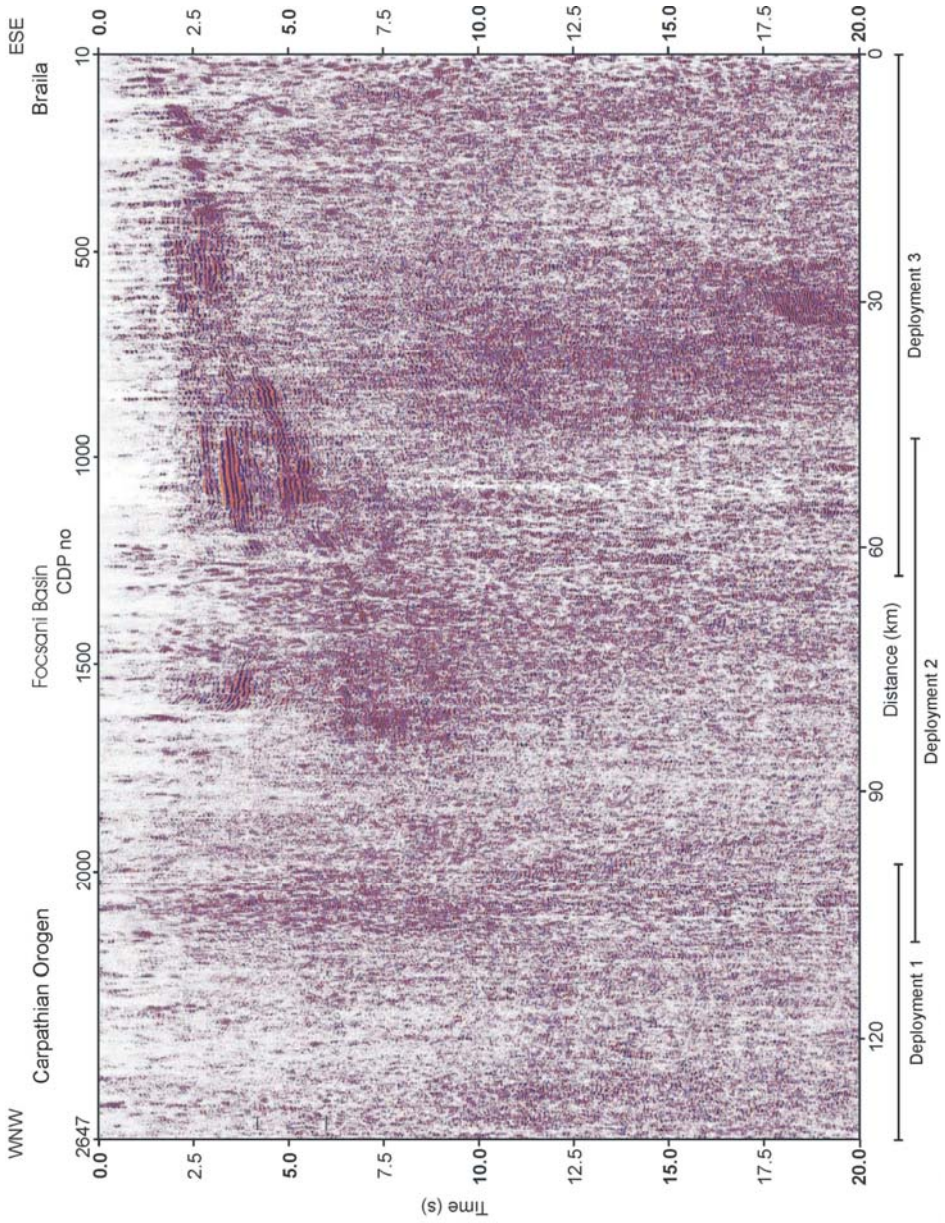

Figure 5.12a. Uninterpreted time seismic section for entire DACIA PLAN profile, up to 20 seconds.

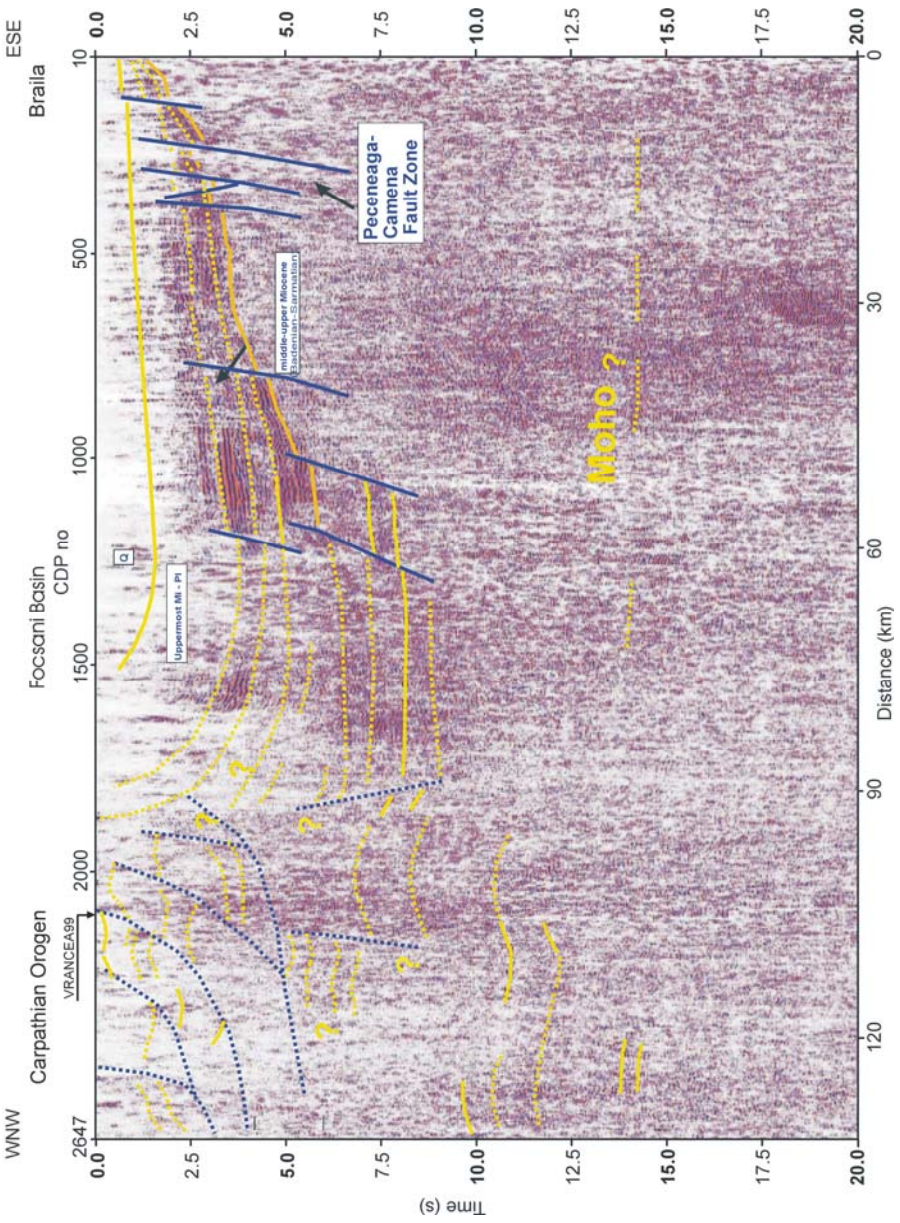

Figure 5.12b. Interpreted time seismic section for entire DACIA PLAN profile, up to 20 seconds

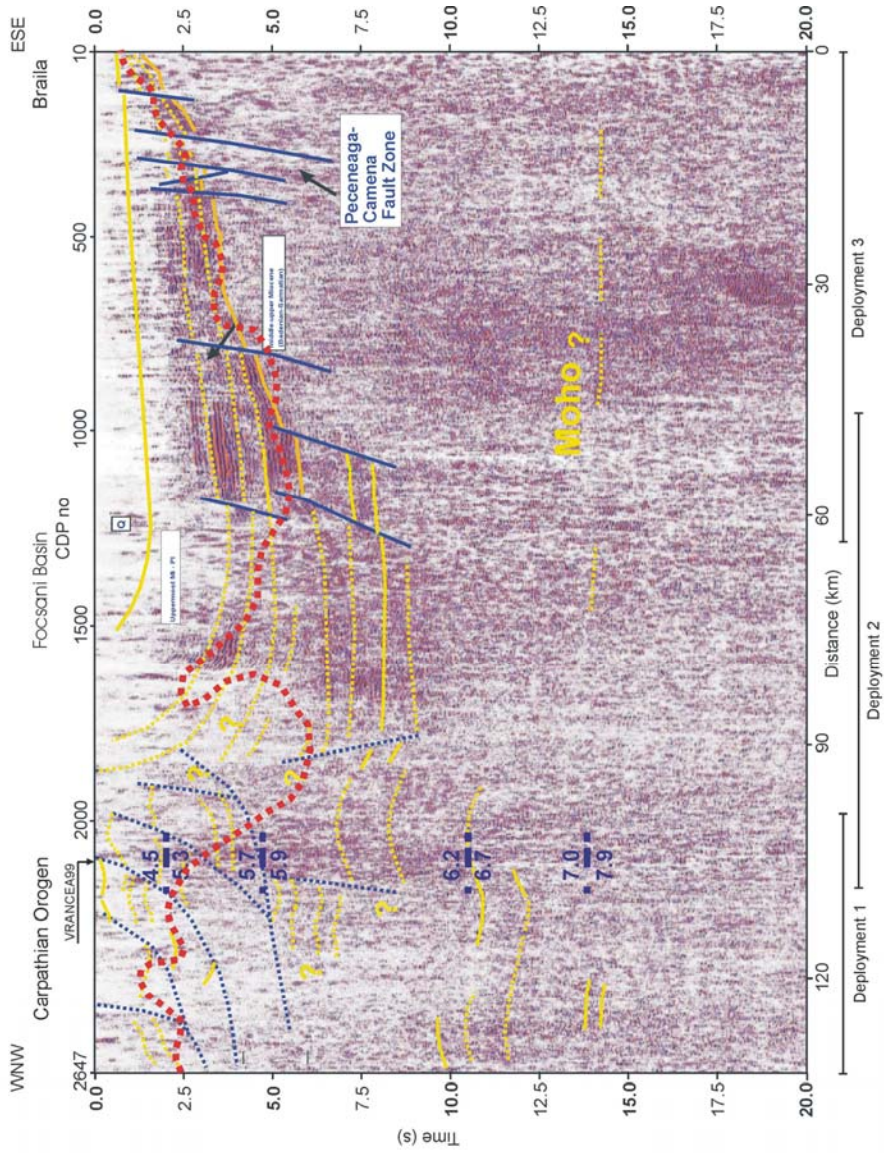

Figure 5.12c. Interpreted time seismic section for entire DACIA PLAN profile, up to 20 seconds; the thick dashed red line represents approximately the 5.0 km/s velocity contour in the tomography model of *Bocin et al.* (2005) and the dark blue velocity interfaces are from the crossing VRANCEA99 velocity model [*Hauser et al.* (2001)]. Yellow lines are geological interfaces and blue lines faults

5.3.4. Interpretation of the "full-stack"

The interpreted DACIA-PLAN full stack is shown in Figure 5.12b. It reveals, unambiguously given the mapped surface geology and shallow exploration seismic lines from the area [*Dicea* (1995), *Leever et al.* (2003), Forest Oil International, pers. comm.], the upwardly flexed western margin of the basin. The fault systems known to offset the base of the basin in its eastern extreme, correlated with the Peceneaga-Camena Fault, are generally thought to be of crustal-scale [e.g. *Rădulescu et al.* (1976)] but the DACIA-PLAN data do not display any evidence that can support or, for that matter, refute this.

There is clear evidence in the DACIA-PLAN full stack for sedimentary successions beneath the Focsani Basin west of approximately common depth point (CDP) no. 1000, in the time range 4-8 s, laterally adjacent to transparent crust further east. The velocity within this sedimentary package ranges from 5.2 to 5.8 km/s, based on the VRANCEA2001 model [cf. Figure 5.3, *Hauser et al*. (2002) and Figure 11, *Hauser et al.* (2007), DACIA-PLAN is located approximately between shotpoints U and R]. Accordingly, the total thickness of the package is more 10 km, lying roughly in the depth range 10-20 km (see also Figure 5.13). The inferred velocities are not atypical of clastic sediments buried to such depths. An analogous unit is the thick sedimentary succession, unambiguously identified in deep seismic reflection data [*Cook et al.* (1987)] and having velocities 5.8-5.9 km/s determined from coincident seismic refraction profiling [*Stephenson et al.* (1994)] that is associated with a fair degree of certainty (from the regional geology) with a thick clastic wedge deposited on a Proterozoic or Palaeozoic continental margin.

The eastern margin of this sub-Focsani sedimentary basin appears to be controlled by a series of normal faults, suggesting that it is of extensional

origin. The western margin of this sequence is not clearly imaged. However, there is a clear evidence, given the reflectivity pattern, that sediments extend to the west beneath at least the easternmost part of the Carpathian nappes (west of ~CDP no. 1800), although the image is more ambiguous than further east and structures evidently more complex.

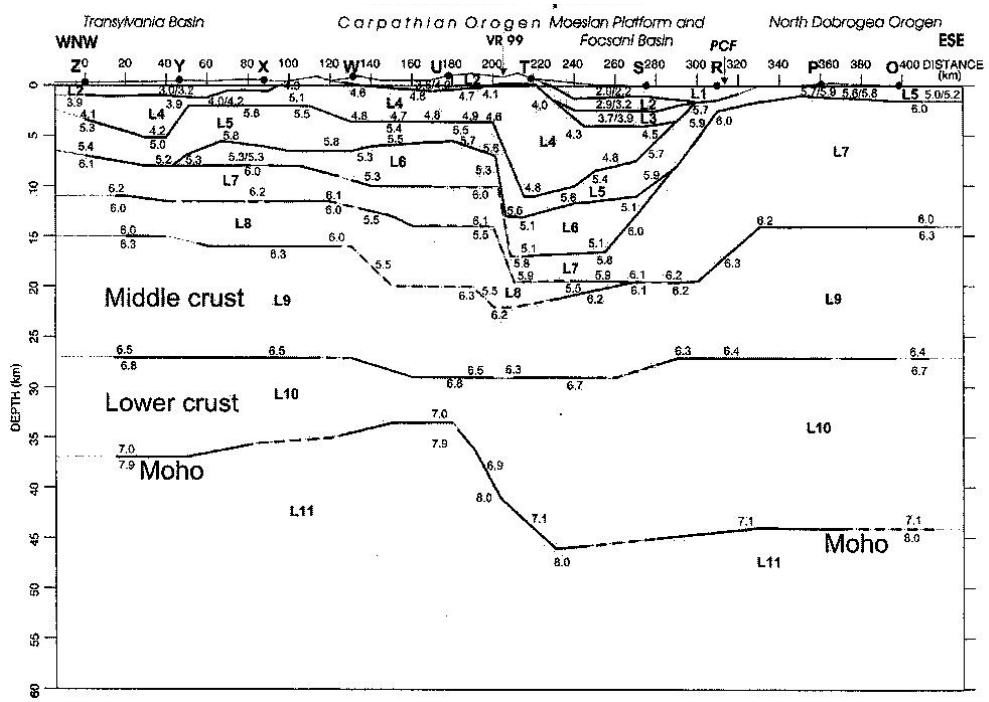

Figure 5.13 VRANCEA2001-2D velocity-depth model. Labelled dots at the top of the model indicate the shot points from O to Z and the decimal numbers show the P-wave velocities in km/s. The VR99 arrow marks the intersection with the VRANCEA'99 seismic line and PCF the Peceneaga-Camena Fault. L1 to L11 indicate the seismic layers used in the interpretation. Thick solid lines indicate areas which are well constrained by reflections and/or refractions. Dashed lines indicate less well constrained areas, while thin lines are extrapolations [after *Hauser et al.* (2007)].

The geometry of the normal faults on the eastern margin of the rift basin (the shallow expression of two of them is seen in the partial stack – Figure 5.7b) suggests that sediments at the base of the Focsani Basin in this area, generally interpreted as middle Miocene in age [*Tărăpoancă et al.* (2003), cf. Figure 5.7b], could be older, belonging in fact to the underlying "rift" basin sequence. This is supported, although not unambiguously, by velocities derived from the tomographic inversion of the DACIA-PLAN first-arrival data, with the thick dashed red line in Figure 5.12c representing approximately the 4.5 km/s velocity contour in the tomography model [*Bocin et al.* (2005)]. The actual age of the inferred extensional basin cannot be determined. *Tărăpoancă et al.* (2003) have reported smaller, fault-bounded sedimentary basins in the adjacent foreland interpreted to be of Badenian age. Thus, the sediments in the rift basin seen in Figure 5.12b could be as young as this if this age is correct and if there is a correlation. Otherwise, the Moesian crust underlying this basin is of Precambrian age [e.g., *Visarion et al.* (1988)] and was in an extensional tectonic environment in the Late Palaeozoic-Triassic [e.g., *Rabagia and Tărăpoancă* (1999), *Pharaoh* (1999)] as well as during Late Jurassic-Cretaceous times, the latter being associated with the opening of the western Black Sea [*Dinu et al.* (2005)].

Of great significance is that the secondary zone of Vrancea zone seismicity, characterised by crustal events of magnitude less than 5.6 [e.g. *Enescu et al.* (1992)], coincides in position and depth with the deeper parts of the rift-like basin imaged on the DACIA-PLAN profile. In this respect, it seems likely that the generally weaker rheology of sedimentary rocks compared to crystalline crustal rocks as well as pre-existing structures in the crust associated with rifting play a role in localising seismicity in this area. The inferred extensional basin is likely two-dimensional (i.e., has a clear structural trend in plan view), which cannot be determined from the seismic profile, however,

whereas the seismicity with which it is associated is laterally constrained. This implies that the source of the stresses giving rise to earthquakes is confined to this particular area, in the bending zone of the south-eastern Carpathians, and, therefore, probably related to whatever the sources of the deeper Vrancea earthquakes are.

Few laterally coherent events are discernible on the north-westernmost part of the DACIAPLAN stack, beneath the south-eastern Carpathians external nappes. There are hints of sub-horizontal, gently folded, horizons in the uppermost 2.5 s and the thrust faults that are shown on Figure 5.12b are inferred from these horizons accordingly. However, it is clear that the existence of such structures is supported more by the geological interpretation of this area – from surface exposures and nearby shallow subsurface – than from the seismic section. The tomography velocity model indicates velocities greater than 4.5 km/s below about 2-2.5 s suggesting that the materials involved in thrusting beneath this depth consist of sediments older than Tertiary, previously more deeply buried than at present and representing "basement" in the context of Carpathian thrusting [*Bocin et al.* (2005)]. It is also important to note that the thrusting in this area, on the inferred thrust faults, predated the flexural couple (or "buckle") proposed to explain the rapid uplift of the overlying Vrancea zone [e.g. *Sanders et al.* (1999)] contemporaneous with the rapid Neogene subsidence of the Focsani Basin [cf. *Bertotti et al.* (2003)].

The VRANCEA99 crustal refraction profile crosses the DACIA-PLAN profile at approximately CDP 2100. The main velocity discontinuities inferred in the VRANCEA99 model [*Hauser et al.* (2001)] have been converted to two-way travel-times and plotted on Figure 5.12c as short dashed blue line. Associated velocities (in km/s) above and below each discontinuity are also shown. The shallowest horizon conforms to the DACIA-PLAN tomography model in that high velocities greater than 5.0 km/s occur at relatively shallow depths beneath

the Vrancea zone external nappes [thick red line in Figure 5.12c; travel-time converted 5.0 km/s horizon from *Bocin et al.* (2005)]. The next horizon, which is not characterised by a large velocity contrast, occurs approximately at the inferred depth of nappe detachment. The crustal unit beneath this discontinuity, in the depth range 10-12 to about 30 km (10.5 s in Figure 5.12c) and having velocities in the range 5.9-6.2 km/s [*Hauser et al.* (2001)], shows evidence of sedimentary layering, possibly correlating with sediments within the buried rift-like basin to the east, as mentioned above.

The deeper layering structure underlying the western flank of the Focsani Basin and southeastern Carpathian nappes (5-10 s in the CDP range 1300-2100) are flat-lying compared to the upwardly flexed Focsani margin. It follows that these units are detached from the overlying "buckle" structure involved in Neogene and recent uplift of the Vrancea zone and down warping of the adjacent Focsani Basin. Accordingly, it is clear that the Neogene Vrancea-Focsani "buckle" involves upper crustal units only and is not a crustal buckle as proposed by *Bertotti et al.* (2003). This is also in agreement with its wavelength. The implication is that material must be entering the section beneath the Vrancea zone at a depth of about 5 s (10-12 km) in order to drive and fill the volume beneath the uplift zone. Unfortunately nothing definitive can be said from the DACIA-PLAN image in this regard but the candidates are intracrustal thrust slices, either from the northwest or from out of the plane, or intruded igneous magmas. In the latter case, there is no supporting bright spot obvious in the seismic data. It is interesting to note, in this regard, the subsidiary antiformal structures beneath 5 s in the CDP range 1800-2200. However, it is not impossible that these are pull-ups related to higher velocities overlying them in the upper few seconds.

Several poorly displayed reflections occur at 13.5-14 s beneath the external nappe zone at the western end of the DACIA-PLAN profile, which

may be an indication of the Moho, which lies at ~40 km (~13.5 sec), above upper mantle with a moderately low velocity of 7.9 km/sec, according to the refraction data [*Hauser et al.* (2001)]. Similarly, the Moho is poorly inferred from the DACIA-PLAN image to lie at about 14 s further to the east, where it is in part obliterated by a zone of artificial "ringiness" that extends through the crust and upper mantle in the CDP range 500-1000. It is thought that this may relate to laterally dispersed and reflected energy from the Peceneaga-Camena Fault. *Răileanu and Diaconescu* (1998) interpreted the Moho at 15 sec, although also poorly displayed, on the nearby Râmnicu-Sarat seismic profile (Figure 5.1). Preliminary analysis of the VRANCEA2001 refraction data (coincident with DACIA-PLAN) is also consistent with a Moho beneath the Carpathian foreland in this area at 14-15 s [42 km; *Hauser et al.* (2002), (2003)].

Crystalline crust is evidently significantly thinned in the area beneath the buried extensional basin; it is represented by not more than 5 s, which, at a velocity of 6.5 km/s or more [*Hauser et al.* (2001)], is considerably less than 20 km. Thin crust beneath a rift basin is not atypical, as a result of crustal stretching during extension, although the degree of thinning observed is fairly extreme. Other possible mechanisms include migration of the Moho to shallower levels as a result of (ultra)mafic intrusion in the lower crust, increasing its density and velocity to upper mantle levels, and delamination of the lower crust. With respect to the former, the upper mantle velocity recorded on VRANCEA99 is fairly low – 7.9 km/s [*Hauser et al.* (2001)] – and this could be seen as supporting evidence. With respect to the latter, crustal delamination is among a number of processes that have been proposed to be involved in providing the locus of the deeper seismicity recorded in the Vrancea Zone [cf. *Wenzel et al.* (2002), *Cloetingh et al.* (2004), *Knapp et al.* (2005)]. The main earthquake zone lies below the DACIA-PLAN image seen in

Figure 5.12 (i.e., deeper than 20 sec, CDPs greater than 2000). Nothing notable was recorded from those depths in this area. However, it is likely significant that the crystalline crust along the DACIA-PLAN profile, directly above the earthquake zone and to the east, appears to be very thin, represented only by what is probably some kilometers of upper crust with overlying sedimentary successions.

5.4. Conclusions

The DACIA-PLAN seismic profile was a part of a multidisciplinary programme designed to study one of the most seismically active areas of Europe, namely the Vrancea zone. Its goal was to elucidate the deep structure of the external Carpathians nappes and the architecture of Tertiary / Quaternary basins developed within and adjacent to the Vrancea zone, including the Focsani Basin. Two seismic sections have been obtained. The first, called the "partial-stack", represents the results of shallow data processing and images the broad internal architecture of the sedimentary successions of the eastern Focsani Basin. The second stack, processed to 20 s along the entire line crossing the Vrancea zone as well as Focsani Basin and called the "full-stack", shows the highly reflective sedimentary strata of the Focsani Basin, the geometry of the transition zone between the foreland basin and external nappes, as well as a number of intracrustal features.

In particular it reveals the presence of a thick rift-like sedimentary basin underlying this transition area, in the depth range 10 – 25 km. This sedimentary basin, which is of indeterminate age and could be as old as Early Palaeozoic or as young as Neogene, is approximately coincident with hypocenters that define the crustal depth segment of the earthquake prone Vrancea zone (as opposed to the seismically more intense upper mantle segment). The sedimentary

successions within this basin and other horizons visible further to the west, beneath the Carpathians nappes, suggest that the geometry of the Neogene and Recent uplift observed in the Vrancea zone, likely coupled with contemporaneous rapid subsidence in the western Focsani Basin, is detached from deeper levels of the crust at about 10 – 12 km depth. The Moho lies at a depth of about 40 km along the profile, its poor expression in the reflection stack being supported by independent estimates from coincident refraction data. Given the apparent thickness of the (meta)sedimentary supracrustal units, the crystalline crust beneath this area is quite thin (< 20 km). This may support the hypothesis of delamination of (lower) continental crust in this area involved in the evolution of the seismic Vrancea zone.

Chapter 6

Conclusions

This last chapter summarizes the main conclusions of this thesis. The purpose of this thesis was to analyze the effectiveness of the use of single sensors in seismic data acquisition performed in areas with rough topographies. In the last decades, it was common thought that arrays of sensors would enhance the signal-to-noise ratio of the recorded data even in hilly and mountainous areas but we demonstrated that arrays of sensors can work destructively in those cases. We have shown this via modeling and field studies, in acquisition, processing and interpretation.

In Chapter 2 we showed that array responses are strongly affected by the phase and amplitude variations; both types of variations exist due to the field conditions studied in this thesis. We performed tests with such variations where it was observed that the effect of phase variations is larger than that of amplitude variations. Phase variations were created using irregular spacing of single sensors and using intra-array static errors. The effectiveness of the use of single sensors was studied using two modeled datasets, one with single sensors and one with array responses. The processing results of these two datasets

showed the importance of phase variations on single-sensor and array responses. This effect can be easily removed from the single-sensor recordings while array responses are permanently affected. In the latter case, the wavelet of the reflected waves, which represent the signal in the seismic reflection surveys, is strongly distorted due to these variations. Many other processing steps are affected. For example, the filtering techniques will not be able to enhance the reflections. Or, problems may occur during velocity analysis where we need clear reflections, characterized by the highest amplitude possible, in order to get an accurate 2D velocity model used for stacking of data. Going further to the interpretation of the stacked time sections, the analysis of these reflections can lead to a miss-interpretation of the geological conditions from the studied area. Lateral variations in amplitude occur due to lateral variations of different physical parameters, due to lateral variations in the fluid content or facies, etc. In our example, the lateral variations in amplitude occurred due to significant intra-array static errors. Single-sensor data allow these issues to be tackled properly.

One possible way to improve the array responses in such areas is to use fine spatially sampled single sensors. In this way, we can remove the static errors prior to synthesizing the array response thus partially attenuating the noise contained by the single-sensor recordings via array-forming. This would mean that many more channels must be recorded and this has only become possible in the last few years. 10,000 channel-systems are now available on the market. But even for these cases local variations need to be treated separately and cannot be tackled by summing a group of single-sensors when rough topography is involved.

In Chapter 3, we propose a new method for the seismic industry to do array-forming of single-sensor data via digital group forming. Since we have now single-sensor recordings, the group forming can be done in a better way.

The method we propose is called the Minimum Variance Distortionless Response (MVDR) beamformer. The difference between the standard array-forming and the MVDR beamformer are essentially the weights applied to the single-sensor recordings before their summation. In the standard array-forming the weights are fixed and equal to 1 and in the MVDR case, the weights are based on the analysis of the raw single-sensor recordings, so data-adaptive. This type of beamformer uses the spatially global information to create a record that contains the presumed desired signal, required by the computation of the signal covariance matrix, and the spatially local information in order to obtain the MVDR beamformer response. In the first case we define a global filter and in the latter case a local filter. Its application on the 2D and 3D synthetic and field data showed a better attenuation of the undesired energy. For this study we designed the survey ourselves and were in the field to check on its implementation. In our studies, the undesired energy means the energy located at wavenumbers greater than the Nyquist wavenumber computed for the group interval. Also, this algorithm is completely data-dependent. Its application does not require any modeling or pre-processing of single-sensor recordings. The only pre-processing step applied is static corrections, in case of data recorded in areas with rough topographies. The standard array-forming and the MVDR beamforming were applied to the single-sensor dataset recorded in a hilly area in Romania. This dataset was recorded at the same time with a long shallow seismic line as a part of an international project (ISES-CARFOR) that we designed too. Being involved in the acquisition of these datasets, I was focused mainly on the planting of the geophones at regular spacing as much is possible. Since the intra-array static errors were not significant, I applied both algorithms on raw seismograms. Next, the static corrections were applied later, during the data processing flow. In the pre-stack data in both the (t, x) and the (f, k_x) domains, the MVDR beamforming response showed a better attenuation of the

out-of-new-spatial-band energy, i.e., mainly surface-waves energy, compared to that one provided by the standard array-forming. Next, stacking of traces enhanced the signal-to-noise ratio of the section based on the MVDR beamformer responses. The reflections seen on the central part of the final stacked time section are clearer and characterized by higher amplitude compared to those seen on the section based on the standard array-forming responses. Also, the continuity of the reflections seen on the upper part of the section based on the MVDR beamformer responses is higher. The quality of the MVDR beamformer responses depends on the quality of single-sensor recordings. If reflected waves are difficult to be seen on the initial recordings, then it is well likely that they are also difficult to be seen on the MVDR beamformer responses.

Single-sensor recordings create a larger amount of data to process but also certain processing steps to be taken which would otherwise not have been possible. In Chapter 4 we used a method called stereotomography which was becoming possible to use while if standard arrays would have been used in the field, this analysis could not have been employed. Stereotomography is a method with which a velocity model can be built, based on local coherency of reflectors. This method belongs to the group of slope methods and it can be applied on pre-stack or post-stack single-sensor seismic data. The travel-times are determined through the automatic picking of locally coherent events; it is not necessary to identify the entire event on the trace gather. The pre-stack stereotomography, which we have used in this thesis, uses stacked data for the automatic travel-time picking. The stacked data are presented by the Common-Reflection-Surface (CRS) stack, obtained after the stacking of traces from super common-midpoint gathers. The use of post-stack stereotomography was very efficient in the case of the partial-3D single-sensor shallow dataset recorded in a hilly area, where the maximum difference in elevation was 200 m. In general,

the signal-to-noise ratio of this dataset was low. Good reflections are seen only at the beginning and the end of the profile; the seismograms recorded on the center of the profile are characterized by very low signal-to-noise ratio. Therefore, the standard velocity analysis from the data processing software package could not provide a reliable 2D velocity model. The post-stack stereotomography method was very efficient in building of the 2D velocity model since the automatic travel-time picking was done on stacked data; we know that the signal-to-noise ratio of a record is enhanced by stacking. A 2D velocity model was obtained after the inversion of the picked travel-times. In addition, I verified the accuracy of the velocity model by a Common-Image-Gather (CIG) analysis, during the depth migration step. At the same time, I processed the single-sensor dataset using the Common-Midpoint (CMP) approach. If we compare the results of the CMP and CRS-stereotomography approaches, we notice that, in general, the signal-to-noise ratio is higher and the reflections are more continuous on the section based on the CRS-stereotomography approach. Also, because the 2D velocity model is more accurate after the CRS-stereotomography approach we can say that we have a better depth positioning of the reflectors / geological interfaces. Using a 2D dataset obtained by stacking in the cross-line direction, I obtained a more accurate 2D velocity model. The number of the picked travel-times on the CRS stack is greater. In addition, the accuracy of this new velocity model is sustained by the image of the CIGs. The depth migrated section shows an improved image of the structure for the analyzed depth interval.

Then in Chapter 5 we used an approach where single-sensors were used as part of a reflection survey with the purpose to investigate the deep structure of the crust. We designed and recorded this dataset along a long profile (~ 130 km) that crosses the mountainous area of the curvature zone of Carpathians, the hilly area and ended in the plain area (Focsani Basin). The access to the single-

sensor points was difficult, especially in the mountainous area. The receivers could not be planted in the designed position, especially in the mountainous area, and their effect was seen on the seismic records. The static errors due to elevation along the seismic profile were very significant. As can be concluded from the modeling results, the use of arrays of sensors in the mountainous area can have a destructive effect on reflections and, further, on the results of data processing steps and interpretation. Therefore, we decided to use single sensors for data acquisition. Next, static errors were removed during the processing. The first arrivals times could easily be picked on the records from the plain area. The quality of these records was very good, with clear reflections and first arrivals. The western part of the profile showed a low signal-to-noise ratio of the recorded seismograms where noise covers the first arrivals. The surface wave cone covers the reflected waves. Still, it was possible to retrieve the reflection information where the (f, x)-deconvolution step turned out to be crucial. After the static corrections were applied, the processing was split into two directions, namely for the upper and lower crust reflectivity. In the first case, we obtained the so-called *partial stack* and for the latter the *full stack*. The main difference between the processing flows was the time length and the number of the analyzed recordings. The filtering techniques, where the (f, x)-deconvolution step was the most significant, could enhance the signal-to-noise ratio of the single-sensor records. The velocity analysis on the CMP-gathers provided the 2D velocity model possible. The new structural information obtained after the tectonic interpretation of these two sections has been used to update the existing tectonic models for the curvature area of Carpathians and the Focsani Basin. Looking at the full stack, there is good evidence to suggest that a thick (~ 10 km) sedimentary basin having the structure of a graben and of indeterminate age underlies the westernmost part of the Focsani Basin, in the depth range 10-25 km; this feature has not been observed before. Furthermore,

most of the crustal depth seismicity observed in the Vrancea zone appears to be associated with this sedimentary basin. Also, the sedimentary successions within this basin and other horizons visible further to the west, beneath the Carpathian nappes, suggest that the geometry of the Neogene and the recent uplift observed in the Vrancea zone, likely coupled with contemporaneous rapid subsidence in the foreland, is detached from deeper levels of the crust at about 10 km depth. Given the apparent thickness of the meta-sedimentary supra-crustal units, the crystalline crust beneath this area is thin, less than 20 km at a velocity of 6.5 km/s or more based on the refraction measurements, supporting the hypothesis that there may have been delamination of (lower) continental crust in this area involved in the evolution of the seismic Vrancea zone.

Finally, in this thesis we have shown at different levels that it is advantageous to use single-sensor recordings in areas with rough topographies. Also, fine spatially sampled single-sensor recordings can be used to synthesize array or MVDR beamformer responses, if needed, but only after static corrections are applied. In this way, we attenuate the surface waves and we protect the reflected waves. We have shown that the MVDR beamformer performs a better noise attenuation compared with standard-arrays, therefore it should be applied in such field situations. The output records will be characterized by higher signal-to-noise ratio compared to than one of the initial records. More important, the amount of aliased energy is reduced and this enhances the effectiveness of the use of some processing algorithms (e.g. filtering, migration).

Indeed, using single-sensor recordings, much more data need to be handled but, presently, there is the capacity for storage and data processing in industry. In oil exploration, the obtaining of high quality seismic data must prevail. Also, if the single-sensor recordings are kept throughout the whole processing sequence, it is prohibitively expensive for a normal 3D exploration

survey, especially when pre-stack depth migrations are needed. In those cases, it is advantageous to use local digital-array as we have proposed in this thesis in Chapter 3. Therefore, we claim that the seismic industry should move towards a standard use of single sensors when recording seismic data. In a decade or so, the amount of data and data transport will not be the bottle-neck any more. With single-sensor recordings more imaging problems can be solved than possible today.

Appendix A.1

Temporal and Spatial Fourier Transforms

In this thesis we make use of an important mathematical function called the Fourier transform. In this appendix we give the proper definitions of these transforms, in time and space. As a definition, the Fourier transform is the transformation of a function into weights of sines and cosines, via the complex exponentials; the sines and cosines are the basis functions into which the function is decomposed.

A.1.1 The one-dimensional Fourier Transform in time and space

The one-dimensional Fourier transform can be used to convert a time-signal (one trace) from the time to the frequency domain. Let us note with *g(t)* a function in the time domain, in which *t* denotes time. It can be transform into the frequency domain using the forward temporal Fourier transform:

$$G(f) = \int_{-\infty}^{+\infty} g(t) e^{(-i2\pi ft)} \mathrm{d}t, \qquad \text{(A.1.1)}$$

where i is the imaginary unit, $i = \sqrt{-1}$ and f is the transform variable frequency.

The inverse temporal Fourier transform is used for the reconstruction from the time signal out of its frequency components:

$$g(t) = \int_{-\infty}^{+\infty} G(f) e^{(i2\pi ft)} \mathrm{d}f. \tag{A.1.2}$$

Since the seismic recordings are obtained from different spatial positions, we use the spatial Fourier transform for their analysis. If we note with *h(x)* a function sampled in one spatial coordinate, say *x*, its converted function is:

$$H(k_x) = \int_{-\infty}^{+\infty} h(x) e^{(i2\pi k_x x)} \mathrm{d}x, \tag{A.1.3}$$

where k_x is the spatial frequency with respect to space *x*, also called the wavenumber.

The original signal, *h(x)*, can be obtained by integrating over all k_x components using the inverse spatial Fourier transform:

$$h(x) = \int_{-\infty}^{+\infty} H(k_x) e^{(-i2\pi k_x x)} \mathrm{d}k_x. \tag{A.1.4}$$

A.1.2 The two-dimensional Fourier Transform

The two-dimensional Fourier transform is used to convert one seismic data (e.g. common-source gather, common-receiver gather) from the time domain, *(t, x)*, to the frequency domain, *(f, k_x)*, in case of one spatial coordinate, say *x*.

Let us note with *s(t, x)* a signal that varies in time and space. The two-dimensional Fourier transform of this signal is defined as:

$$\tilde{S}(k_x, f) = \int_{-\infty}^{+\infty}\int_{-\infty}^{+\infty} s(x,t)e^{[-i2\pi(k_x x - ft)]}\mathrm{d}t\mathrm{d}x. \qquad \text{(A.1.5)}$$

The original signal can be recovered using the inverse Fourier transform:

$$s(x,t) = \int_{-\infty}^{+\infty}\int_{-\infty}^{+\infty} \tilde{S}(k_x, f)e^{[i2\pi(k_x x - ft)]}\mathrm{d}f\mathrm{d}k_x. \qquad \text{(A.1.6)}$$

Appendix A.2

Method of Lagrange multipliers

In this appendix the method of Lagrange multipliers is explained. Here, we follow Arfken (1985). The method of Lagrange multipliers is a method used to find the *extremum* of a multivariate function $f(x_1, x_2, .., x_n)$ subject to the *constraint* $c(x_1, x_2, ..., x_n) = 0$, where f and c are functions with continuous first partial derivatives on the open set containing the curve $c(x_1, x_2, ..., x_n) = 0$, and $\nabla c \neq 0$ at any point on the curve. An *extremum* of a function is a maximum or a minimum of that function. A *constraint* is a condition that a solution to an optimization problem must satisfy in order to be acceptable. Two types of constraints can be used, namely equality and inequality constraints, depending on their definition (e.g. certain values, for equality constraints, and intervals, for inequality constraints).

For an *extremum* of f to exist on c, the gradient of f must line up with the gradient of c. The gradient is a horizontal vector (i.e. it has no vertical (z) component) that shows the direction that the function increases. If the two gradients are in the same direction, then one is a multiple (- λ) of the other, so:

$$\nabla f = -\lambda \nabla c. \qquad \text{(A.2.1)}$$

The two vectors are equal, so all of their components are as well, giving:

$$\frac{\partial f}{\partial x_k} + \lambda \frac{\partial c}{\partial x_k} = 0, \qquad \text{(A.2.2)}$$

for all $k = 1, 2, \ldots, n$, where the constant λ is called the Lagrange multiplier. The extremum is then found by solving the $n+1$ equation in $n+1$ unknown, which is dome without inverting c, which is why Lagrange multipliers can be so useful.

For multiple constraints, $c_1 = 0$, $c_2 = 0$, …

$$\nabla f + \lambda_1 \nabla c_1 + \lambda_2 \nabla c_2 + \ldots = 0. \qquad \text{(A.2.3)}$$

Appedix A.3

Mathematical description of Singular Value Decomposition

In this appendix we summarize the method of Singular-Value Decomposition (SVD). In linear algebra, the singular value decomposition (SVD) is an important factorization of a rectangular real or complex matrix, with several applications in signal processing and statistics.

Let us suppose a $m \times n$ matrix $\mathbf{M}$ whose entries come from the field K, which is either the field of real numbers or the field of the complex numbers. Then there exists a factorization of the form:

$$\mathbf{M} = \mathbf{U}\boldsymbol{\Sigma}\mathbf{V}^{*}, \qquad \text{(A.3.1)}$$

where $\mathbf{U}$ is a $m \times m$ *unitary matrix* over K, the matrix $\boldsymbol{\Sigma}$ is $m \times n$ with non-negative numbers on the diagonal and zeros off the diagonal, and $\mathbf{V}^{*}$ denotes the *conjugate transpose* of $\mathbf{V}$, an $n \times n$ unitary matrix over K.

Such a factorization is called a singular-value decomposition of **M**. The matrix **V** contains a set of orthonormal "input" or "analyzing" basis vector directions for **M**. The matrix **U** contains a set of orthonormal "output" basis vector directions for **M**. The matrix **Σ** contains *singular values*, which can be thought as scalar "gain controls" by which each corresponding input is multiplied to give a corresponding output.

The *singular values* are non-negative real numbers often listed in decreasing order s_1, s_2, .., also defined as eigenvalues, and are located on the diagonal of **Σ**. The term "eigenvalue" was introduced by *Schmidt* (1907), and the term "singular values" by *Smithies* (1937).

A *unitary matrix* is a $n \times n$ complex matrix **A** that satisfies the condition:

$$\mathbf{A}^*\mathbf{A} = \mathbf{A}\mathbf{A}^* = \mathbf{I}_n, \qquad \text{(A.3.2)}$$

where $\boldsymbol{I_n}$ is the identity matrix and $\mathbf{A}^*$ is the conjugate transpose (also called Hermitian) of **A**. The matrix **A** is unitary if and only if it has an inverse which is equal to its conjugate transpose $\mathbf{A}^*$.

The *conjugate transpose* (or Hermitian transpose) of an $n \times n$ matrix **A** with complex entries is the $n \times m$ matrix $\mathbf{A}^*$ obtained by taking the transpose and then taking the complex conjugate of each entry. The conjugate transpose is formally defined by:

$$(\mathbf{A}^*)_{i,j} = \overline{\mathbf{A}}_{j,i}, \qquad \text{(A.3.3)}$$

where the subscripts denote the i, j-th entry, for $1 \leq i \leq n$ and $1 \leq j \leq m$, and the overbar denotes a scalar complex conjugate. The definition can also be written as:

$$\mathbf{A}^{*} = \bar{\mathbf{A}}^{T}, \qquad \text{(A.3.4)}$$

where $\mathbf{A}^{\mathbf{T}}$ denotes the transpose and $\bar{\mathbf{A}}$ denotes the matrix with complex conjugated entries.

Bibliography

Arfken, G. (1985), "Lagrange Multipliers" in Mathematical Methods for Phisicists, 3rd ed. Orlando, FL: Academic Press, 945 – 950.

Bell, K.L., Y.Ephraim, and H.L. van Trees (2000), A Bayesian approach to robust adaptive beamforming, *IEEE Trans. Signal Processing, 48*, 386 – 398.

Bertotti, G., L. Matenco, and S. Cloetingh (2003), Vertical movements in and around the SE Carpathian foredeep: lithospheric memory and stress field control. *Terra Nova, 15, 299305.*

Billette, F., and G. Lambaré (1998), Velocity macro-model estimation from seismic reflection data by stereotomography, *Geophy. J. Int., 135(2)*, 671 – 680.

Billette, F., Le Bégat, P. Podvin, and G. Lambaré (2003), Practical aspects and applications of 2D Stereotomography, *Geophysics, 68(3)*, 1008 – 1021.

Bocin, A., N. Cazan, M. Haldan, I. Panea, R. Stephenson, F. Hauser, I. Dumitru, P. Georgescu, V. Mocanu, L. Matenco, G. Drijkoningen, and C. Dinu (2003), 2D seismic velocity modeling in Vrancea zone and Focsani Basin. *In*: Geodynamic and tectonic evolution of the Carpathian arc and its foreland: Environmental tectonics and continental topography, pp 71. Stephan Mueller Conference, Retezat Mts – Southern Carpathians, Romania, Projectcode C25E30.

Bocin, A., R. Stephenson, A. Tryggvason, I. Panea, V. Mocanu, F. Hauser, and L. Matenco (2005), 2.5D seismic velocity modelling in the south-eastern Romanian Carpathians Orogen and its foreland, *Tectonophysics, 410, Issues 1-4*, 273 – 291.

Capman, X.H., G.C. Herman, and E. Muyzert (2006), Suppressing near-receiver scattered waves from seismic land data, *Geophysics, 71*, 121 – 131.

Capon, J. (1969), High resolution frequency-wavenumber spectrum analysis, *Proc. IEEE, 57,* 1408 -1418.

Chalard, P. Podvin, Le Bégat, and D. Berthet (2002), 3D stereotomographic inversion on a real dataset, *SEG 72nd Ann. Meeting, Expanded Abstracts*, 946 – 948.

Chalot-Prat, F., and R. Girbacea (2000), Partial delamination of continental mantle lithosphere, uplift-related crust-mantle decoupling, volcanism and basin formation: a new model for the Pliocene-Quaternary evolution of the southern East- Carpathians, Romania, *Tectonophysics, 327*, 83-107.

Chauris, H., M. Noble, G. Lambaré, and P. Podvin (2002), Migration velocity analysis from locally coherent events in 2-D laterally heterogeneous media, part I: Theoretichal aspects, *Geophysics, 67(4)*, 1202 – 1212.

Cloetingh, S., E. Burov, L. Matenco, G. Toussaint, G. Bertotti, P.A.M. Andriessen, M.J.R. Wortel, and W. Spakman (2004), Thermo-mechanical controls on the mode of continental collision in the SE Carpathians (Romania), *Earth Planet. Sci. Lett, 218*, 57-76.

Cook, F.A., K.C. Koflin, L.S. Lane, J.R. Dietrich, and J. Dixon (1987). Structure of the southeast margin of the Beaufort-Mackenzie Basin, Arctic Canada, from crustal seismic reflection data, *Geology, 15*, 931-935.

Cooper, N. (2004), A world of reality – Designing land 3D programs for signal, noise and prestack migration – Part 2, *The Leading Edge, 23*, 1230 – 1235.

Cornea, I., F. Rădulescu, A. Pompilian, and A. Sova (1981), Deep seismic sounding in Romania, *Appl. Geophys., 119*, 1144-1156.

Cox, H. (1973), Resolving power and sensitivity to mismatch of optimum array processors, *J. Acoust. Soc. Amer., 54*, 771 – 758.

Cox, H., R.M. Zeskind, and M.H. Owen, 1987, Robust adaptive beamforming, *IEEE Trans. On Acoustics, Speech and Signal Processing,* **35**, 1365 – 1376.

Csontos, L., A. Nagymarosy, F. Horváth, and M. Kovác (1992), Tertiary tectonic evolution of the Intra Carpathian area a model, *Tectonophysics, 208, 1/3* (Amsterdam), 221-241.

Csontos, L. (1995), Tertiary tectonic evolution of the Intra-Carpathian area: a review, *Acta Vulcanologica 7*, 1-13.

Demetrescu, C. (1982), Thermal structure of the crust and upper mantle of Romania, *Tectonophysics, 90*, 123-135.

Dicea, O. (1995), The structure and hydrocarbon geology of the Romanian East Carpathians border from seismic data, *Petroleum Geoscience, 1*, 135-143.

Dinu, C., H.K. Wong, D. Tambrea, and L. Matenco (2005), Stratigraphic and structural characteristics of the Romanian Black Sea shelf, *Tectonophysics, 410, Issues 1-4,* 417 – 435.

Drijkoningen, G.G. (2000), The usefulness of geophone ground-coupling experiments to seismic data, *Geophysics, 65(6)*, 1780 – 1787.

Drijkoningen, G.G., F. Rademakers, E.C. Slob, and J. Fokkema (2006), A new elastic model for ground coupling of geophones with spikes, *Geophysics, 71(2)*, Q9-17.

Enescu, D., I. Cornea, P. Constantinescu, F. Rădulescu, and S. Pătrut (1972), Structure of the crust and upper mantle within the Carpathian bending zone, *St. Cerc. Geol. Geof., Seria Geofizică, 10 (1)*, 23-41 (in Romanian).

Enescu, D., A. Pompilian, and A. Bălă (1988), Distributions of the seismic wave velocities in the lithosphere of some regions in Romania, *Rev. Roum. Géol. Géophys. Géogr. Sér. Géophys., 32*, 3-11.

Enescu, D., D. Danchiv, and A. Bălă (1992), Lithosphere structure in Romania II. Thickness of Earth's crust. Depth-dependent propagation

velocity curves for the P and S waves, *Stud. Cercet. Geol. Geofiz. Geogr. Ser. Geofiz., 30*, 3-19.

Enescu, D., C. Diaconescu, and M. Diaconescu (1993), Lithosphere structure in Romania. III. Results on the deep structure of Vrancea zone, *Rev. Roum. Geophysique, 37*, 51-60.

Feldman, D.D., and L.J. Griffiths (1994), A projection approach to robust adaptive beamforming, *IEEE Trans. Signal Processing, 42*, 867 – 876.

Fuchs, K., K. Bonjer, G. Back, I. Cornea, C. Radu, D. Enescu, D. Jianu, A. Nourescu, G. Merkler, T. Moldoveanu, G. Tudorache (1979), The Romanian earthquake of March 4, 1977: II Aftershock and migration of seismic activity, *Tectonophysics 53 (3-4)*, 225 – 247.

Gershman, A.B. (1999), Robust adaptive beamforming in sensor arrays, *Int. J. Electron. Commun. 53, 305-314.*

Ghica, D., M. Radulian, and M. Popa (2005), Noise level analysis for BURAR seismic array, Romania, *EGU Mtg., Geophysical Research Abstracts, 7*, 04100.

Girbacea, R. and W. Frisch. (1998), Slab in the wrong place: lower lithospheric mantle delamination in the last stage of the Eastern Carpathian subduction retreat, *Geology 26 (7)*, 611-614.

Godara, L.C. (1986), Error analysis of the optimal antenna array processors, *IEEE Trans. Aerosp. Electron. Syst., AES-22*, 395 – 409.

Godara, L.C. (1997), Application of antenna arrays to mobile communications. II. Beam-forming and direction-of-arrival considerations, *Proc. IEEE, 85*, 1195 – 1245.

Harmanci, K., J. Tabrikian, and J.L. Crolik (2000), Relationships Between Adaptive Minimum Variance Beamformers and Optimal Source Localization, IEEE Transactions on Signal Processing, *48*, 1-10.

Hauser, F., V. Răileanu, W. Fielitz, A. Bălă, C. Prodehl, G. Polonic, and A. Schulze (2001), VRANCEA99-the crustal structure beneath the southeastern Carpathians and the Moesian Platform from a seismic refraction profile in Romania, *Tectonophysics 340*, 233-256.

Hauser, F., C. Prodehl, M. Landers, and Vrancea Working Group (2002), Seismic experiments target earthquake-prone region in Romania, *EOS 83*, 457, 462-463.

Hauser, F., V. Raileanu, M. Landes, A. Bala, C. Prodehl, and W. Fielitz (2003), Properties of the eastern Carpathian Lithosphere, derived from two seismic refraction surveys in Romania - Part 1, *Geophysical Research Abstracts, 5*, *EAE03-A-03359*.

Hauser, F., Raileanu, V., Fielitz, W., Dinu, C., Landes, M., Bala, A., and Prodehl, C. (2007), Seismic crustal structure between the Transylvanian Basin and the Black Sea, Romania, *Tectonophysics*, *430*, 1-25.

Hoffe, B.H., G.F. Margrave, R.R. Stewart, D.S. Foltinek, H.C. Bland, and P. Manning (2002), Analyzing the effectiveness of receiver arrays for multicomponent seismic exploration, *Geophysics, 67(6)*, 1853 – 1868.

Holle, J.A. (1992), Nonlinear high-resolution three-dimensional seismic travel time tomography, *Journal of Geophysical Research 97*, 6553 – 6562.

Hoover, G.M., and J.T. O'Brien (1980), The influence of the planted geophone on seismic land data, *Geophysics, 45*, 1239 – 1253.

Hubral, P. (1999), Macro model independent seismic reflection imaging, *J. Appl. Geoph. 42 (3,4)*-Special issue on Karlsruhe Workshop on macro model independent seismic reflection imaging.

Jaeger, R., J. Mann, G. Hoecht, and P. Hubral (2001), Common-reflection-surface stack: Image and attributes, *Geophysics, 66 (1)*, 97 – 109.

Jian, L., P. Stoica, and Z. Wang (2003), On robust Capon beamforming and diagonal loading, IEEE Trans. on Signal Processing, **51**, Issue 7, 1702-1715.

Johnson, D.H., and D.E. Dudgeon (1993), Array signal processing: concepts and techniques, *Englewood Cliffs, NJ: PTR Prentice Hall*.

Kiratzi, A.A. (1993), Active Deformation in the Vrancea Region, Rumania, *PAGEOPH, 140(3)*, 392-402.

Knapp, J.H., C.C. Knapp, V. Raileanu, L. Matenco, V. Mocanu, and C. Dinu (2005), Crustal constraints on the origin of mantle seismicity in the Vrancea Zone, Romania: the case for active continental lithospheric delamination, *Tectonophysics, 410, Issues 1-4*.

Krohn, C.E. (1984), Geophone ground coupling, *Geophysics, 49*, 722 – 731.

Lambaré, G., M. Alerini, R. Baina, and P. Podvin (2003), Stereotmography: a fast approach for velocity macro-model estimation, *SEG 73rd Ann. Meeting, Expanded Abstracts*, 850 – 853.

Lambaré, G., M. Alerini, and P. Podvin (2004), Stereotomographic picking in practice, *EAGE 66th Conference and Exhibition, France*.

Lavaud, B., R. Baina, and E. Landa (2004), Poststack stereotomography: A robust strategy for velocity model estimation, *EAGE 66th Conference and Exhibition, France*.

Leever, K., G. Bertotti, and S. Cloetingh (2003), Neotectonics in the Focsani basin, Eastern Carpathians, *European Geophysical Society General Assembly. Geophysical Research Abstracts, Nice, France*, 03578.

Linzer, H.G. (1996), Kinematics of retreating subduction along the Carpathian arc, Romania, *Geology*, 167-170.

Mann, J., R. Jaeger, T. Müller, G. Hoecht, and P. Hubral (1999), Common-relfection-surface stack – a real data example, *J. Appl. Geoph. 42 –* Special issue on Karlsruhe workshop on macro model independent seismic reflection imaging, 301 – 318.

Matenco, L. and G. Bertotti (2000), Tertiary tectonic evolution of the external East Carpathians (Romania), *Tectonophysics, 316*, 255-286.

Matenco, L., G. Bertotti, S. Cloetingh, and C. Dinu (2003), Subsidence analysis and tectonic evolution of the external Carpathian-Moesian platform region during Tertiary times, *Sedimentary Geology, 156*, 71-94.

Matenco, L., R. Zoetemeijer, S. Cloetingh, and C. Dinu (1997), Lateral variations in mechanical properties of the Romanian external

Carpathians: inferences of flexure and gravity modeling, *Tectonophysics, 282*, 147-166.

Monzingo, R.A., and T.W. Miller (1980), Introduction to Adaptive Arrays: New York, Wiley.

Morse, P.F., and G.F. Hildebrandt (1989), Ground-roll suppression by the stack array, *Geophysics, 54*, 290 – 301.

Müller, T. (1999), The common reflection surface stack method – Seismic imaging without explicit knowledge of the velocity model, Ph. D. thesis, Universität Karlsruhe.

Muyzert, E., and G.J.O. Vermeer (2004), The impact of acquisition perturbations on land seismic data, *SEG 74th Ann. Meeting, Expanded Abstracts*, 79 – 81.

Neducza, B. (2007), Stacking of surface waves, Geophysics, **72**, V51-V58.

Nemcock, M., L. Pospisil, J. Lexa, and R.A. Donelick (1998), Tertiary subduction and slab break-off model of the Carpathian-Pannonian region, *Tectonophysics, 295*, 307-340.

Newman, P., and J.T. Mahoney (1973), Patterns with a pinch of salt, *Geophys. Prosp., 21*, 197 – 219.

Oncescu, M.C. and K.P. Bonjer (1997), A note on the depth recurrence and strain release of large Vrancea earthquakes, *Tectonophysics, 272*, 291-302.

Ozbek, A. (2000), Adaptive Beamforming with Generalized Linear Constraints, *70th Ann. SEG Mtg., Expanded Abstracts*.

Panea, I., G.G. Drijkoningen, G. Bertotti, G., and L. Matenco (2003), Effect of perturbations on array forming, *73rd Ann. SEG Mtg., Expanded Abstracts*.

Panea, I., G.G. Drijkoningen, G. Bertotti, and L. Matenco (2004), Analyzing the effect of intra-array variations using single-sensor seismic data, *66th EAGE Conference, Expanded Abstracts*.

Panea, I., R. Stephenson, C. Knapp, V. Mocanu, G. Drijkoningen, L. Matenco, J. Knapp, and K. Prodehl (2005), Near-vertical seismic reflection image using a novel acquisition technique across the Vrancea Zone and Focsani Basin, south-eastern Carpathians (Romania), *Tectonophysics, 410, Issues 1-4*, 293 – 309.

Pharaoh, T.C. (1999), Palaeozoic terranes and their lithospheric boundaries within the Trans-European Suture Zone (TESZ): a review, *Tectonophysics, 314*, 17-41.

Rabagia, T. and M. Tarapoanca (1999), Tectonic evolution of the Romanian part of the Moesian platform: an integrated model, *Romanian Journal of Tectonics and Regional Geology, 77*, 58.

Raghunath, K.J., and V.U. Reddy (1992), Finite Data Performance Analysis of MVDR Beamformer with and without Spatial Smoothing, IEEE Transactions on Signal Processing, *40*, 2726-2735.

Rapapport, T.S., Ed. (1998), Smart antennas: Adaptive arrays, algorithms, and wireless position location, *IEEE*.

Rădulescu, D.P., I. Cornea, M. Sandulescu, P. Constantinescu, F. Radulescu, and A. Pompilian (1976), Structure de la crôute terrestre en Roumanie. Essai d'interprétation des études séismiques profondes, *An.Inst. Geol. Geofiz., 50*, 5-36.

Rădulescu, F. and V. Răileanu (1981), Reflection records with prolonged times. In: Studies on the crustal and upper mantle structure in the S and W of Romania, *Intern. Rep. CSEN/CFP, 31.81.3, CFP Archive*, Bucharest, 35 pp.

Rădulescu, F. V. Răileanu, and I. Cornea (1984), Contributions of the reflection seismic method to the crustal structure deciphering, *Stud. Cerc. Geol. Geofiz. Geogr. Ser. Geofiz., 22*, 11-17 (in Romanian).

Rădulescu, F. (1988), Seismic models of the crustal structure in Romania, *Rev. Roum. Géol. Géophys. Géogr. Sér. Géophys., 32*, 13-17 (in Romanian).

Răileanu, V., C. Diaconescu, and F. Rădulescu (1994), Characteristics of

Romanian lithosphere from deep seismic reflection profiling, *Tectonophysics, 239*, 165-185.

Răileanu, V., and C.C. Diaconescu (1998), Some seismic signatures in the Romanian crust, *Tectonophysics, 288*, 127-136.

Reed, I.S., J.D. Mallett, and L.E. Brennan (1974), Rapid convergence rate in adaptive arrays, IEEE Trans. Aerosp. Electron. Syst., *AES-10*, 853-863.

Roure, F., G. Bessereau, M. Kotarba, J. Kusmierek, and W. Strzetelski (1993), Structure and hydrocarbon habitas of the Polish Carpathian Province, *AAPG Bulletin 77*, 1660.

Royden, L.H. (1988), Late Cenozoic tectonics of the Pannonian basin system, *in* Royden L.H. and Horvath F., eds., The Pannonian basin. A study in basin evolution: American Association of Petroleum Geologists Memoir, 27-48.

Royden, L.H. (1993), The tectonic expression of the slab pull at continental convergent boundaries, *Tectonophysics*, 303-325.

Sanders, C., P. Andriesseu, and S. Cloetingh (1999), Life cycle of the East Carpathian Orogen: erosion history of a doubly vergent critical wedge assessed by fission track thermochronology, *J. Geophys. Res. 104*, 095-29,112.

Săndulescu, M. (1984), Geotectonica României (translated title: Geotectonics of Romania). Ed. Tehnica, Bucharest, 450 pp.

Săndulescu, M. (1988), Cenozoic Tectonic History of the Carpathians. In: L.H. Royden and F. Horvath (Editors), The Pannonian Basin, a study in basin evolution. *AAPG Memoir*, 17-25.

Săndulescu, M.and M. Visarion (1988), La structure des plate-formes situées dans l'avant-pays et au-dessous des nappes du flysch des Carpates Orientales, *St. tehn. econ., Geofiz. 15*, 62-67.

Shahbazpanahi, S., A.B. Gershman, Z-Q Luo, and K.M. Wong (2003), Robust adaptive beamforming for general-rank signal models, *IEEE Trans. Signal Processing, 51(9)*, 2257 - 2269.

Sperner B., D. Ioane, and R.J. Lillie (2004), Slab behaviour and its surface expression: new insights from gravity modelling in the SE-Carpathians, *Tectonophysics, 382*, 51-84.

Stănica, D., M. Stănica, and M. Visarion (1986), The structure of the crust and upper mantle in Romania as deduced from magnetotelluric data, *Rev. Roum. Géol. Géophys. Géogr. Sér. Géophys., 30*, 25-35.

Stefanescu, M., O. Dicea, and G. Tari (2000), Influence of extension and compression on salt diapirism in its type area, East Carpathians Bend area, Romania. In: B.C. Vendeville, Y. Mart and J.L. Vigneresse (Editors), Salt, shale, and igneous diapirs in and around Europe, *Geological Society of London, Special Publication, 174*. 131-147.

Stephenson, R.A., K.C. Coflin, L.S. Lane, and J.R. Dietrich (1994), Crustal structure and tectonics of the southeastern Beaufort Sea continental margin, *Tectonics, 13*, 389-400.

Stone, D.G. (1994), Designing surveys in two and three dimensions. SEG.

Tărăpoancă, M., G. Bertotti, L. Matenco, C. Dinu, and S. Cloetingh (2003), Architecture of the Focsani depression: A 13 km deep basin in the Carpathians bend zone (Romania), *Tectonics, 22/6, 1074*, doi:10.1029/2002TC001486.

Tărăpoancă, M. (2004), Architecture, 3D geometry and tectonic evolution of the Carpathians foreland basin, PhD Thesis, Vrije Universiteit, Faculty of Earth and Life Sciences, Amsterdam, 120 pp.

Trappe, H., G. Gierse, and J. Pruessmann (2001), Application of the common-reflection-surface stack in time and depth processing, *SEG 71th Ann. Internat. Meeting, San Antonio, Expanded Abstracts*, W5-9.

Van Veen, B.D., and K.M. Buckley (1988), Beamforming: A versatile approach to spatial filtering, IEEE ASSP Magazine, 4-24.

Van Veen, B.D. (1991), Minimum Variance beamforming with soft response constraints, IEEE Trans. Signal Processing, **39**, 1964-1972.

Vermeer, G.J.O. (1990), Seismic wavefield sampling, SEG.

Visarion, M., M. Sandulescu, D. Stanica, and L. Atanasiu (1988). An improved geotectonic model of the East Carpathians, *Rev. Roum. Geol. Geophys et Geogr., Serie Geophysique, 32*, 43-52.

Vorobyov, S.A., A.B. Gershman, and Z.-Q. Luo (2003), Robust adaptive beamforming using worst-case performance optimization, IEEE Trans. Signal Processing, **51**, 313-324.

Wax, M., and Y. Anu (1996), Performance analysis of the minimum variance beamformer in the presence of steering vector errors, *IEEE, Trans. Signal Processing, 44*, 938 – 947.

Wenzel, F., U. Achauer, D. Enescu, E. Kissling, R. Russo, and V. Mocanu (1998), The final stage of plate detachment: International tomographic experiment in Romania aims to a high-resolution snapshot of this process, *EOS*.

Wenzel, F., B. Sperner, F. Lorenz, and V. Mocanu (2002), Geodynamics, tomographic images and seismicity of the Vrancea region (SE – Carpathians, Romania), *Stephan Mueller Spec. Public. Series 3*, 95 – 104.

Zoltowski, M.D. (1988), On the performance of the MVDR beamformer in the presence of correlated interference, IEEE Trans. Acoust., Speech, Signal Processing, *36*, 945-947.

ACKNOWLEDGEMENTS

I would like to express my gratitude to all persons who helped me to complete this thesis. First, I want to thank my promoter, Prof. dr. ir. Jacob Fokkema, for making this research possible and for his support, especially during the last year. Also, I want to sincerely thank my supervisor, Dr. Guy Drijkoningen, for his daily help and for his huge patience towards me in all these years. I also want to thank Dr. Randell Stephenson for making the first step in designing this research by including me in the international seismic project DACIA-PLAN. Special thanks are also due to Prof. Kees Wapenaar, Dr. Evert Slob, Prof. Dr. Kroonenberg, prof. Mulder and Guus Lohlefink for being so nice with me during my visits at the Delft University of Technology.

I owe Chapter 4 to Mr. Evgeny Landa, Mr. Gilles Lambaré and the OPERA team. I would like to thank them for helping me to understand how the stereotomography works.

I would like to thank my professors from the University of Bucharest, Department of Geology and Geophysics, for making my life easier at work: Prof. Corneliu Dinu, Prof. Paul Georgescu, Prof. Ivan Marian, Prof. Dumitru Ioane, Dr. Victor Mocanu, Dr. Liviu Matenco and Dr. Tudorel Orban. I can not forget Dr. Ion Dumitru (Mitica) who helped me with the installation of the data processing software Focus-Paradigm; I guess he became an expert in installing this software because he had to do it after every visit of mine to the Delft University of Technology.

Also, I can not forget my colleagues from Delft (Aletta, Dennis, Deyan, Petar, Martijn, Gerrit, Jesper, Elmer, Chris, Dirk, Ben, Daria, Ali and Daniela) and Bucharest (Mihai, Marius, Vlad, Diana, Andrei, Nicu, Marcela), and I am sorry because I can not remember all.

I am indebted to Dennis van der Burgh for his help with the Dutch translations and to my guiding Angel(ov) who took care about the final preparations regarding the defense of my thesis in the last months of my PhD thesis.

I had the chance to visit beautiful cities from Netherlands together with Dennis and taste different dishes together with Deyan and other colleagues from Delft.

Finally, I am very grateful to my family, especially to my husband and my son for their understanding regarding my long times spent apart of them.

Special thanks are due to my twin sister, Mari, who helped me in many ways during the last years.

ABOUT THE AUTHOR

Ionelia Panea (Lili) was born on the 11th of May 1972 in the famous town Caracal located in the Olt county from southern Romania. After graduating the Chemistry High-school in her native town, she and her twin sister applied to the Faculty of Geology and Geophysics, University of Bucharest. They both graduated with a B.Sc. degree in Geophysics in June 1996, followed by a M.Sc. degree in Petroleum Geology in July 1997.

She started working in 1996 as Research Assistant at the Institute of Geodynamics "Sabba S. Stefanescu" from Bucharest, where she studied the earth tides and earthquakes. At the end of 1997, she transferred to CCPEG-PETROM, a Romanian oil company based in Bucharest, where she worked as a Geophysicist. Later, she decided to pursue an academic career after her son, Catalin-Florin, was born so she accepted the teaching assistant position at the Faculty of Geology and Geophysics, department of Geophysics from University of Bucharest. She enjoys working with students from both departments since then.

In 2002 Lili applied for PhD at the Delft University of Technology, Department of Applied Earth Sciences or, as it is recently known, Geotechnology. During her PhD, she was involved in two main international seismic projects, and other many small projects, which gave her the opportunity of working and meeting experts in the field and make new friends. She presented the results of her projects to the SEG and EAGE Conferences, when

the great similarity between the twin sisters always created confusions among their professors and colleagues.